NEAR FIELD ACOUSTIC AND VIBRATION STUDIES WITH A CANTILEVER BEAM

KEN KLEIN

NEAR FIELD ACOUSTIC AND VIBRATION STUDIES WITH A CANTILEVER BEAM

by

Ken Klein

A thesis submitted to the

School of Graduate Studies

in partial fulfillment of the

requirements for the degree of

Master of Science

Department of Physics
Memorial University of Newfoundland

July, 1995

St. John's Newfoundland

ISBN 0-612-06128-0

Canada

Dedication

Dedicated to my very dear wife, Ann and our very dear children, Jimmy and Jacob.

Abstract

Several acoustic investigations were conducted with the near field radiated from a vibrating cantilever beam.

The objective of the first investigation was to experimentally determine the spatial distribution of acoustic intensity close to the beam. Difficulties that occur with acoustic intensity measurements made this a non trivial task and led to the development of an experimental procedure for mapping the spatial distribution of acoustic intensity in the near field. The mapping procedure combined the physics of a closed surface with approximations from an analysis with Taylor's series. The method was successfully tested on the field radiated by the beam. It was then shown that the reliability of the spatial distribution of intensity that resulted from this method could be statistically evaluated from the measured data alone without making assumptions about the nature of the acoustic field.

A second experimental investigation demonstrated the practicality of constructing acoustic intensity with transfer functions. The expression for acoustic intensity, normally formulated in terms of acoustic pressures, was expressed in terms of transfer functions between pressures and the force exciting the cantilever beam.

In the third and last investigation, the source of the acoustic field, the cantilever beam, was modelled with Euler-Bernoulli theory. Elements of modal analysis were used to obtain the modal parameters of the beam and a value for Young's Modulus for the

material of the beam. This vibration model was then used in an integral approximation for the acoustic field close to the beam. The acoustic near field was calculated and compared with experimental measurements. The results were used to examine the distribution of phase in the near field as it pertained to the measurement of acoustic intensity.

Acknowledgments

This work would not have been possible without the support of my supervisors, Dr. Jacques Yves Guigné and Dr. Alex Hay and the support of my employer, the Centre for Cold Oceans Resources Engineering.

TABLE OF CONTENTS

List of Tables

List of Figures

List of Abbreviations and Symbols Used

Symbol	Meaning
c	sound velocity
d	distance between transducers
f	force
F(m)	force, mth spectral component in DFT
h	thickness of beam
k	wave number (2π/wavelength)
K	radius of gyration
l	length of beam
p	acoustic pressure, time domain
P	acoustic pressure, frequency domain
Q	Young's modulus
r	radial distance
$\hat{r}$	radial unit vector
t	time
T	time interval
u	fluid particle velocity
U	fluid particle velocity, frequency domain
W	beam displacement normal to plane, time dependent
Y	beam displacement amplitude
x,y,z	position coordinates
X(m)	acoustic pressure, mth spectral component in DFT
CSIM	closed surface intensity map
FRF	frequency response function
PTF	pressure transfer function
Δ	increment (e.g. increment of time Δt)
δ	delta function
Θ	phase
κ	fluid compressibility
μ	eigenvalue
υ	frequency
ξ	eigenfunction
ρ	solid density
ρ_o	fluid density
σ	standard deviation
Φ	flux of energy crossing surface
Ψ	instantaneous acoustic intensity vector

ω	angular frequency (2π x frequency)
∇	gradient
$< >$	estimate
$\| \|$	magnitude

CHAPTER ONE

INTRODUCTION

Structural vibration radiates sound. Flexural vibration, the usual means by which vibrational energy flows through a structure, produces the most efficient sound radiation [Ross, 1976]. These circumstances make it possible to monitor those modal parameters of a structure associated with the flexural resonances, from the radiated acoustic field. It has been demonstrated that the flexural modes of vibration can be monitored with measurements of the radiated acoustic pressure. Bissinger and Chowdhury [1990] compared natural frequencies and damping values calculated from transfer functions of pressure and force with those calculated from transfer functions of acceleration and force for both a cylindrical bar and a plate. They found good agreement in both cases. Similarly, Okubo and Masuda [1990] used the transfer functions between near field acoustic pressure and excitation force to experimentally obtain the natural frequencies, damping values and mode shapes of T-plate joints.

In addition to acoustic pressure, acoustic intensity, the energy flux vector in the acoustic field, can be measured. Acoustic intensity measurements have historically been used to quantify the power of an acoustic source, the power propagating through a duct, or to establish the attenuation of sound through a panel, [Fahy, 1989]. Near a solid surface acoustic intensity has an advantage over acoustic pressure. Acoustic intensity usually indicates whether the surface is radiating sound (large values normal to the surface) or reflecting sound (small values normal to surface). Unlike acoustic intensity, acoustic

pressure near the surface cannot be readily used to distinguish radiation from reflection because it can be large in both cases.

The research for this thesis occurred within a program to develop acoustic methods to monitor the mechanical behaviour of structures for indications of structural fatigue [Guigné et al, 1992, Klein et al, 1995]. Changes in acoustic intensity and pressure near the surface of cantilever beams were being correlated with the state of fatigue. Estimates of modal parameters were being made from pressure transfer functions. The pattern of acoustic energy flow was being mapped in a horizontal plane parallel to the beam's surface.

Unexpectedly long measurement intervals were required to obtain reproducible estimates of mean acoustic intensity. The search for an explanation led to an examination of the averaging requirements of the measurement. It also became apparent that the measurements of intensity in the near field were not always reliable. The desire to quantify reliability provided the incentive to develop a method for mapping acoustic intensity. Chapter 2 describes acoustic intensity, its measurement, and looks at the measurement statistics of simple acoustic waves. Chapter 3 describes a new procedure for mapping acoustic intensity and the results of its experimental testing.

During the same program, acoustic pressure was being measured twice, once for acoustic intensity measurements, and then again to construct transfer functions between acoustic pressure and force for modal parameter estimates. It was realized that the transfer functions could be used to construct an acoustic intensity normalized with respect to

applied force, eliminating the need for two separate measurements of acoustic pressure. The construction of normalized acoustic intensity is described in Chapter 4.

Several experiments had been conducted to measure transfer functions between pressure and force close to the surface of a cantilever beam. Although the acoustic environment did not lend itself to being easily modelled, there was still a desire to formulate the near field of the cantilever in some approximate fashion and compare it with experiment. Chapter 5 describes the modelling of a cantilever's vibration response. Chapter 6 describes the modelling of the cantilever's near acoustic field from its vibration response and compares the formulated field with experimental measurements. The opportunity is taken to examine the spatial distribution of phase in the near field as it pertains to the measurement of acoustic intensity.

CHAPTER TWO

MEASURING ACOUSTIC INTENSITY

The purpose of this chapter is to provide a background on how the average flux of energy in an acoustic field is measured in practice. For the reader unfamiliar with acoustic intensity a definition is outlined in section 2.1. There are two methods of obtaining a time averaged measurement, one expressed in the time domain and one expressed in the frequency domain. The development of the equations supporting each method are reviewed in sections 2.2 and 2.3. It may be of interest that the expression in the frequency domain was derived without assuming the acoustic field to be stationary or ergodic.

Measurements are always accompanied by errors. Section 2.4 discusses some of the more likely sources of error and notes the work of several authors in this area. One of the decisions faced by the experimentalist is the length of time interval to use to obtain an average value. Section 2.5 examines how moving from the far field to the near field affects this time interval.

2.1 Acoustic Intensity

Acoustic intensity is a vector quantity that comes from considering the change in acoustic energy within a closed volume of fluid. For a fluid of density ρ_o and compressibility κ, with p the acoustic pressure and $\vec{u}$ the fluid particle velocity, it can be shown that (e.g. Morse and Ingard, 1968),

$$\oint_s p\,\vec{u}\cdot d\vec{S} = -\frac{\partial}{\partial t}\int_v \frac{1}{2}\kappa p^2 + \frac{1}{2}\rho_o|\vec{u}|^2\,dV \qquad (2.1)$$

where $\frac{1}{2}\kappa p^2$ is the acoustic potential energy per unit volume, and $\frac{1}{2}\rho_o|u|^2$ is the acoustic kinetic energy per unit volume. The product of acoustic pressure with fluid particle velocity is called the acoustic intensity vector (Ψ) and represents a flow of energy crossing a surface.

$$\vec{\Psi} = p\vec{u} \qquad (2.2)$$

Attempts to measure acoustic intensity met with limited success until the late 1970's when the arrival of digital technology provided the accuracy and stability necessary to make the measurement reliable. A history of development is given by Fahy [1989].

2.2 Time Domain Formulation

An expression can be derived that shows time-averaged acoustic intensity can be measured using the integral of time domain pressure p(t). Consider a time average starting at t_o,

$$\overline{\Psi(t)} = \frac{1}{T}\int_{t_o}^{t_o+T} p(t')\,\vec{u}(t')\,dt' \qquad (2.3)$$

Expressing $\vec{u}(t)$ as a time integral,

$$\overline{\Psi(t)} = \frac{1}{T}\int_{t_o}^{t_o+T} p(t)\int_{-\infty}^{t}\frac{\partial\vec{u}(t')}{\partial t'}\,dt'\,dt \qquad (2.4)$$

Splitting the time integral,

$$\overline{\Psi(t)} = \frac{1}{T}\int_{t_o}^{t_o+T} p(t)\,dt \cdot \int_{-\infty}^{t_o} \frac{\partial \vec{u}(t')}{\partial t'}\,dt' + \frac{1}{T}\int_{t_o}^{t_o+T} p(t) \int_{t_o}^{t} \frac{\partial \vec{u}(t')}{\partial t'}\,dt'\,dt \qquad (2.5)$$

The first term is just the time average of p(t) multiplying a value of particle velocity at time t_o. A long enough measurement interval T, will let the time average of p(t) approach its mean value, zero. Then the first term will not contribute appreciably to the time average leaving,

$$\overline{\Psi(t)} \triangleq \frac{1}{T}\int_{t_o}^{t_o+T} p(t) \int_{t_o}^{t} \frac{\partial \vec{u}(t')}{\partial t'}\,dt'\,dt \qquad (2.6)$$

Using Euler's relation,

$$\frac{\partial \vec{u}}{\partial t} = -\frac{\vec{\nabla} p}{\rho_o} \qquad (2.7)$$

we then substitute for the time derivative in the second integrand to obtain,

$$\overline{\Psi(t)} \triangleq \frac{-1}{\rho_o T}\int_{t_o}^{t_o+T} p(t) \int_{t_o}^{t} \vec{\nabla} p(t')\,dt'\,dt \qquad (2.8)$$

For simplicity we focus on the x component of $\overline{\Psi}(t)$. Consider two pressure transducers designated $p_A(t)$ and $p_B(t)$. The line joining the transducers (A to B) is in the $\overline{x}$ direction. The transducers are separated by a distance d. At the midpoint between the two transducers, the pressure gradient in the x direction is approximated as,

$$\frac{\partial p(t)}{\partial x} \triangleq \frac{p_B(t) - p_A(t)}{d} \qquad (2.9)$$

It will be assumed that the value of d can be chosen for this approximation to hold over

the frequency interval of interest. Similarly, the pressure at the midpoint is approximated as,

$$p(t) \doteq \frac{p_B(t) + p_A(t)}{2} \tag{2.10}$$

With these approximations we have an expression that can be used to measure time averaged acoustic intensity using pressure in the time domain.

$$\overline{I(t)} \doteq \frac{-1}{2\rho_o dT} \int_0^T (p_A(t) + p_B(t)) \cdot \left(\int_0^t [p_B(t') - p_A(t')]\, dt' \right) dt \tag{2.11}$$

This equation is implemented in intensity measuring hardware.

It is also noted in passing that Pavic [1977] showed in the limit $T \to \infty$, that the latter equation reduces to,

$$\overline{I(t)} \to \frac{1}{\rho_o dT} \int_0^T p_B(t) \cdot \left(\int_0^t p_A(t')\, dt' \right) dt \tag{2.12}$$

2.3 Frequency Domain Formulation

An expression can be derived that shows time averaged acoustic intensity can be measured using the frequency spectra of acoustic pressure, P(ω). Using Euler's relation (Eq. (2.7)), particle velocity can be written in terms of pressure in the frequency domain,

$$\bar{U}(\omega) = \frac{\bar{\nabla} P(\omega)}{i\omega\rho_o} \tag{2.13}$$

We shall consider the x component of Ψ(t). The pressure and particle velocity are replaced with their Fourrier representation to give,

$$\begin{aligned}\Psi_x(t) &= p(t)\cdot\bar{u}_x(t)\\ &= \int_{-\infty}^{\infty} P(\omega)\ e^{-i\omega t}\,d\omega \cdot \frac{1}{i\rho_o}\frac{\partial}{\partial x}\int_{-\infty}^{\infty}\frac{P(\omega')}{\omega'}\ e^{-i\omega' t}d\omega'\\ &= \frac{1}{i\rho_o}\int_{-\infty}^{\infty}\int_{-\infty}^{\infty} P(\omega)\frac{1}{\omega'}\frac{\partial}{\partial x}P(\omega')\,e^{-i(\omega+\omega')t}\,d\omega\,d\omega'\end{aligned} \tag{2.14}$$

Take the time average of $\Psi(t)$ over the interval [0,T].

$$\overline{\Psi_x(t)} = \frac{1}{i\rho_o T}\int_0^T\left[\int_{-\infty}^{\infty}\int_{-\infty}^{\infty} P(\omega)\frac{1}{\omega'}\frac{\partial}{\partial x}P(\omega')\,e^{-i(\omega+\omega')t}\,d\omega\,d\omega'\right]dt \tag{2.15}$$

It is assumed that p(t) and u(t) are both zero outside the interval [0,T]. Then the time integration interval can be extended to [-∞,∞] without additional contribution to the time average.

$$\overline{\Psi_x(t)} = \frac{1}{i\rho_o T}\int_{-\infty}^{\infty}\int_{-\infty}^{\infty} P(\omega)\frac{1}{\omega'}\frac{\partial}{\partial x}P(\omega')\left[\int_{-\infty}^{\infty} e^{-i(\omega+\omega')t}\,dt\right]d\omega\,d\omega' \tag{2.16}$$

The quantity in square brackets is $2\pi\delta(\omega+\omega')$. Performing the integration over ω' yields,

$$\overline{\Psi_x(t)} = \frac{-2\pi}{i\rho_o T}\int_{-\infty}^{\infty}\frac{P(\omega)}{\omega}\frac{\partial P(-\omega)}{\partial x}\,d\omega \tag{2.17}$$

Since p(t) is real, $P(-\omega)=P^*(\omega)$.

$$\overline{\Psi_x(t)} = \frac{-2\pi}{i\rho_o T}\int_{-\infty}^{\infty}\frac{P(\omega)}{\omega}\frac{\partial P^*(\omega)}{\partial x}\,d\omega \tag{2.18}$$

The pressure difference between two pressure transducers is used to estimate the pressure gradient, as was done in the time domain formulation (Eq.(2.9)).

$$\frac{\partial P(\omega)}{\partial x} \doteq \frac{P_B(\omega) - P_A(\omega)}{d} \tag{2.19}$$

The pressure at the midpoint is approximated as,

$$P(\omega) \doteq \frac{P_B(\omega) + P_A(\omega)}{2} \tag{2.20}$$

With these approximations,

$$\overline{\Psi_x(t)} \doteq \frac{-2\pi}{i\rho_o T} \int_{-\infty}^{\infty} \left[\frac{P_A(\omega) + P_B(\omega)}{2\omega}\right] \left[\frac{P_B^*(\omega) - P_A^*(\omega)}{d}\right] d\omega \tag{2.21}$$

which reduces to,

$$\overline{\Psi_x(t)} = \frac{-2\pi}{\rho_o d T} \int_{-\infty}^{\infty} \frac{Im[P_A(\omega)\ P_B^*(\omega)]}{\omega}\, d\omega + \frac{i\pi}{\rho_o d T} \int_{-\infty}^{\infty} \frac{|P_B(\omega)|^2 - |P_A(\omega)|^2}{\omega}\, d\omega \tag{2.22}$$

The integrand of the second integral is odd with respect to ω and the second integral vanishes.

$$\overline{\Psi_x(t)} \doteq \frac{-2\pi}{\rho_o d T} \int_{-\infty}^{\infty} \frac{Im[P_A(\omega)\ P_B^*(\omega)]}{\omega}\, d\omega \tag{2.23}$$

The spectral contribution to $\bar{\Psi}_x(t)$ between ω and $\omega+d\omega$ is identified as,

$$\Psi_x(\omega) \doteq \frac{-2\pi}{\omega \rho_o d T} Im\left[P_A(\omega)\, P^*{}_B(\omega)\right] d\omega \tag{2.24}$$

This cross spectral formulation for intensity was derived by Fahy [1977].

Now, $p_A(t)$ and $P_A(\omega)$ are related by,

$$P_A(\omega) = \frac{1}{2\pi} \int_{-\infty}^{\infty} p_A(t)\ e^{i\omega t}\ dt \tag{2.25}$$

Since p(t) is zero outside the interval [0,T],

$$P_A(\omega) = \frac{1}{2\pi} \int_{0}^{T} p_A(t)\ e^{i\omega t}\ dt \tag{2.26}$$

To convert to discrete measurements, the integral is approximated by a summation over N points, with $T=N\Delta t$.

$$\int_0^T p_A(t)\ e^{i\omega t}\ dt \rightarrow \sum_{n=-\frac{N}{2}}^{\frac{N}{2}} p_A(n\Delta t)\ e^{i\omega n\Delta t}\ \Delta t \tag{2.27}$$

Choosing discrete values of ω, $\omega_m=2\pi m/T$, $m=\{0,1,...,N/2\}$, yields,

$$\begin{aligned} &\rightarrow \frac{T}{N} \sum_{n=-\frac{N}{2}}^{\frac{N}{2}} p_A(n\Delta t)\ e^{\frac{i2\pi mn}{N}} \\ &\rightarrow T\ X_A(m) \end{aligned} \tag{2.28}$$

where $X_A(m)$ is the mth spectral coefficient in a DFT of $p_A(t)$. Then, the spectral contribution to $\bar{\Psi}_x(t)$ between $\omega_m-\Delta\omega/2$ and $\omega_m+\Delta\omega/2$ ($\Delta\omega=2\pi/T$) is,

$$\overline{\Psi_x(m)} \doteq \frac{-1}{\omega_m \rho_o d}\ Im\left[X_A(m)\, X^*_B(m)\right] \tag{2.29}$$

This formulation for intensity was derived by Chung [1978]. Both Fahy and Chung assumed stationarity and ergodicity to arrive at their results. The same result has been derived here with a windowed process (p(t) and u(t) assumed to be zero outside the measurement interval [0,T]). A windowed process is a realistic portrayal of a typical

measurement. A windowed process does not demand specific correlation properties like those of a stationary process.

Writing the DFT coefficients in terms of their magnitudes and phases illustrates an important aspect of the measurement.

$$\overline{I_x(m)} \doteq \frac{-1}{\omega_m \rho_o d} \; |X_A(m)||X^*_B(m)| \sin(\theta_A(m) - \theta_B(m)) \qquad (2.30)$$

There must be a measureable phase difference between the pressures at A and B for the measured time averaged intensity to be non zero. In practice, if the hardware phase resolution is inadequate, the measurement will probably be unreliable.

2.4 Sources of Error

Both methods use two microphones with fixed spacing to approximate the pressure gradient component along the line joining the microphones with their pressure difference. Thompson and Tree [1981] examined the error introduced by this finite difference approximation and showed that it depends not only on the ratio of microphone spacing to wavelength (i.e. kd), but also on the ratio of the microphone spacing to the distance separating the measurement position from the source location (i.e. d/r). They showed that to maintain the same level of error, larger microphone spacings are required in the near field than the far field.

Over and above the error introduced by the finite difference approximation itself, equation 2.30 illustrates that measurement accuracy depends on accurately resolving the difference between $\Theta_A(m)$ and $\Theta_B(m)$. The trend is for $\Theta_A(m)$-$\Theta_B(m)$ to decrease as the

frequency decreases, for a fixed microphone spacing. Real pressure transducers have individual phase response characteristics that vary with frequency. As the frequency drops, there will come a point where the difference between transducer phase responses (microphone phase mismatch) is no longer small compared to $\Theta_A(m)-\Theta_B(m)$, and a significant bias error is then introduced. In general, the effects of microphone phase mismatch (and similarly instrumentation channel phase mismatch) become problematic at low frequencies and in highly reactive acoustic fields, presenting the greatest difficulty in intensity measurement hardware design [Pascal and Carles, 1982]. This bias error can be reduced by repeating each measurement with microphone positions reversed [Chung, 1978]. Alternatively, if the phase mismatch between the microphones is measured, the intensity measurements can be corrected [Krishnappa, 1981].

Statistical error can be appreciable when for example a lot of reverberation exists. This error has been examined by several authors. It is usually modelled by assuming that there are two sound fields, one the object of measurement, the other extraneous. Seybert [1981] related statistical error to the coherence between the two pressure signals used in the measurement. Seybert used the assumption that the desired and undesired sound fields were uncorrelated. Then Dyrlund [1983] related the coherence to the pressure intensity index by assuming the extraneous sound field to be diffuse. Experimental measurements have shown some agreement with these formulations of statistical error [Pepin 1984]. Asymptotic expressions for standard error in terms of a field factor were subsequently developed by Pascal [1986].

However the use of coherence in error estimation has been questioned. Chung [1981] showed that ordinary coherence and the cross spectral method are not always well related. Jacobsen and Neilsen [1987] noted that measured coherence can be a function of spectral resolution. Watkinson [1986] pointed out that coherence estimates can be affected by bias error, questioned the validity of assuming the desired and undesired components in a sound field to be uncorrelated in all cases and suggested returning to calculations of mean and standard deviation.

The bias errors that have been discussed to this point can be mitigated by recognizing hardware limitations such as microphone phase mismatch, and the random errors can be quantified with statistical analysis. There are other phenomena that may or may not cause significant error. For example, each microphone disturbs the sound field, and affects what the other microphone sees. Tichy [1981] demonstrated experimentally the disturbance to one microphone caused by the presence of a second microphone, noting that the disturbance increased with frequency and tended to affect measured phase more than amplitude. (It would be very difficult to estimate the error caused by the presence of both microphones.) As a second example, in mapping the flow of near field intensity a phenomenon called a vortex can be encountered. It is not clear whether this feature is an added complication to measurement. The vortex was first postulated as a closed loop of energy [Schultz et al, 1975], but in fact, instantaneous energy flows through the vortex; the vortex itself only applies to the net energy component of intensity [Mann et al, 1987].

The effort of many individuals to quantify errors and disturbances suggests one

would want to proceed cautiously in making measurements of acoustic intensity.

2.5 Effect of the Near Field on Measurement Interval

Whether in the time domain or the frequency domain, the calculated average intensity is for the measurement interval [0,T]. The length of T required to obtain an estimate that approaches the mean value of $\Psi(t)$ for $T\rightarrow\infty$, depends on the statistics of $\Psi(t)$. The effect of being in the near field on the measurement interval can be illustrated with a spherically symmetric wave of amplitude A,

$$\begin{aligned} p(r,t) &= \frac{A}{r}\cos(kr-\omega t) \\ \bar{u}(r,t) &= \frac{A}{\rho_o c r}\left(\cos(kr-\omega t) - \frac{\sin(kr-\omega t)}{kr}\right)\hat{r} \end{aligned} \tag{2.31}$$

The instantaneous intensity $\Psi(t)$ is,

$$p(r,t)\cdot\bar{u}(r,t) = \frac{A^2\hat{r}}{2\rho_o c r^2}\left[1+\cos 2(kr-\omega t) - \frac{\sin 2(kr-\omega t)}{kr}\right] \tag{2.32}$$

and the time average over [0,T],

$$\overline{\Psi(t)} = \frac{1}{T}\int_0^T p(r,t)\bullet\bar{u}(r,t)\,dt \tag{2.33}$$

is,

$$\overline{\Psi(t)} =,$$

$$\frac{A^2\hat{r}}{2\rho_o c r^2}\left[1+\frac{\sin(2kr)-\sin 2(kr-\omega T)}{2\omega T} + \frac{\cos(2kr)-\cos 2(kr-\omega T)}{2\omega T k r}\right] \tag{2.34}$$

In the limit $T\to\infty$ ($r\neq 0$),

$$\overline{\Psi(t)} \to \frac{A^2 f}{2\rho_o c r^2} \tag{2.35}$$

Then, from Eq.(2.34), to get an estimate of $\Psi(t)$ that approaches the value in Eq.(2.35) requires,

$$\begin{aligned} \omega T &\blacktriangleright 1 \\ \omega T k r &\blacktriangleright 1 \end{aligned} \tag{2.36}$$

The latter condition shows that in the near field ($kr<1$), as the point of measurement moves closer to the source, the measurement interval will need to be increased. This result is a consequence of the dependence of instantaneous intensity on $(kr)^{-1}$ in the near field. Consider the time averaged mean square,

$$\overline{(\Psi(t)-\bar{\Psi}(t))^2} = \frac{1}{T}\int_0^T (\Psi(t)-\bar{\Psi}(t))^2\, dt \tag{2.37}$$

Inserting the forms of $\Psi(t)$ and $\bar{\Psi}(t)$, given in Eq.'s (2.32) and (2.34) respectively, yields,

$$\overline{(\Psi(t)-\bar{\Psi}(t))^2} = \frac{1}{T}\left[\frac{A^2}{2\rho_o c r^2}\right]^2 \int_0^T \left(F + \frac{\sin 2(kr-\omega t)}{kr} - \cos 2(kr-\omega t)\right)^2 dt \tag{2.38}$$

where,

$$F = \frac{\sin(2kr) - \sin 2(kr-\omega T)}{2\omega T} + \frac{\cos(2kr) - \cos 2(kr-\omega T)}{2\omega T k r} \tag{2.39}$$

Integration yields,

$$\overline{(\Psi(t)-\overline{\Psi(t)})^2} = \left[\frac{A^2}{2\rho_o c r^2}\right]^2 \left[\frac{1}{2}\left(1+\frac{1}{k^2r^2}\right)+F^2+\frac{F_1}{8\omega T k^2 r^2}+\frac{F_2}{2\omega T k r}+\frac{F_3}{8\omega T}\right] \tag{2.40}$$

where,

$$\begin{aligned} F_1 &= \sin 4(kr-\omega T)-\sin(4kr) \\ F_2 &= \frac{\cos(4kr)-\cos 4(kr-\omega T)}{2}-2F(\cos(2kr)-\cos 2(kr-\omega T)) \\ F_3 &= \sin(4kr)-\sin 4(kr-\omega T)-\frac{F}{\omega T}(\sin(2kr)-\sin 2(kr-\omega T)) \end{aligned} \tag{2.41}$$

Assuming ωT>>1 and ωTkr>>1 (and therefore F<<1), Eq.(2.40) reduces to,

$$\overline{(\Psi(t)-\overline{\Psi(t)})^2} \rightarrow \left[\frac{A^2}{2\rho_o c r^2}\right]^2 \frac{1}{2}\left(1+\frac{1}{(kr)^2}\right) \tag{2.42}$$

Eq.(2.42) shows that in the near field with kr<1, the variance increases as kr decreases. In particular, if the instantaneous intensity from a spherical wave were sampled continuously, with ωTkr >>1, then from Eq.'s (2.35) and (2.42), we would anticipate a standard deviation to mean ratio of approximately,

$$\frac{\sqrt{\overline{(\Psi(t)-\overline{\Psi(t)})^2}}}{\overline{\Psi(t)}} \doteq \frac{1}{\sqrt{2}}\sqrt{1+\frac{1}{(kr)^2}} \tag{2.43}$$

which, for small values of kr, would exceed unity.

These two calculations with a spherically symmetric wave suggest that in the near field (kr<1), estimates of time averaged intensity will be more difficult to obtain, and prone to larger statistical variation than in the far field (kr>>1).

The interaction between two frequency components in the acoustic field can also make estimates of time averaged intensity more difficult to obtain (example given in Appendix A). The effect of the interaction can be reduced by requiring $\Delta\omega T>>1$, where $\Delta\omega$ is the separation between the frequencies.

2.6 Summary

Two methods of processing to obtain time averaged acoustic intensity, in the frequency domain, and in the time domain, were reviewed. It was noted that the frequency domain method was equivalent to a windowed process that assumes zero intensity outside the measurement interval.

The measurement of acoustic intensity requires good phase resolution and suffers from bias errors when the limits of phase resolution are exceeded. In general the demands on phase resolution increase at lower frequencies.

In the near field, the time interval to obtain a good estimate of average intensity may depend on position. An example with spherical waves showed that in the near field the statistical distribution of instantaneous intensity broadened as the distance to the source decreased. As a result, longer measurement intervals were shown to be necessary in the near field to obtain good estimates of mean intensity than in the far field.

It could be anticipated that a series of measurements to establish the spatial distribution of acoustic intensity in the near field of a source would contain a range of errors. The challenge would be to decide whether the measurements portray the distribution reasonably accurately.

CHAPTER THREE

MAPPING ACOUSTIC INTENSITY

This chapter is concerned with how to measure the spatial distribution of time averaged acoustic intensity in the near ı eld. The main topic is a new procedure that was developed for this purpose. This procedure provides a recipe for data collection, and also a numerical means of assessing the quality of the collected data.

Section 3.1 begins with an overview of other methods for mapping acoustic intensity and discusses the motivation to develop a new method. The theoretical side of the new method is covered in section 3.2. The actual mapping procedure is described in section 3.3. The experimental testing and validation of the procedure is described in section 3.4. Then, a numerical measure of reliability is demonstrated for intensity maps generated by this method in section 3.5. The selection of averaging time for data collection is covered separately in section 3.6.

The contents of this chapter have been summarized in Klein and Guigne, [1995].

3.1 Mapping Procedures

Different procedures have been suggested for mapping the spatial distribution of acoustic intensity near a vibrating surface. Pressure has been phase referenced to surface acceleration using a cross spectrum between a surface mounted accelerometer and a mobile microphone [Petterson, 1979]. The one microphone was used to make all acoustic measurements required to construct the desired acoustic intensity vectors. This approach should have eliminated phase mismatch error from calculated intensity.

A large planar array of microphones was placed in close proximity to a surface in order to perform near field acoustic holography [Williams and Maynard, 1981]. Several acoustic products were constructed, including the vector distribution of acoustic intensity.

Probably the most common method of mapping acoustic intensity consists of sampling the intensity vector on a grid of regularly spaced points in a plane using a microphone pair with fixed spacing. Regardless of the method employed, the usual objective is to determine the distribution of x,y and z components of intensity across a plane.

We had experienced the effects of errors in attempting to map the spatial distribution of acoustic intensity in the near field of a vibrating cantilever beam (e.g. poor reproducibility). Our measurement capability at the time was limited to two real time acoustic intensity analyzers and a few microphones, which precluded measurements with an accelerometer, and likewise with a microphone array. This situation provided the incentive to develop a procedure to meet our needs. The procedure described in the sections to follow was developed with 3 requirements in mind (discussed below).

During the mapping process the grid point spacing may be reduced to sample the intensity distribution on a finer scale. **A mapping procedure should indicate when sufficient sampling has been achieved.**

Acoustic intensity describes energy flux crossing normal to a surface. Each measurement should have a bounded normal surface area to which it applies. Let us assume that the mapping plane lies in the x-y plane. For the z components normal to the

mapping plane, the plane can be subdivided into equal areas centred on each measurement location. The net flux crossing the plane can be then related to the z components and their associated individual areas. However, the x and y intensity components all lie in the plane. The sizes of the normal surface areas to which they apply is not so well defined. **A mapping procedure should delineate the boundaries of the normal surfaces associated with all the measured intensity components.**

Near field measurements are very demanding on the measuring hardware's phase resolution. Simultaneous measurement of several frequency bands with one fixed microphone spacing introduces the possibility that phase resolution will be adequate for some bands and inadequate for other bands. It is also difficult to anticipate the required microphone spacing because the phase difference between microphone locations is unlikely to be a simple function of acoustic wavelength and microphone spacing. With the possibility of poor phase resolution, **a mapping procedure should provide an objective means of assessing whether the measured intensity distribution is a close facsimile of the actual distribution.**

3.2 Approximations Using a Closed Surface

Consider a box, formed by the intersection of surfaces normal to six intensity measurements pointing away from (x_0, y_0, z_0) as shown in Fig. 3.1. This box will be referred to as a "cell".

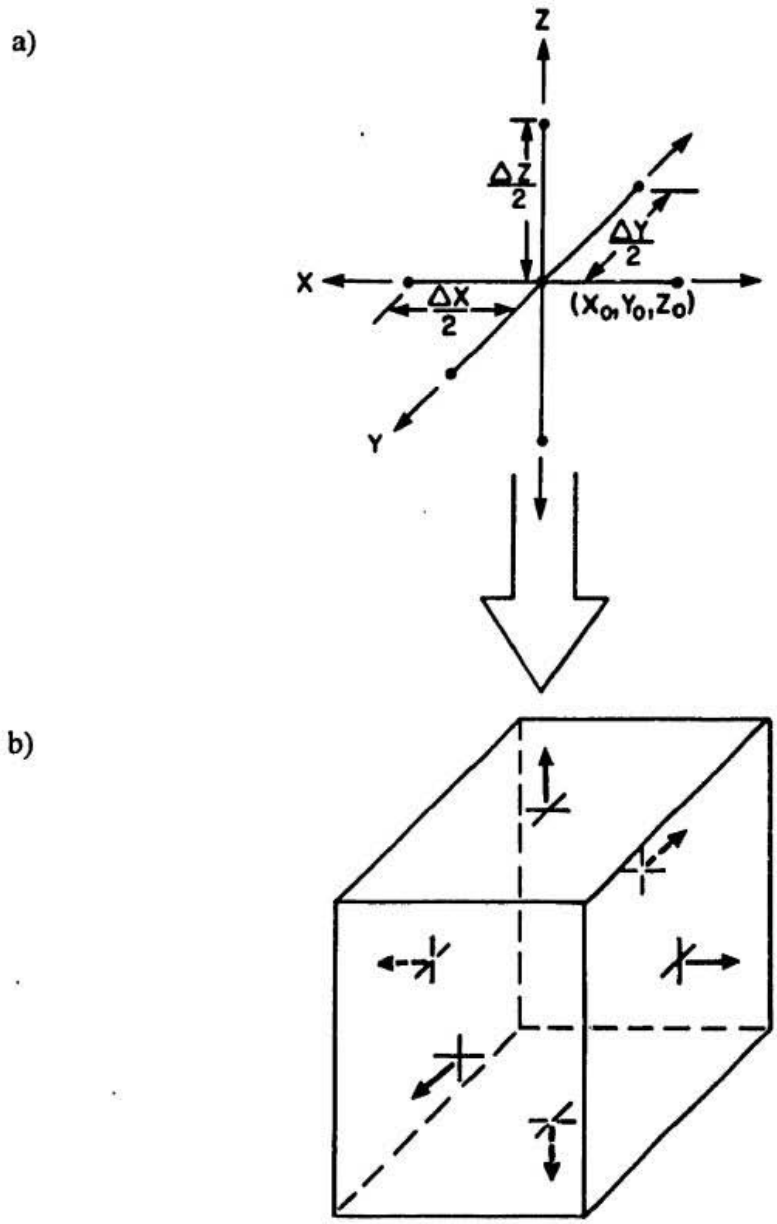

Figure 3.1: The intensity measurements associated with a cell. (a) Six unit vectors point away from the interior point (x_o,y_o,z_o). (b) The surfaces normal to the unit vectors define a cell.

The x component of intensity is measured at $(x_o-\Delta x/2,y_o,z_o)$ and $(x_o+\Delta x/2,y_o,z_o)$. The y component of intensity is measured at $(x_o,y_o-\Delta y/2,z_o)$ and $(x_o,y_o+\Delta y/2,z_o)$. The z component of intensity is measured at $(x_o,y_o,z_o-\Delta z/2)$ and $(x_o,y_o,z_o+\Delta z/2)$. With this arrangement we will show that as the cell dimensions $(\Delta x,\Delta y,\Delta z)$ are reduced,

i) the intensity component measured normal to the centre of each cell wall can be related to the average intensity crossing that wall, and

ii) the six intensity components, each normal to one of the cell walls, can be related to the components of the intensity vector at the centre of the cell.

Developing relationships between the intensity components, as described in i) and ii), will allow us to use the "cell" as the basic building block for mapping intensity over an extended surface.

Let $\Psi(x, y, z)$ be the acoustic intensity vector.

$$\Psi(x,y,z) = \Psi_x(x,y,z)\,\vec{i} + \Psi_y(x,y,z)\,\vec{j} + \Psi_z(x,y,z)\,\vec{k} \qquad (3.1)$$

Consider the integral of the x component of Ψ across one of the faces of the cell parallel to the y-z plane. For example,

$$\overline{\Psi_x(x_0+\frac{\Delta x}{2},y,z)} = \frac{\int_{y_o-\frac{\Delta y}{2}}^{y_o+\frac{\Delta y}{2}}\int_{z_o-\frac{\Delta z}{2}}^{z_o+\frac{\Delta z}{2}} \Psi_x(x_0+\frac{\Delta x}{2},y,z)\,dydz}{\Delta y\,\Delta z} \qquad (3.2)$$

The integrand is replaced with its Taylor's expansion about point (x_0, y_0, z_0).

$$\Psi_x(x,y,z) = \Psi_x(x_0,y_0,z_0) + (x-x_0)\frac{\partial \Psi_x}{\partial x} + (y-y_0)\frac{\partial \Psi_x}{\partial y} + (z-z_0)\frac{\partial \Psi_x}{\partial z} + \ldots \quad (3.3)$$

Performing the integration produces a series that contains the Taylor's expansion of $\Psi_x(x_0+\Delta x/2,y_0,z_0)$ about (x_0, y_0, z_0) with additional terms. The terms representing $\Psi_x(x_0+\Delta x/2,y_0,z_0)$ have been collected in Eq.(3.4), followed by the lowest order terms in Δy and Δz.

$$\overline{\Psi_x\left(x_0+\frac{\Delta x}{2},y,z\right)} = \Psi_x\left(x_0+\frac{\Delta x}{2},y_0,z_0\right) + \frac{1}{6}\left(\frac{\Delta y}{2}\right)^2\frac{\partial^2\Psi_x}{\partial y^2} + \frac{1}{6}\left(\frac{\Delta z}{2}\right)^2\frac{\partial^2\Psi_x}{\partial z^2} + \ldots \quad (3.4)$$

From Eq.(3.4), approximating the average value of $\Psi_x(x_0+\Delta x/2,y,z)$ over the cell wall at $x=x_0+\Delta x/2$ by $\Psi_x(x_0+\Delta x/2,y_0,z_0)$ neglects terms of which the lowest order are,

$$\overline{\Psi_x\left(x_0+\frac{\Delta x}{2},y,z\right)} - \Psi_x\left(x_0+\frac{\Delta x}{2},y_0,z_0\right) = \frac{1}{6}\left[\left(\frac{\Delta y}{2}\right)^2\frac{\partial^2\Psi_x}{\partial y^2} + \left(\frac{\Delta z}{2}\right)^2\frac{\partial^2\Psi_x}{\partial z^2}\right] + \ldots \quad (3.5)$$

The steps from Eq.'s (3.2) to (3.5) can be repeated to obtain the spatial average of the intensity component normal to each of the other 5 cell walls (i.e. spatial averages for $\Psi_x(x_0-\Delta x/2,y,z)$, $\Psi_y(x,y_0\pm\Delta y/2,z)$, and $\Psi_z(x,y,z_0\pm\Delta z/2)$. In each case an equation similar to Eq.(3.5) is obtained.

Now the flux of Ψ leaving the cell, Φ_{cell},

$$\Phi_{cell} = \int_{y_0-\frac{\Delta y}{2}}^{y_0+\frac{\Delta y}{2}} \int_{z_0-\frac{\Delta z}{2}}^{z_0+\frac{\Delta z}{2}} \left[\Psi_x(x_0+\frac{\Delta x}{2}, y, z) - \Psi_x(x_0-\frac{\Delta x}{2}, y, z) \right] dydz +$$
$$\int_{x_0-\frac{\Delta x}{2}}^{x_0+\frac{\Delta x}{2}} \int_{z_0-\frac{\Delta z}{2}}^{z_0+\frac{\Delta z}{2}} \left[\Psi_y(x, y_0+\frac{\Delta y}{2}, z) - \Psi_y(x, y_0-\frac{\Delta y}{2}, z) \right] dxdz + \qquad (3.6)$$
$$\int_{x_0-\frac{\Delta x}{2}}^{x_0+\frac{\Delta x}{2}} \int_{y_0-\frac{\Delta y}{2}}^{y_0+\frac{\Delta y}{2}} \left[\Psi_z(x, y, z_0+\frac{\Delta z}{2}) - \Psi_z(x, y, z_0-\frac{\Delta z}{2}) \right] dxdy$$

will be approximated as,

$$\Phi_{cell} \doteq \left[\Delta y \Delta z \left(\Psi_x(x_0+\frac{\Delta x}{2}, y_0, z_0) - \Psi_x(x_0-\frac{\Delta x}{2}, y_0, z_0) \right) + \right.$$
$$\Delta x \Delta z \left(\Psi_y(x_0, y_0+\frac{\Delta y}{2}, z_0) - \Psi_y(x_0, y_0-\frac{\Delta y}{2}, z_0) \right) + \qquad (3.7)$$
$$\left. \Delta x \Delta y \left(\Psi_z(x_0, y_0, z_0+\frac{\Delta z}{2}) - \Psi_z(x_0, y_0, z_0-\frac{\Delta z}{2}) \right) \right]$$

With the 6 equations of the form of Eq.(3.5) it can be shown that this approximation neglects terms of order,

$$\left[\frac{1}{24} \left(\Delta x \Delta y^3 \Delta z \frac{\partial^3 \Psi_x}{\partial x \partial y^2} + \Delta x \Delta y \Delta z^3 \frac{\partial^3 \Psi_x}{\partial x \partial z^2} \right.\right.$$
$$+ \Delta x^3 \Delta y \Delta z \frac{\partial^3 \Psi_y}{\partial x^2 \partial y} + \Delta x \Delta y \Delta z^3 \frac{\partial^3 \Psi_y}{\partial y \partial z^2} \qquad (3.8)$$
$$\left.\left. + \Delta x^3 \Delta y \Delta z \frac{\partial^3 \Psi_z}{\partial x^2 \partial z} + \Delta x \Delta y^3 \Delta z \frac{\partial^3 \Psi_z}{\partial y^2 \partial z} \right) + \ldots \right]$$

The components of the vector Ψ at the centre of the cell will be approximated from,

$$\Psi_x(x_0,y_0,z_0)=\frac{1}{2}\left[\Psi_x(x_0+\frac{\Delta x}{2},y_0,z_0)+\Psi_x(x_0-\frac{\Delta x}{2},y_0,z_0)\right]$$
$$\Psi_y(x_0,y_0,z_0)=\frac{1}{2}\left[\Psi_y(x_0,y_0+\frac{\Delta y}{2},z_0)+\Psi_y(x_0,y_0-\frac{\Delta y}{2},z_0)\right] \qquad (3.9)$$
$$\Psi_z(x_0,y_0,z_0)=\frac{1}{2}\left[\Psi_z(x_0,y_0,z_0+\frac{\Delta z}{2})+\Psi_z(x_0,y_0,z_0-\frac{\Delta z}{2})\right]$$

which, because of the anti symmetry in the expansions (Eq.(3.3)) neglects terms of order,

$$\frac{(\Delta x)^2}{8}\frac{\partial^2\Psi_x}{\partial x^2}+\ldots\ ,\ \frac{(\Delta y)^2}{8}\frac{\partial^2\Psi_y}{\partial y^2}+\ldots\ ,\ \frac{(\Delta z)^2}{8}\frac{\partial^2\Psi_z}{\partial z^2}+\ldots \qquad (3.10)$$

respectively. Eq.'s (3.7) and (3.9) are the basic approximations used to develop an intensity mapping procedure based on a closed surface. Since the point of evaluation of the derivatives remains constant, these approximations should improve as Δx, Δy, or Δz decrease (i.e., when cell dimensions are reduced).

3.3 Mapping With a Closed Surface

The mapping process begins by establishing an imaginary box which encloses the mapping plane of interest. Assume the mapping surface to be a rectangle in the x-y plane. This surface would be enclosed by a box like that shown in Fig. 3.2, with width and length much greater than depth. The objective is to partition the box into individual cells, make measurements of intensity normal to the cell walls and apply the approximations of the previous section to construct the intensity vector at the centre of each cell. In the beginning there is no information to use to establish cell size. We begin by choosing an arbitrary size.

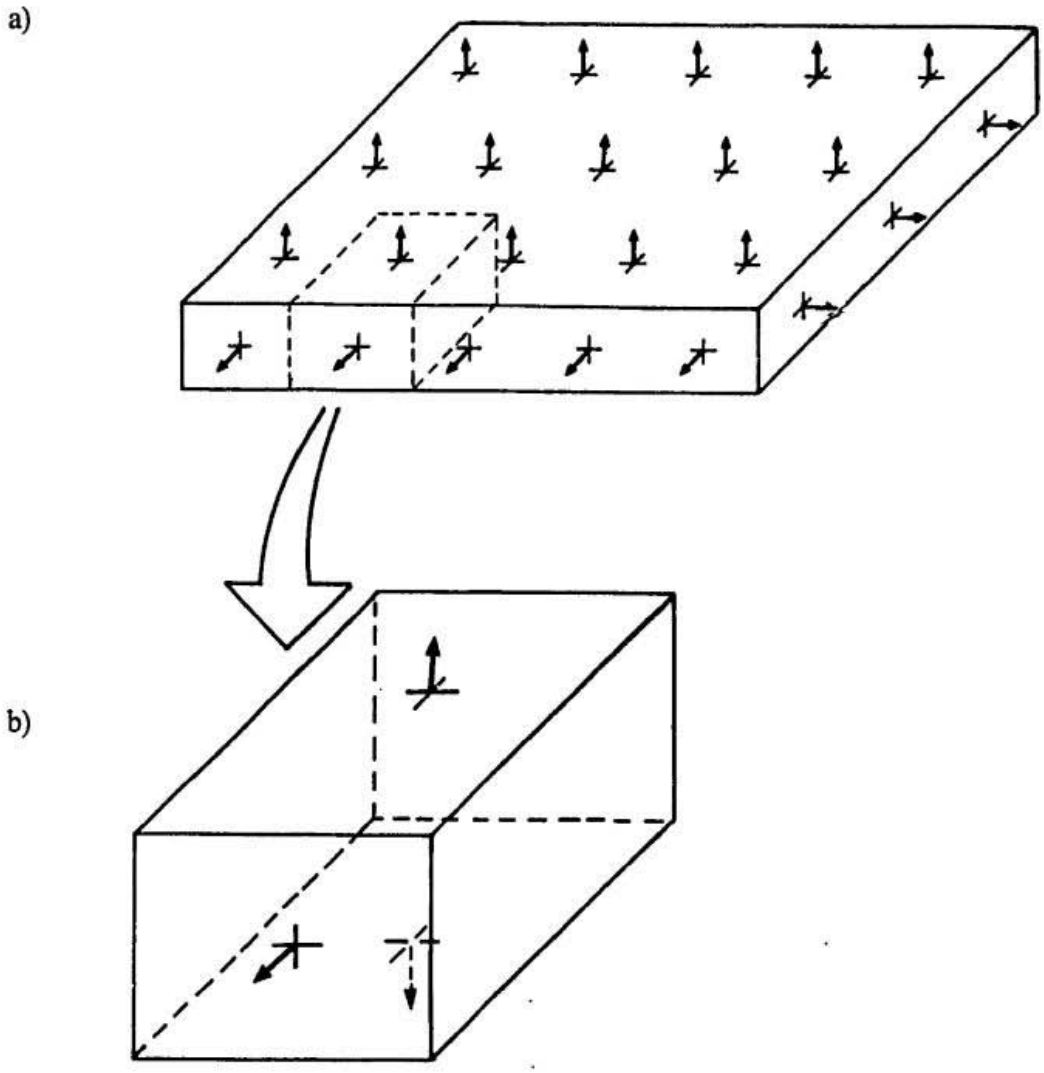

Figure 3.2: (a) A rectangular box comprised of multiple cells. (b) An enlarged view of one cell. Intensity measurements are made initially only on cell walls common to the exterior of the box.

Intensity measurements are made at regularly spaced intervals normal to the surface of the box. In Fig. 3.2 the measurements form a 5 by 3 grid pattern in the horizontal plane. The measurement spacing acts to partition the box into 15 cells. The boundary of one of the cells is shown in the figure. The intensity measurements normal to the box surface are used to estimate the net acoustic energy leaving the box. Then, keeping the overall box dimensions constant, the number of cells are increased, by adding additional measurement locations at regular intervals on the exterior of the box. This reduces cell size.

Each time the number of cells is increased, the apparent net flux leaving the box, $\Phi_{\text{net flux}}$, is calculated using the approximation in the previous section, where N is the number of exterior cell surfaces.

$$\Phi_{Net\ Flux} = \sum_{i=1}^{N} (\Psi_{isurface})_i \cdot A_i \qquad (3.11)$$

A_i equals the area of the ith cell face on the surface of the box, and $(\Psi_{surface})_i$ equals the intensity measured normal to A_i. In addition, the sum of apparent absolute flux, $\Phi_{absolute}$, is calculated.

$$\Phi_{absolute} = \sum_{i=1}^{N} |(\Psi_{isurface})_i \cdot A_i| \qquad (3.12)$$

A lossless fluid medium is assumed with no sources enclosed by the box. The net flux of acoustic intensity out of the box should be zero. In the absence of measurement errors, the decision that an adequately small cell size resolution has been achieved is based

on the expectation that the apparent net flux tends to zero with decreasing cell size while the total absolute flux tends to a constant value. This is taken to indicate that sufficient sampling of the flux crossing the surfaces has been achieved.

The effect of positioning errors and measurement errors require that the decision making process also include,

$$\left| \sum_{i=1}^{N} (\Psi_{intensity})_i \cdot A_i \right| < \sum_{i=1}^{N} \sigma_i \cdot A_i \qquad (3.13)$$

where σ_i is the measured standard deviation of $(\Psi_{surface})_i$. Once cell size is established, measurements of the components normal to the interior cell walls are made to construct the intensity vector at the centre of each cell.

3.4 Experimental Validation

The described mapping procedure was tested near the surface of a vibrating cantilever beam in a room with finished walls and ceiling, and a concrete floor. The experimental setup is shown in Fig. 3.3 including cantilever dimensions and reference coordinate axes. The cantilever was excited at its third beam bending mode frequency of 315.0 Hz. Measurements of acoustic intensity were made with a Brüel and Kjær Sound Intensity Analyzer System Type 3360 using a matched pair of type 4181 microphones and a 50 mm spacer. Two data sets were collected. The first set was the acoustic intensity measured according to the described procedure (construction of intensity vector components at the centre of each cell from measurements made normal to the cell walls). This data set is identified using the subscript CSIM (Closed Surface Intensity Mapping).

a)

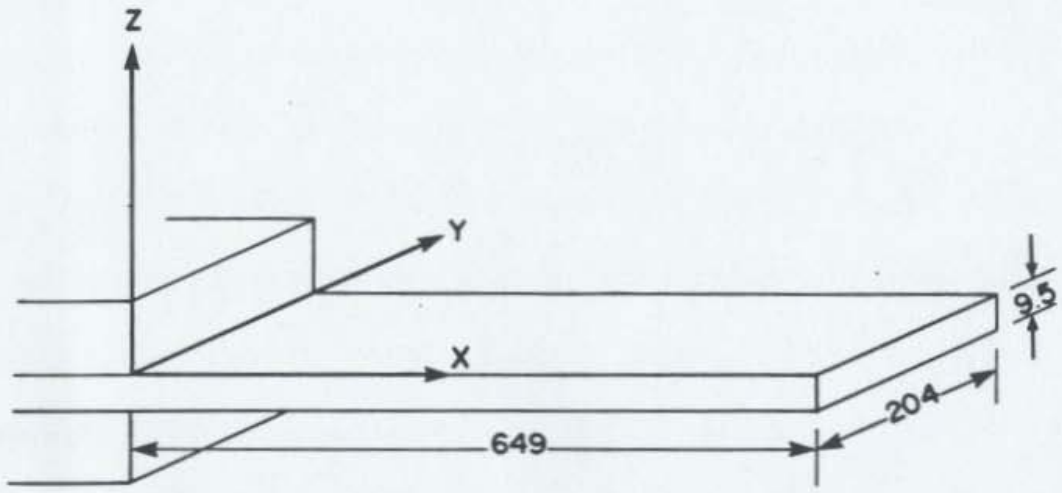

b)

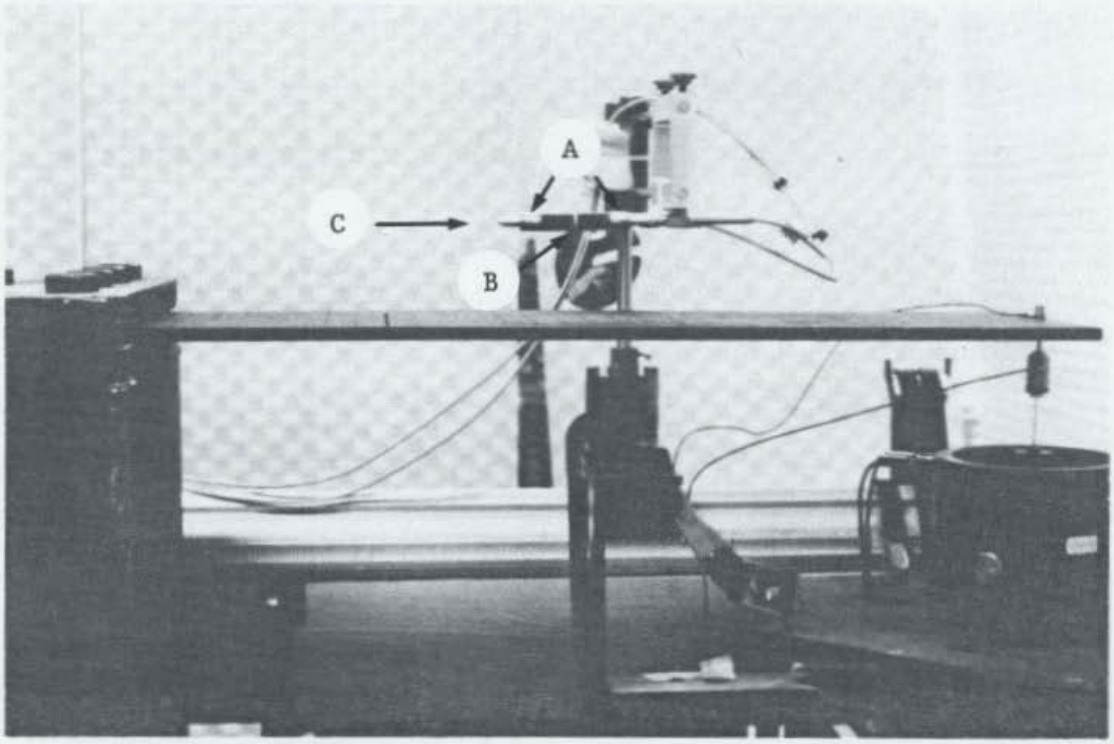

Figure 3.3: The experimental setup. (a) Cantilever dimensions (in mm) and coordinate axes. (b) Photograph of typical measurement configuration. Two microphones (A) were separated by a 50 mm spacer (B). The line joining the microphones defined the direction of measurement (C) above the cantilever beam.

The second data set consisted of direct measurements of the three intensity components at the centre of each cell. A comparison was then made between the acoustic intensity vector that the mapping procedure constructed at each cell centre (CSIM) and the vector actually measured at cell centre. For both data sets, time averaged acoustic intensity was collected in third octave bands by the intensity analyzing system using a 16 second averaging time constant. Ten samples of time averaged intensity in the 315 Hz third octave band, collected 16 seconds apart were used to calculate a mean and standard deviation for each intensity measurement. Alignment of acoustic probe position and orientation was done manually. The data sets were collected over a period of 7 days. Measurements were repeated when excessive external noise or floor vibration occurred, or excessive variation occurred in cantilever vibration amplitude. Variability occurred in cantilever vibration levels due to slight sagging of the exciter support. Average cantilever acceleration amplitude varied no more than about ± 7 % for the accepted intensity measurements.

The mapping plane was located 65 mm above the surface of the cantilever. This was the lowest altitude above the cantilever that could be achieved with the acoustic probe spacing while allowing for z direction measurements. A box height of 10 mm was used. The bottom of the box was located at z=60 mm and the top of the box at z=70 mm. The x-y coordinates of the corners of the box were (98,41), (98,163), (551,41), and (551,163) mm. The CSIM (Closed Surface Intensity Map) was initially begun with a coarse grid of N_x=3 (3 cells in the x direction) by N_y=3 (3 cells in the y direction). After all the

intensity components normal to the box were measured, the grid was divided in the x direction increasing N_x to 5 and the missing normal intensity components measured. The grid was again divided in the x direction increasing N_x to 9 and the missing normal intensity components measured. Table 3.1 lists the parameters that were calculated at the completion of measuring the intensity components normal to the box surface for each grid.

From Table 3.1, the sum of absolute flux out of the box stabilised once the number of grid points reached N_x=9. The net flux leaving the box remained close to zero for all 3 grids and always remained below the flux calculated with standard deviations. N_y was not increased because it had been observed in a previous test that increasing N_y to 5 did not have a significant effect on the decision parameters (minimal variation of Ψ in y direction).

With the final grid established, the missing intensity components defining the

Table 3.1 Surface component information versus grid size.

Grid		$\Sigma (\Psi_{\perp surface})_i A_i$	$\Sigma (\sigma_i A_i)$	$\Sigma \lvert (\Psi_{\perp surface})_i A_i \rvert$
N_x	N_y	μWatts	μWatts	μWatts
3	3	0.039	0.057	2.70
5	3	0.004	0.089	3.36
9	3	-0.025	0.092	3.57

individual cell walls were then measured. The components of the intensity vector at the centre of each cell were calculated using Eq.(3.9).

Direct measurement of intensity components at the centre of each cell took place in parallel with CSIM measurements. Consequently, both data sets were collected over approximately the same time frame. Several statistical tests (e.g. linear regression, paired difference) were applied to the collected data to evaluate how well the CSIM method had estimated the intensity vector measured at cell centre. The linear regression results will be presented here. The results of the other tests were satisfactory. (Appendix B tabulates and compares the two data sets, and shows the results of a paired difference test.)

Linear regression was used to obtain a linear relation of the form, $\Psi_{\text{calculated by CSIM}} = a \cdot \Psi_{\text{measured}} + b$. The x, y and z components were analyzed separately, with N = 27 pairs for each component. The linear regression results are given in the Table 3.2 (r is the correlation coefficient). Fig. 3.4 illustrates the paired data for each vector component and the line of best fit.

Table 3.2 Linear regression results

Component	a	b	r
x	1.0523	1.2406	0.989
y	0.8426	0.0519	0.965
z	0.9746	-1.1837	0.999

a)

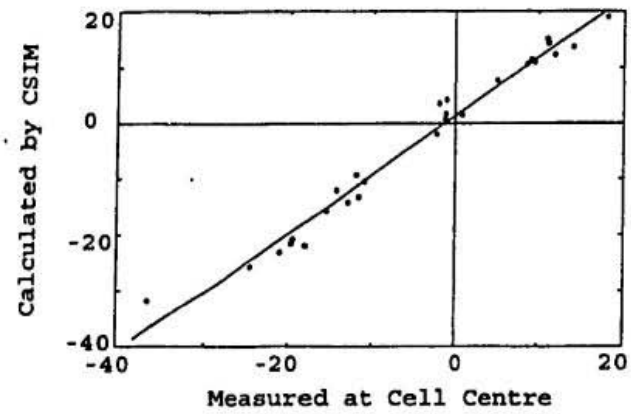

b)

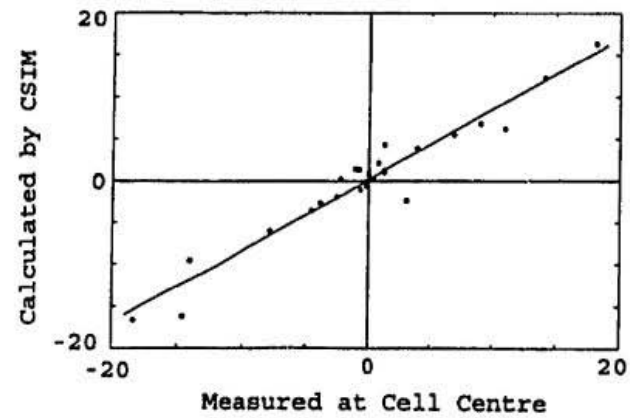

c)

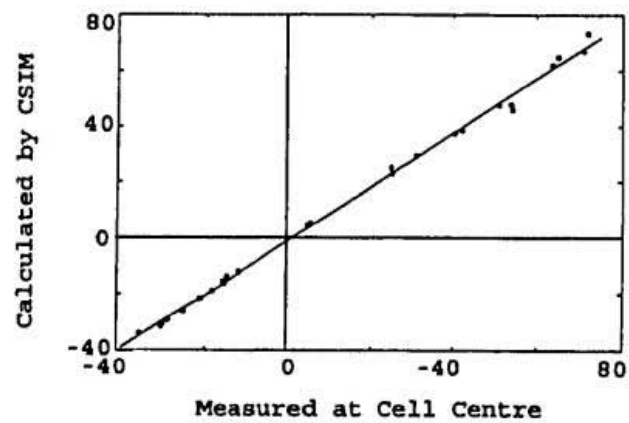

Figure 3.4: Comparison of intensity components at cell centre; calculated by CSIM versus actual measurement. a) X component; b) Y component; c) Z component.
All measurements are in units of $\mu W/m^2$.

The correlation coefficients for all three components lie within 3.5 % of unity (worst case) indicating the relationships are predominantly linear. The relationships for the x and z components both show near unity gain and a small bias. The relation for the y component shows negligible bias but a gain below unity. The clustering of much of the y component data near zero, between -5 and 5 $\mu W/m^2$ limited the usefulness of estimates with linear regression. A larger spread in magnitude, like the x or z components would have been preferable.

Nonetheless, the statistical analyses indicated the method was producing reasonably good estimates of the vector intensity distribution. Fig. 3.5 (upper graph) shows the intensity vector distribution estimated by CSIM on a linear scale. The arrows extending from each cell centre indicate the magnitude of each component. From symmetry considerations, it was expected that the intensity vector distribution should be symmetric about the centre line of the cantilever. This quality is indeed present in Fig. 3.5. The standard deviation associated with each component is similarly illustrated on the same scale (lower graph). They appear as dots indicating relatively small variations were observed during data collection.

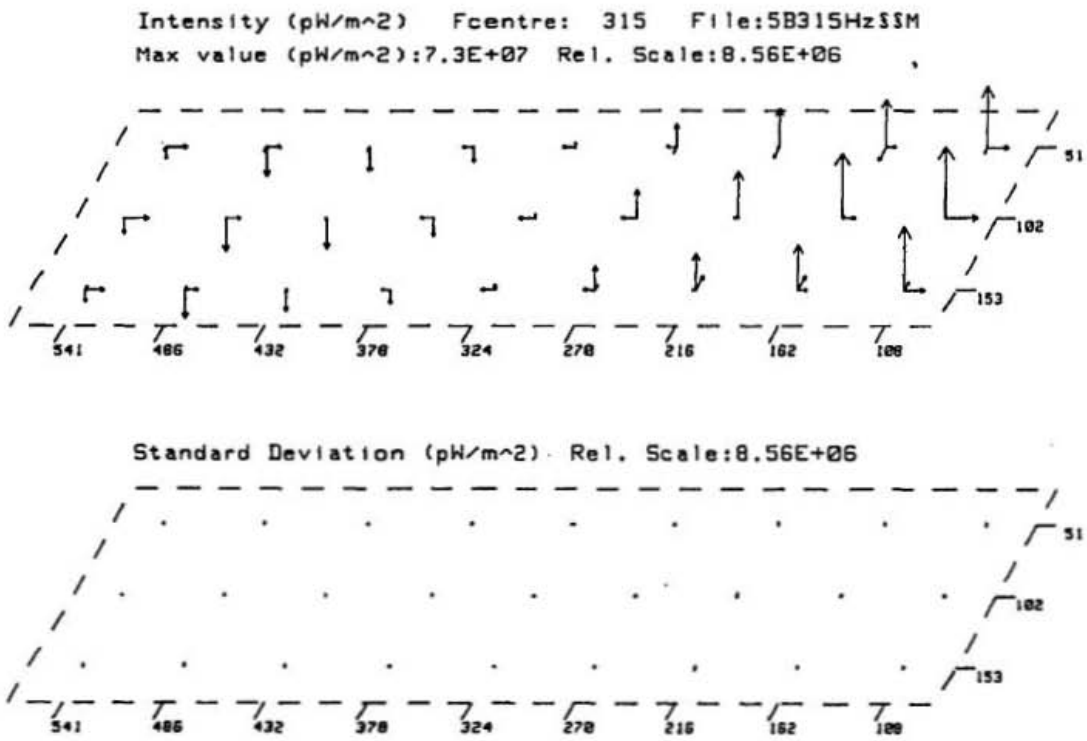

Figure 3.5: The acoustic intensity distribution calculated by CSIM (single frequency excitation, 50 mm microphone spacing). The acoustic intensity distribution (upper graph) and corresponding standard deviations (lower graph) are both presented on the same linear scale with arrow length proportional to amplitude. Coordinates are in mm.

3.5 A Numerical Measure of Reliability

A measure of reliability of the estimated vector distribution is obtained by recognizing that each cell in the box forms a closed surface. The apparent net flux out of each cell should ideally be zero but the approximations introduce errors. The sum of the apparent flux Φ_{cell} leaving the jth cell is given in Eq.(3.14).

$$(\Phi_{cell})_j = \sum_{i=1}^{6} \Psi_{ij} \cdot A_{ij} \qquad (3.14)$$

A_{ij} is the area of the ith wall of the jth cell. Ψ_{ij} is the intensity measured normal to A_{ij}.

If the approximations used by the method are good at the final cell dimensions, then the typical net flux leaving each cell should be small compared to the level of flux entering and leaving the box. This ratio, denoted α, is formalized in Eq.(3.15).

$$\alpha = \frac{\sqrt{\frac{1}{N_x N_y} \sum_{j=1}^{N_x N_y} \left[\frac{(\Phi_{cell})_j - \overline{\Phi_{cell}}}{\sum_{i=1}^{6} A_{ij}} \right]^2}}{\left[\frac{\Phi_{absolute}}{\sum_{i=1}^{N} A_i} \right]} \qquad (3.15)$$

The physical significance of α is interpreted to be the typical rms acoustic intensity from a fictitious source enclosed by a cell, normalized to the sum of absolute intensity entering or leaving the box. The fictitious source is introduced by the effect of approximations and errors in measurement, and by the assumption of stationarity which ignores net changes in the acoustic field that actually occur over the time frame for completing all the measurements.

As an indication of reliability, α should be small. Being dimensionless, it can be thought of as the percentage error in the data used to construct the intensity map. A nominal acceptance value for α would be 0.1 if discrepancies of 10% could be tolerated. Several examples follow to illustrate the use of α.

Two mappings similar to that of Fig. 3.5 were done using the same distribution of gridpoints, similar force excitation, and similar data collection parameters. Table 3.3 lists the data collection parameters for these experiments.

Table 3.3 Summary of data collection parameters

Figure #	3.5	3.6	3.7
Excitation frequency (Hz)	315.0	314.0	315.0
Microphone spacing (mm)	50	12	12
Averaging time constant (sec)	16	2	16
Length of time series (points)	10	10	10
Box height (mm)	10	10	10
Mapping plane height (mm)	65	35	35
Alpha (α)	0.040	0.055	0.147

The main difference to note for Fig.'s 3.6 and 3.7 is that the microphone pair spacing was only 12 mm for these mappings, and the height of the mapping plane was 35 mm.

Hardware phase resolution was not always adequate to resolve the phase difference

over 12 mm. When phase resolution was inadequate, measurements appeared stable for minutes, even hours and then reversed sign. The change in sign identified the problem to be related to the phase resolution. (Separate measurements showed the phase difference over 12 mm was only 0.2 degrees in a typical case.)

Fig.'s 3.6 and 3.7 illustrate the results of the two mappings with 12 mm microphone spacing. Again the errors were small relative to the magnitude of the measured components. The ratio α calculated from each case is given in Table 3.3. Fig. 3.5, with its quality established from the earlier data comparison exhibits good symmetry about the cantilever centreline and has an α of 0.040. Examination of Fig.'s 3.6 and 3.7 will show that Fig. 3.6 is more symmetric about the cantilever centre line than Fig. 3.7 (particularly in the y components). This difference in symmetry is indicated in the value of α, 0.055 for Fig. 3.6 versus 0.147 for Fig. 3.7. With a maximum acceptance value of 0.1 for α, the mappings that generated Fig.'s 3.5 and 3.6 would be accepted but not the mapping that generated Fig. 3.7.

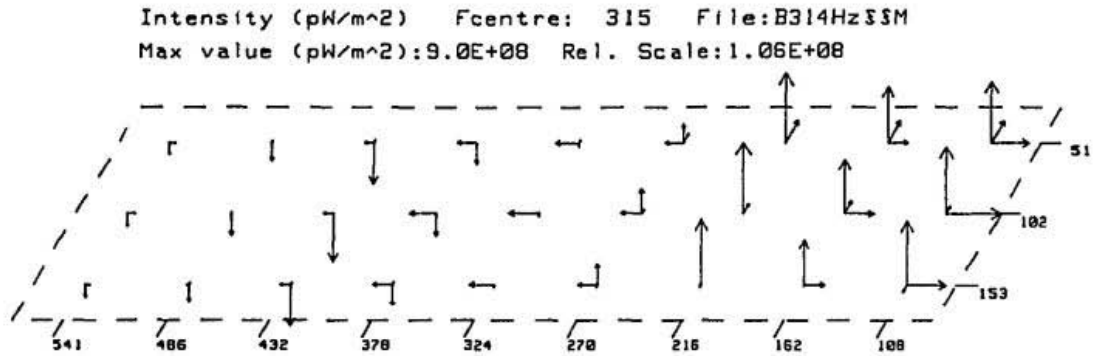

Figure 3.6: An acoustic intensity distribution calculated by CSIM (single frequency excitation, 12mm microphone spacing).

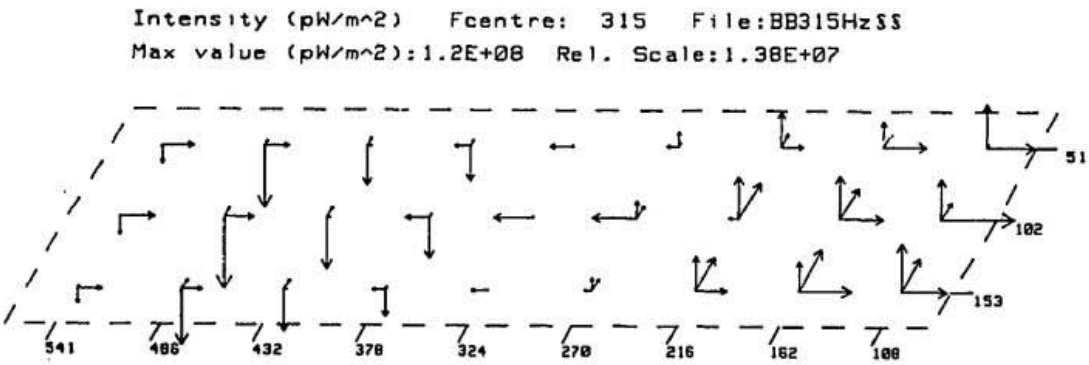

Figure 3.7: A second acoustic intensity distribution calculated by CSIM (single frequency excitation, 12 mm microphone spacing).

Intensity mappings (Fig.'s 3.8 and 3.9) in the 125 Hz frequency band were made for two similar size cantilever specimens. A smooth cantilever provided the data for all figures but Fig. 3.8. A cantilever with a fine notch across its width was used for Fig. 3.8. The effect of the notch was minor, shifting the natural frequencies by less than 2%. The data collection parameters were the same for both mappings and are listed in Table 3.4. These mappings used a coarser grid of points (N_x=5) and involved smaller intensity magnitudes (typically by an order of magnitude) than the previous examples. Like the mappings of the 315 Hz band with 12 mm microphone spacing, phase resolution was sometimes marginal in the 125 Hz band using a 50 mm microphone spacing.

Table 3.4 Summary of data collection parameters

Excitation frequency (Hz)	60 to 720 to 60 continuous
Microphone spacing (mm)	50
Averaging time constant (sec)	32
Length of time series (points)	20
Box height (mm)	10

The relative size of the standard errors (not shown) was small (typically less than 5%) for both Fig.'s 3.8 and 3.9.

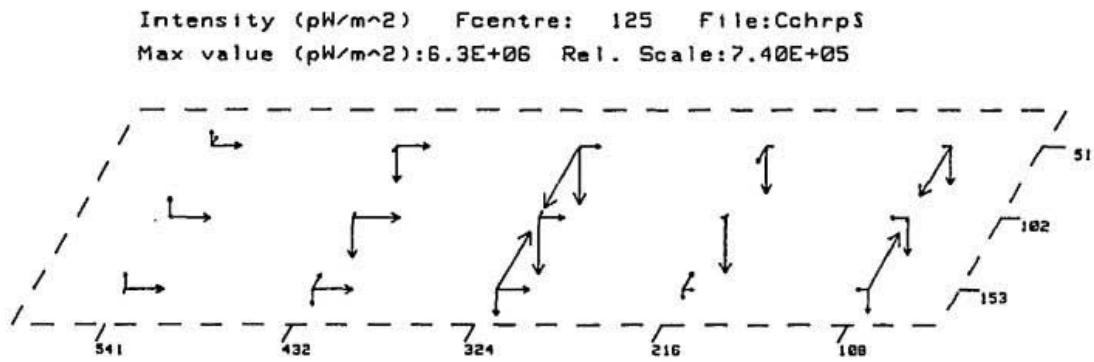

Figure 3.8: An acoustic intensity distribution calculated by CSIM (multiple frequency excitation, 50 mm microphone spacing).

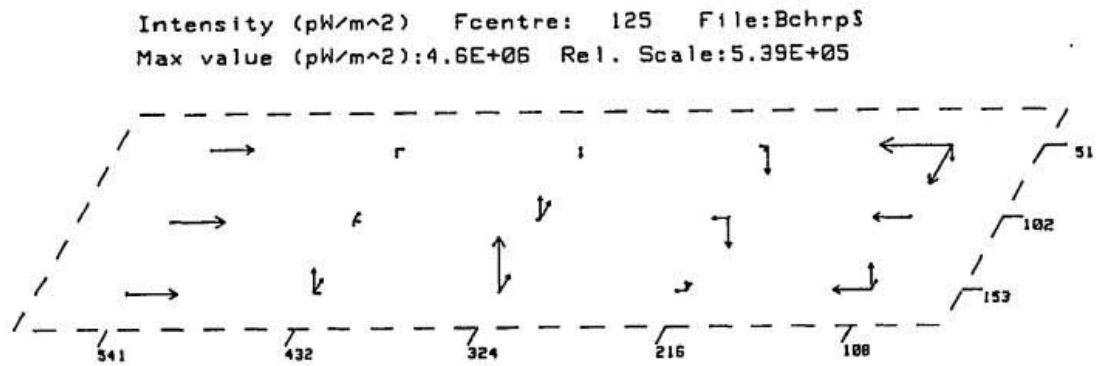

Figure 3.9: An acoustic intensity distribution calculated by CSIM (multiple frequency excitation, 50 mm microphone spacing).

Table 3.5 lists the different fluxes calculated during the mappings for Fig.'s 3.8 and 3.9.

Table 3.5 Values of the different fluxes calculated during the mappings

Fig #	Band Hz	Grid N_x	Grid N_y	$\Sigma(\Psi_{\perp surface})_i A_i$ μW	$\Sigma(\sigma_i A_i)$ μW	$\Sigma\lvert(\Psi_{\perp surface})_i A_i\rvert$ μW
3.8	125	3	3	-0.004	0.028	0.432
		5	3	-0.016	0.022	0.399
3.9	125	3	3	-0.049	0.015	0.156
		5	3	-0.019	0.014	0.149
3.10	250	3	3	0.001	0.001	0.013
		5	3	0.001	0.001	0.015

For Fig. 3.8, $|\Sigma (\Psi_{\perp surface})_i A_i| < \Sigma (\sigma_i A_i) << \Sigma |(\Psi_{\perp surface})_i A_i|$ and α was calculated to be 0.099. The mapping of Fig. 3.8 is mostly symmetric about the cantilever centre line. The symmetry of Fig. 3.8 is reflected in an α value at the limit of acceptability. By comparison Figure 3.9 is far from symmetric. For Fig. 3.9, $|\Sigma (\Psi_{\perp surface})_i A_i| \not< \Sigma (\sigma_i A_i) << \Sigma |(\Psi_{\perp surface})_i A_i|$ and α was calculated to be 0.240, well outside the limit of acceptability.

Lastly, Fig. 3.10 illustrates the intensity in the 250 Hz band collected simultaneously with that of Fig. 3.9. The intensity magnitudes in this mapping may be an order of magnitude smaller than in the 125 Hz mapping but this mapping is reasonably symmetric (one lack of symmetry in the y component at (108,153)). For this mapping, from Table 3.5, $|\Sigma (\Psi_{\perp surface})_i A_i| = \Sigma (\sigma_i A_i) << \Sigma |(\Psi_{\perp surface})_i A_i|$ and α was calculated to be 0.056, inside the limit of acceptability. These examples suggest that the value of α is insensitive to the scale of component magnitudes in a mapping and is capable of

discriminating between good and poor intensity mappings.

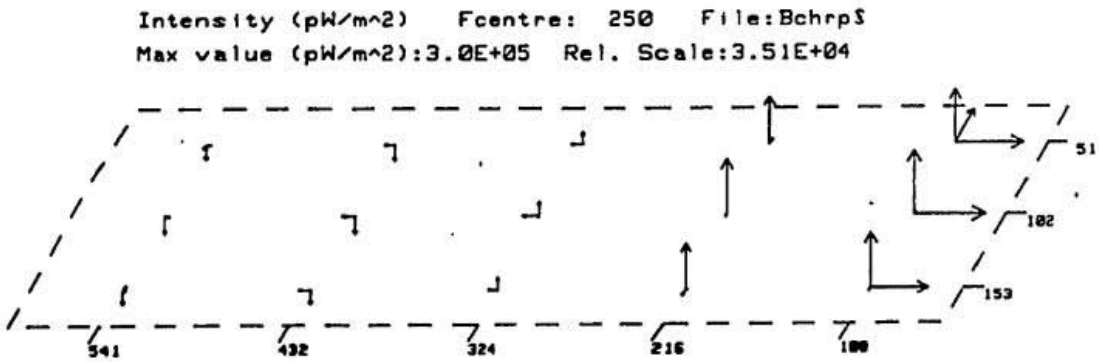

Figure 3.10: An acoustic intensity distribution calculated by CSIM (multiple frequency excitation, 50 mm microphone spacing).

One additional comment is required to complete the discussion of the CSIM mapping procedure. It may not have been immediately apparent during the discussion of intensity mappings with a 50 mm microphone spacing, that the 10 mm depth of the imaginary box was small relative to the microphone spacing. A small box depth was a compromise to place the mapping plane as close to the beam's surface as possible. A vertical cell height much less than the microphone spacing made the tacit assumption that the z intensity component varied almost linearly in the z direction over the height of a cell, which seems to have been borne out experimentally. It also introduced more relative uncertainty in the spatial positions of the top and bottom cell walls for the mappings with a 50 mm microphone spacing than for the mappings with the smaller 12 mm microphone spacing.

3.6 Averaging Time

To determine the averaging time to use in practice, the microphone pair was placed at a point in the mapping plane oriented to measure intensity normal to the vibrating surface. Using a small time constant value, between 10 and 20 samples of time averaged intensity (spaced one averaging time constant apart) were collected for each frequency band of interest. The mean and standard deviations were calculated, the time constant value doubled and data collection repeated. It was expected that a mappable frequency band would exhibit a mean value that stabilized with increasing time constant and a standard deviation that decreased with increasing time constant. A mean to standard deviation ratio greater than 10 was taken to indicate that an adequate minimum value for the averaging time constant had been reached. This process was then repeated at two other points in the plane. With the number of samples in the timeseries and the averaging time constant established, the described mapping methodology could then be carried out.

Table 3.6 Observed intensity statistics versus measurement interval

Total Interval (sec)	Time Constant (sec)	Position 1 $\mu W/m^2$		Position 2 $\mu W/m^2$		Position 3 $\mu W/m^2$	
		Mean	Std Dev	Mean	Std Dev	Mean	Std Dev
80	4	-3.39	0.80	-4.40	0.65	0.308	0.073
160	8	-3.36	0.56	-4.49	0.21	0.355	0.052
320	16	-3.13	0.38	-4.49	0.28	0.340	0.033
640	32	-3.49	0.27	-4.40	0.18	0.333	0.015

Table 3.6 shows the observed statistics that determined the measurement time interval for the mapping shown in Fig. 3.8. The time series consisted of 20 samples of exponentially averaged intensity using a 4, 8, 16 or 32 second time constant. In this case the mean value at each position was consistent with an 8 second time constant, but a 32 second time constant was required to achieve a mean to standard deviation ratio greater than 10 in all 3 positions.

3.7 Summary

The method presented in this chapter was developed as a recipe for mapping the spatial distribution of time averaged acoustic intensity. It used the physics of a closed surface to assess the accuracy of the experimental data by examining how well the data satisfied Gauss's law. The method was designed to indicate when sufficient measurements have been collected, ensure that the surface areas associated with each intensity measurement were well defined, and provide a quantitative means of assessing whether the calculated spatial distribution of intensity was an accurate representation of the acoustic field. It was applied to the near field of a cantilever beam and experimentally validated. Several examples demonstrated an ability to accept good intensity mappings and reject poor ones.

CHAPTER FOUR

ACOUSTIC INTENSITY FROM PRESSURE TRANSFER FUNCTIONS

During the program to develop acoustic methods to monitor the mechanical behaviour of structures, measurements of acoustic pressure were effectively being duplicated, perhaps unnecessarily. Two microphones and a sound intensity analyzer were used to map the spatial distribution of intensity in 1/3 octave bands above a cantilever beam. Then with a dual channel signal analyzer, one of the microphones and a force transducer (measuring excitation to the beam) were used to construct PTF's (pressure transfer functions) for estimating the beam's modal parameters. On paper it seemed possible to construct acoustic intensity from the same PTF's used for modal parameter estimates (see section 4.1) and eliminate the need for separate sound intensity measurements. An experiment was devised to compare acoustic intensity measured with the sound intensity analyzer and that calculated with PTF's (section 4.2). The experimental testing identified limitations associated with frequency resolution (section 4.3) and phase resolution (section 4.4). After the recipe for acoustic intensity from PTF's was established, it became apparent that the intensity calculated from PTF's and that measured with the sound intensity analyzer emphasized different regions of the frequency spectrum (section 4.5).

4.1 Relating Acoustic Intensity To Pressure Transfer Functions

It was shown in chapter 2 that the spectral contribution to time averaged acoustic intensity at angular frequency ω_m was,

$$\overline{\Psi(m)} \doteq \frac{-1}{\omega_m \rho_o d} Im\left[X_A(m)\, X_B^*(m) \right] \qquad (4.1)$$

where $X_A(m)$ is the mth spectral coefficient of a DFT of $p_A(t)$ corresponding to frequency ω_m. If both sides of our expression are divided by some real number, say R, then,

$$\frac{\overline{\Psi(m)}}{R} \doteq \frac{-1}{\omega_m \rho_o d} Im\left[\frac{X_A(m)\, X_B^*(m)}{R} \right] \qquad (4.2)$$

It will be assumed that there is one point force f(t), which causes a mechanical system to radiate the acoustic field p(t). We choose $R = |F(m)|^2$, where F(m) is the mth spectral coefficient of the DFT of f(t). Then we have,

$$\frac{\overline{\Psi(m)}}{|F(m)|^2} \doteq \frac{-1}{\omega_m \rho_o d} Im\left[\frac{X_A(m)\, X_B^*(m)}{|F(m)|^2} \right] \qquad (4.3)$$

Using $|F(m)|^2 = F^*(m) \cdot F(m)$, we can write,

$$\frac{\overline{\Psi(m)}}{|F(m)|^2} \doteq \frac{-1}{\omega_m \rho_o d} Im\left[\frac{X_A(m)}{F(m)} \left[\frac{X_B(m)}{F(m)} \right]^* \right] \qquad (4.4)$$

We recognize $X_A(m)/F(m)$, $X_B(m)/F(m)$ as the transfer functions between acoustic pressure and the applied force, corresponding to points A and B respectively.

Eq.(4.4) assumes a causal relation between force and pressure. It may happen in practice that the sound field is composed of two pressure fields, one the result of force applied to a mechanical system, the other a result of some unrelated process. We can coherently average with respect to the applied force to minimize the contribution to the transfer function by the extraneous sound component using one of the standard processing

functions available on a dual channel signal analyzer,

$$\left\langle \frac{X(m)}{F(m)} \right\rangle = \frac{\sum_{i=1}^{N} F_i^*(m)\, X_i(m)}{\sum_{i=1}^{N} F_i^*(m)\, F_i(m)} = \frac{\sum_{i=1}^{N} (G_{f,p}(\omega_m))_i}{\sum_{i=1}^{N} (G_{f,f}(\omega_m))_i} \qquad (4.5)$$

which is the average of N cross spectra between force and pressure, $G_{f,p}(\omega_m)$, divided by the average of N autospectra of force $G_{f,f}(\omega_m)$. Then we have,

$$\frac{\overline{\Psi(m)}}{|F(m)|^2} \doteq \frac{-1}{\omega_m \rho_o d} Im \left[\frac{\sum_{i=1}^{N} (G_{f,p_s}(\omega_m))_i}{\sum_{i=1}^{N} (G_{f,f}(\omega_m))_i} \frac{\sum_{i=1}^{N} (G^*_{f,p_s}(\omega_m))_i}{\sum_{i=1}^{N} (G_{f,f}(\omega_m))_i} \right] \qquad (4.6)$$

Eq.(4.6) assumes $\Psi(m)$ represents the component of intensity caused by f(t). It will be assumed that the mechanical system and surrounding acoustic environment do not change. Then the pressure transfer function estimates should be time invariant and $\Psi(m)/|F(m)|^2$ should have some characteristic value at each ω_m.

4.2 Experimental Comparison With Measured Intensity

Acoustic intensity measured directly with a microphone pair was compared with acoustic intensity reconstructed from PTF's and the applied force spectrum. The smooth cantilever beam described in chapter 3 was driven by a point force to generate the sound field. The surroundings were fixed, keeping the acoustic environment static. It was therefore assumed that the PTF's were time independent.

The comparison was facilitated by multiplying equation (4.6) by $|F(m)|^2$ to obtain,

$$\overline{\Psi(m)} \doteq \frac{-|F(m)|^2}{\omega_m \rho_o d} Im \left[\frac{\sum_{i=1}^{N} (G_{f,p_A}(\omega_m))_i \sum_{i=1}^{N} (G^*_{f,p_B}(\omega_m))_i}{\sum_{i=1}^{N} (G_{f,f}(\omega_m))_i \sum_{i=1}^{N} (G_{f,f}(\omega_m))_i} \right] \qquad (4.7)$$

The left hand side is the net acoustic intensity at frequency ω_m measured with $p_A(t)$ and $p_B(t)$. The right hand side is the spectral product at frequency ω_m of, the PTF between force and $p_A(t)$, the PTF between force and $p_B(t)$, and the squared magnitude of force. Clearly $\Psi(m)$ and F(m) must be measured over the same interval [0,T].

The experimental setup is shown in Fig. 4.1. A microphone pair was suspended above the cantilever. The microphone signals were available to a Bruel and Kjaer 3360 Sound Intensity Analyzer and to a Bruel and Kjaer 2032 Dual Channel Signal Analyzer. The force signal was fed to the Dual Channel Signal Analyzer. With this setup the transfer functions between pressure and force were measured by the Dual Channel Signal Analyzer. Then at some later time, acoustic intensity was time averaged by the Sound Intensity Analyzer while the spectrum of applied force was collected by one channel of the Dual Channel Signal Analyzer. For this latter measurement, both systems were manually triggered to record over the same time interval. A comparison was then made between the intensity measured by the sound intensity analyzer and that calculated with equation (4.7) using the measured PTF's, and the measured force spectrum.

4.3 Frequency Resolution Considerations

Early tests measured PTF's with 2 Hz frequency resolution over a frequency interval that included the fourth beam bending mode at 801 Hz.

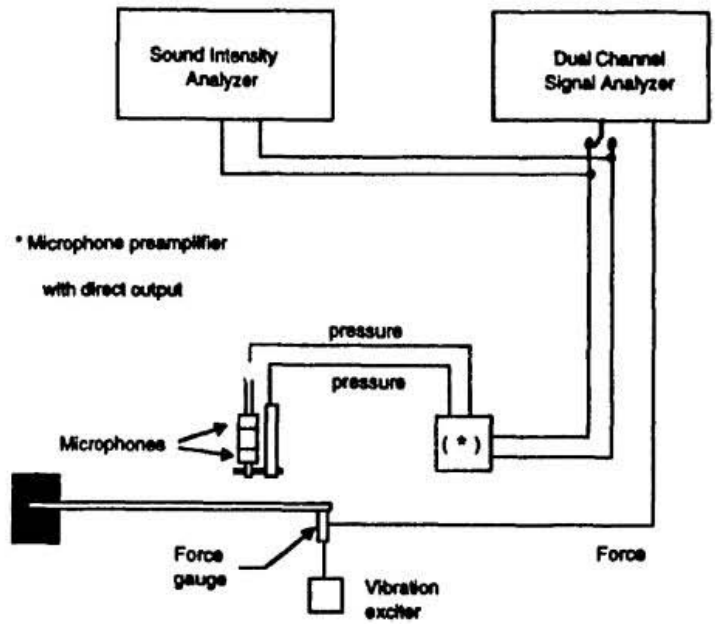

Figure 4.1: Experimental setup for measuring pressure transfer functions and radiated acoustic intensity.

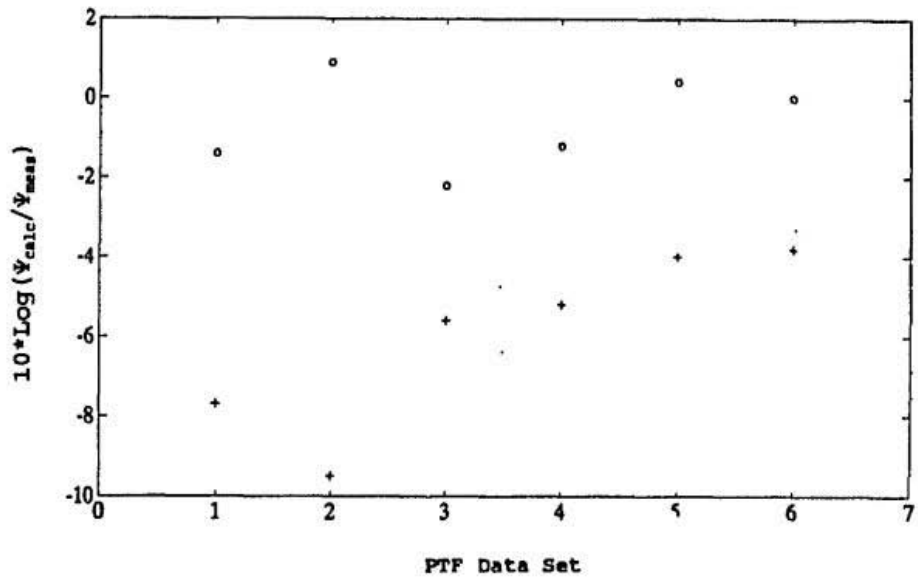

Figure 4.2: Comparison of calculated and measured intensity near (+) and off (o) resonance.

Then single frequency excitation was used to excite the beam near the fourth mode for simultaneous measurements of time averaged acoustic intensity and the spectrum of applied force.

Six separate PTF data sets had been collected for the same location and intensity direction. Intensity and force measurements occurred twice, once with excitation at 796 Hz (off resonance) and once at 800 Hz (near resonance). The ratio in dB ($10 \cdot \mathrm{Log}(\Psi_{calc}/\Psi_{meas})$) is plotted in Fig. 4.2 for each PTF data set and both excitation frequencies. Fig. 4.2 shows that Ψ_{calc} underestimated Ψ_{meas} by 4 to 10 dB near resonance but estimated Ψ_{meas} within 2 dB off resonance.

Simultaneous measurements were continued (single frequency excitation) to compare calculated and measured intensity with proximity to the fourth mode natural frequency. The same ratio ($10 \cdot \mathrm{Log}(\Psi_{calc}/\Psi_{meas})$) is plotted in Fig. 4.3 to show the variation with frequency between directly measured intensity and that reconstructed from the instantaneous force spectra and the PTF's (still 2 Hz frequency resolution). Fig. 4.3 also shows the force level as a function of frequency. The amount of disagreement seemed correlated to the separation between the excitation frequency and resonance (801 Hertz) and possibly the force level. A small experiment conducted at fixed excitation frequency (810 Hz) examined the effect of force level. The ratio in dB ($10 \cdot \mathrm{Log}(\Psi_{calc}/\Psi_{meas})$) is plotted in Fig. 4.4 versus the force level in dB ($10 \cdot \mathrm{Log}(\mathrm{Force}/1\mathrm{N})$). The results suggested force level wasn't a major contributor to the previous descrepancy. Attention was therefore directed to the effects of frequency resolution.

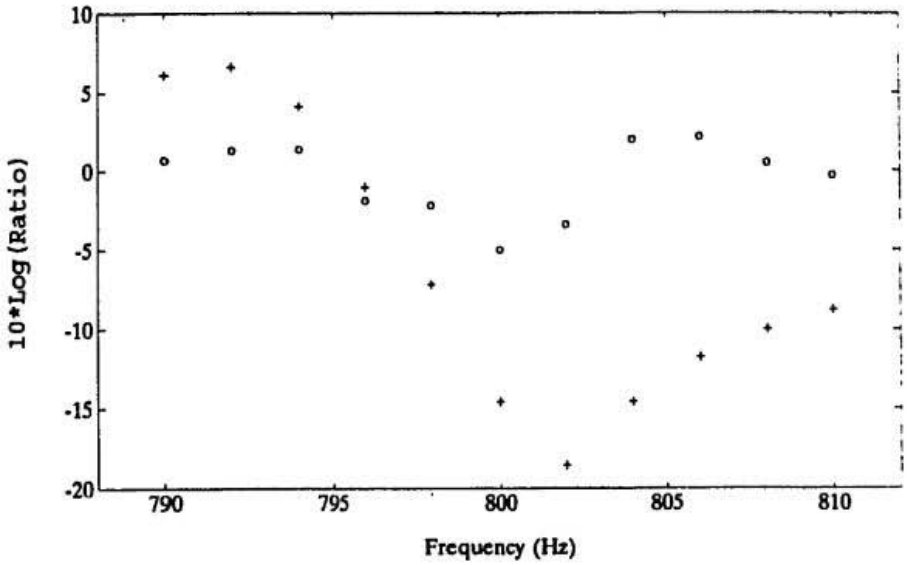

Figure 4.3: Variation with proximity to natural frequency. (o) Ratio = Ψ_{calc}/Ψ_{meas}; (+) Ratio = Force/1N.

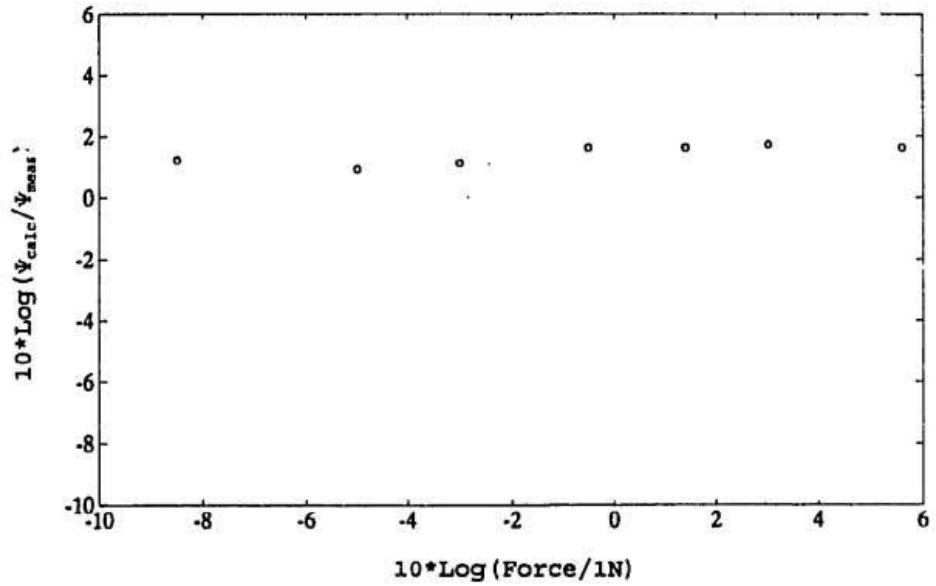

Figure 4.4: Ratio of calculated to measured acoustic intensity versus force level.

In the development of the cross spectral formulation for intensity (chapter 2) the continuous Fourier spectrum was approximated by a discrete Fourier series. In a natural frequency region, the frequency resolution of the discrete series needs to be small enough to replicate the rapid amplitude change with frequency of the continous spectrum. The data in Fig. 4.3 suggested an examination of the ability of the 2 Hz frequency resolution PTF to replicate spectrum shape near resonance.

New PTF's were collected (same location) with 0.25 Hz frequency resolution. Fig. 4.5 compares magnitudes at common frequencies for 2 Hz and 0.25 Hz resolution PTF's. While the spectral coefficients at the two resolutions were similar to either side of resonance, between 798 and 802 Hz the coarser 2 Hz resolution spectrum had smoothed out the peak. This result suggested that insufficient PTF frequency resolution prevented proper replication in the natural frequency region causing measured and calculated intensities to differ.

4.4 Phase Resolution Considerations

To further improve PTF frequency resolution, PTF's were collected at 0.125 Hz resolution (in addition to the 0.25 Hz PTF's). The comparison of calculated and measured intensity was repeated. Table 4.1 lists the results.

The acoustic intensity constructed from PTF's with 0.25 Hz resolution showed improved agreement with measured intensity, but not that constructed using 0.125 Hz resolution PTFs. Finer frequency resolution had only mitigated the amount of disagreement some of the time.

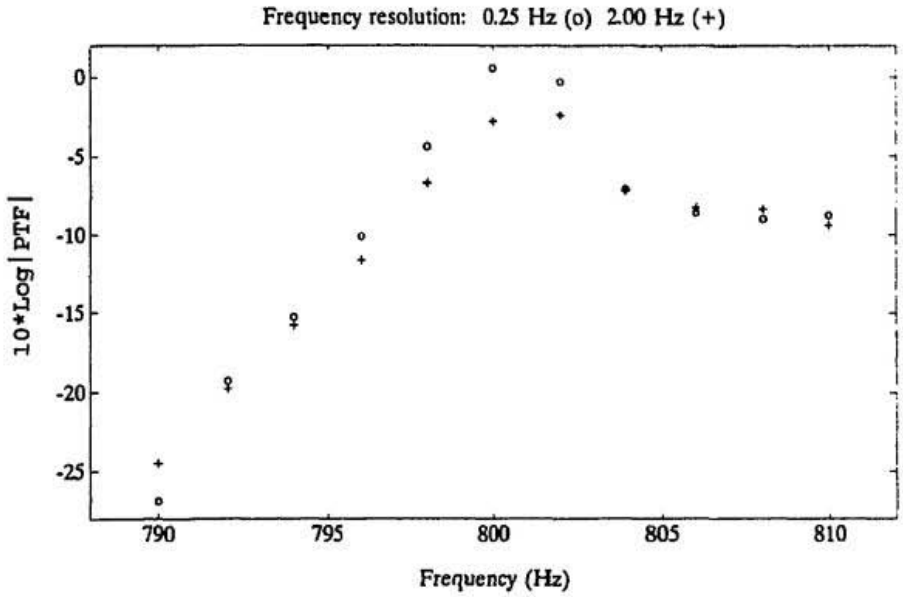

Figure 4.5: Effect of frequency resolution on pressure transfer function amplitude near resonance. (o) 0.25 Hz; (+) 2 Hz.

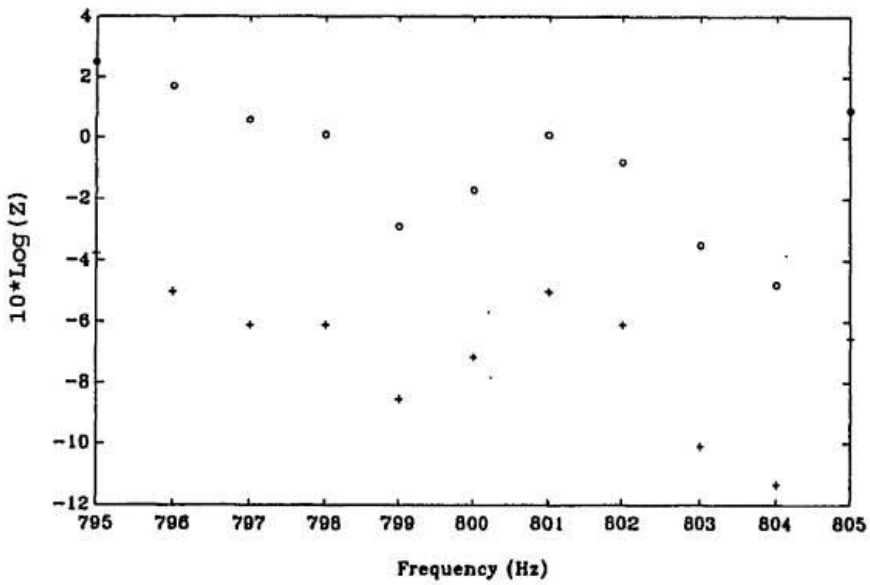

Figure 4.6: The correlation of phase difference with the ratio between calculated and measured acoustic intensity. (o) $Z = \Psi_{calc}/\Psi_{meas}$; (+) Z = sin(phase difference).

Table 4.1 Acoustic intensity constructed from pressure transfer functions with finer frequency resolution

Freq Hz	$10*Log_{10}(\Psi_{calc}/\Psi_{meas})$ Δf=0.25 Hz	Δf=0.125 Hz
796	1.7	1.4
798	0.2	-2.0
800	-0.3	-2.0
802	0.4	0.5
804	-0.6	-4.9

It was then noted that the amount of error correlated with the phase difference between PTF's. Fig. 4.6 illustrates the correlation of $10 \cdot Log(\Psi_{calc}/\Psi_{meas})$ with the sine of the phase difference between PTF's for yet another set of 0.125 Hz resolution PTF's.

It was unknown whether potential differences between the two hardware systems could produce an error correlated with phase. Therefore a comparison was made between cross spectral acoustic intensity measured with the Dual Channel Signal Analyzer and acoustic intensity measured with the Sound Intensity Analyzer. Both systems were connected to the same microphone pair and calibrated. Both systems were triggered manually to measure intensity over the same 8 second time interval to within approximately a third of a second. The cantilever was excited for most measurements at a single frequency. For one comparison a broad band excitation was used. The results are given in Table 4.2. The agreement removed any doubts about differences between hardware, showing the two measurement methods to be equivalent. The data also provided insight into the source of the error.

Table 4.2 Comparison of acoustic intensity measurement methods

Freq. (Hz)	10 Log($\Psi_{\text{Signal Analyzer}}$/(pW/m^2))	10 Log($\Psi_{\text{Intensity Analyzer}}$/(pW/m^2))
795.	77.6	77.6
796.	76.8	77.0
797.	75.9	76.1
798.	74.2	74.4
799.	73.5	73.7
800.	73.6	73.7
801.	72.2	72.3
802.	70.7	71.0
803.	68.6	68.7
804.	67.9	68.1
805.	68.4	68.5
780-820$^{(\text{sweep})}$	72.4	72.3

The phase difference between microphones taken from the cross spectrum of the dual signal channel analyzer varied smoothly with frequency across the region of natural frequency whereas the phase difference calculated from PTF's did not. The two sets of phase difference should have been in agreement. Since the acoustic pressures would reach their peak values near resonance, the lack of agreement suggested the force signal during PTF measurements was too small in the region of natural frequency to reliably establish the force-pressure phase difference.

To examine the influence of force level, PTF's were collected at 0.125 Hz resolution with a similar force level to that previously used. Then the measurement was repeated with an approximately 15 dB larger force level. Lastly, the cross spectrum of the pressures was measured at several frequencies under single frequency excitation to provide an estimate of the true phase difference. The phase differences from both sets of PTF's

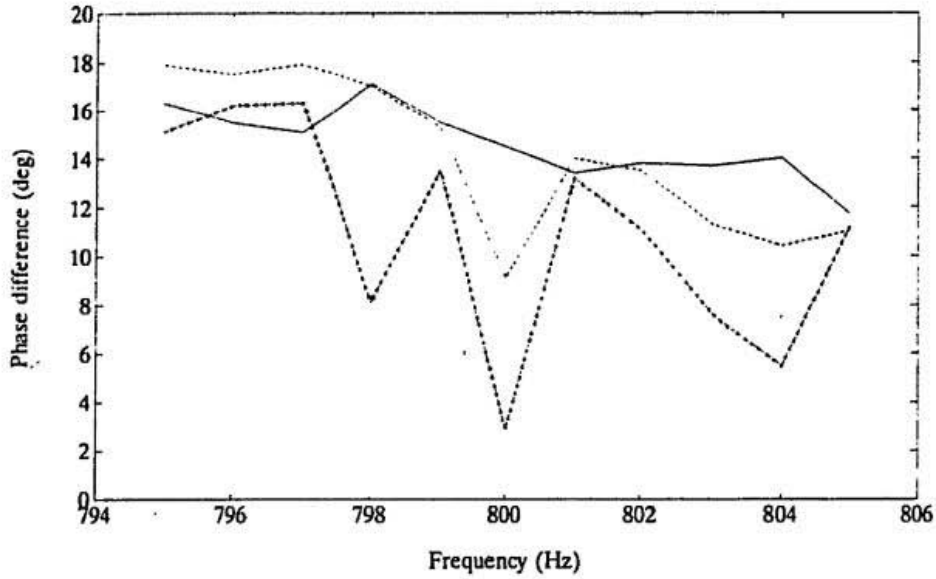

Figure 4.7: Phase difference; cross spectrum versus pressure transfer functions. (solid) cross spectrum; (dash-dot) low force PTF's; (dashed) raised force PTF's.

and the pressure cross spectrum are plotted versus frequency in Fig. 4.7. At 798,800, 803 and 804 Hz, the PTF's collected with the lower force level showed smaller phase differences than the pressure cross spectrum, by at least 50 %. The phase difference from the PTF's collected at the raised force level agreed reasonably well with that of the pressure cross spectrum everywhere except at 800 Hz. It was concluded that the previous lack of agreement was a result of insufficient force signal during PTF measurements. The remedy was simply to raise the force level to obtain a better estimate of phase difference. The comparison of measured and calculated intensity was repeated. PTF's were collected at the higher force level. As before, the instantaneous force spectrum was collected during the intensity measurement. In most cases a continous sine sweep was used to generate a

force signal with frequency content spanning the 1/3 octave band of interest of the Sound Intensity Analyzer. Measurements of the PTF's and acoustic intensity were made in the 800 Hz band at two positions above the cantilever beam. Additional measurements of the PTF's and acoustic intensity were made in the 315 Hz band at one position above the cantilever beam. The 315 Hz band encompassed the third beam bending mode natural frequency. Table 4.3 tabulates the results of the comparison. The agreement between calculated and measured intensity was now satisfactory, typically within 0.5 dB (12 %). This agreement occurred with some PTF's that had been measured 3 to 6 days before the intensity and force spectra were measured.

Table 4.3 Acoustic intensity calculated from pressure transfer functions versus measurement

Freq. Range	10 Log(Ψ_{calc}/(pW/m^2))	10 Log(Ψ_{meas}/(pW/m^2))
780-820 @ 0.33 Hz	72.3	72.6
780-820 @ 1 Hz	73.2	73.1
770-840 @ 1 Hz	70.6	70.4
780-820 @ 0.5 Hz	72.5	72.1
780-820 @ 0.5 Hz	79.7	80.0
770-830 @ 0.7 Hz	78.4	79.0
805 Hz	74.2	74.9
375-425 @ 0.8 Hz	65.3	65.9
375-425 @ 0.5 Hz	64.6	64.9

4.5 The Normalization of Acoustic Intensity From Pressure Transfer Functions

In Eq.(4.6), the spectral intensity is normalized to the square magnitude of applied force. This normalization emphasizes the natural frequency region, where a little force can

generate substantial acoustic energy. This emphasis is illustrated in Fig. 4.8 which shows a 30 Hz wide window of mean acoustic intensity (solid line) calculated from PTF's measured above another cantilever beam. The calculated intensity reaches a maxima at the cantilever's 5th beam bending mode located at 1323 Hz.

The dotted curves plot the upper and lower error bounds on the mean value. The PTF spectra were collected as a time series to obtain the statistics of the real and imaginary parts of each PTF as a function of frequency. The bounds were calculated by considering the possible permutations introduced by changing the real or imaginary parts of the PTF's by their corresponding standard deviation.

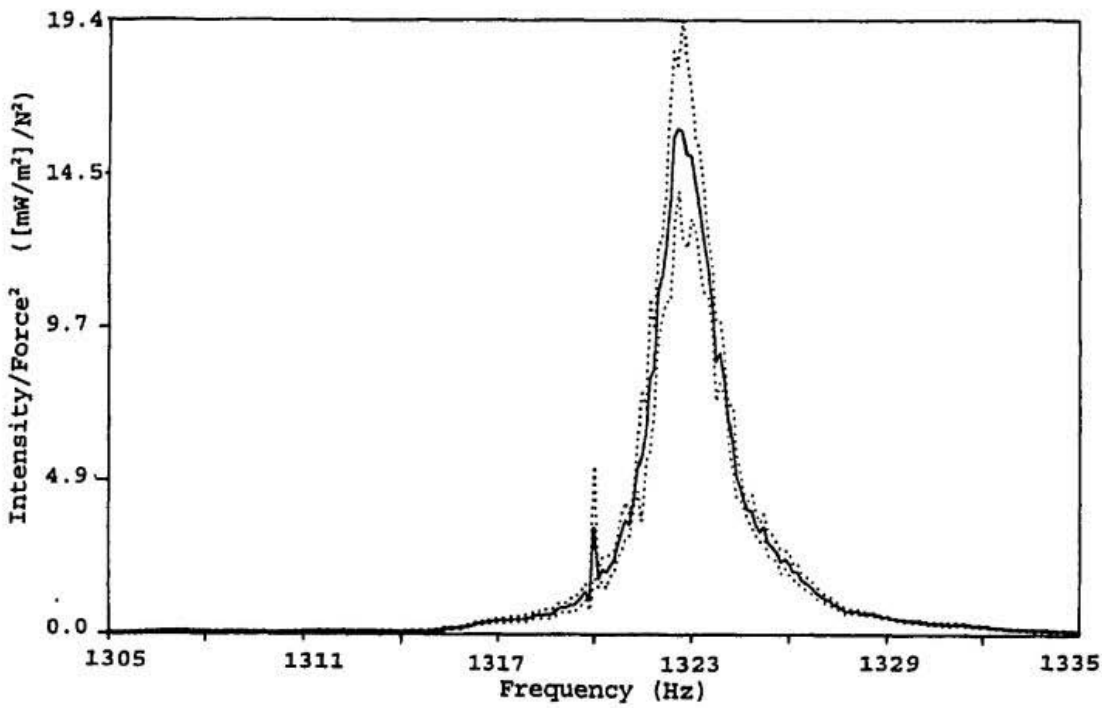

Figure 4.8: Acoustic intensity constructed from pressure transfer functions in the region of the fifth bending mode.

One aspect that was not fully appreciated at the onset of tests, was the different emphasis with frequency, between acoustic intensity from PTF's versus acoustic intensity measured directly using random noise excitation with a flat amplitude spectrum. In the first case, the use of PTF's produced an intensity calculated for a flat force spectrum of unit amplitude. In the second case the signal to the amplifier driving the exciter had equal spectral energy at all frequencies and the hardware was expected to generate an approximately flat force spectrum.

Fig. 4.9 shows the intensity measured directly using a Dual Channel Signal Analyzer with the same microphone positions as Fig. 4.8 and a flat random noise spectrum to the exciter amplifier. The spectrum in Fig. 4.9 peaked at 1305 Hz, 18 Hz below the natural frequency and the spectral peak in Fig. 4.8.

Acoustic intensity from PTFs peaks at the natural frequency because the PTF's peak at the natural frequency. Any hardware limitations in applying a uniform force have been eliminated by the normalization. Fig. 4.10 shows the amplitude of one of the PTFs collected above the beam peaking at the 5th mode natural frequency, 1323 Hz.

Without the normalization, the applied force spectrum was sufficiently uneven (even with a flat noise spectrum to the exciter amplifier) to shift the region of maximum intensity measured directly, away from the natural frequency. Figure 4.11 shows the applied force spectrum on both linear and logarithmic scales. The force spectrum had a maxima at 1300 Hz and a minima at 1323 Hz. (This force spectrum shape was typical for other natural frequency regions too.)

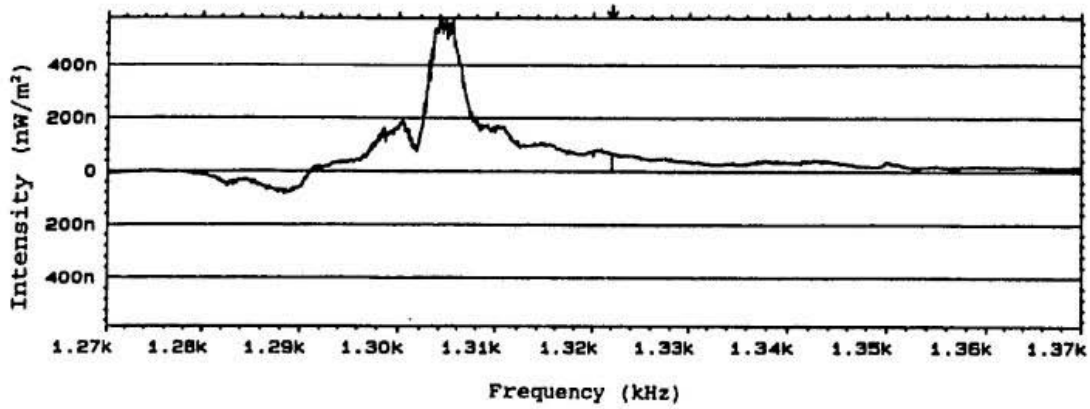

Figure 4.9: Acoustic intensity from pressure cross spectrum in the region of the fifth bending mode. In units of nW/m^2.

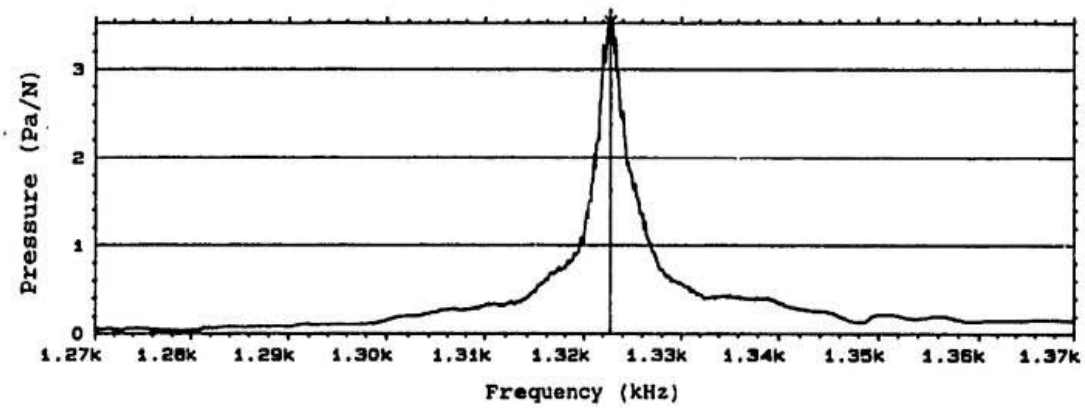

Figure 4.10: Pressure transfer function in the region of the fifth bending mode. In units of Pa/N.

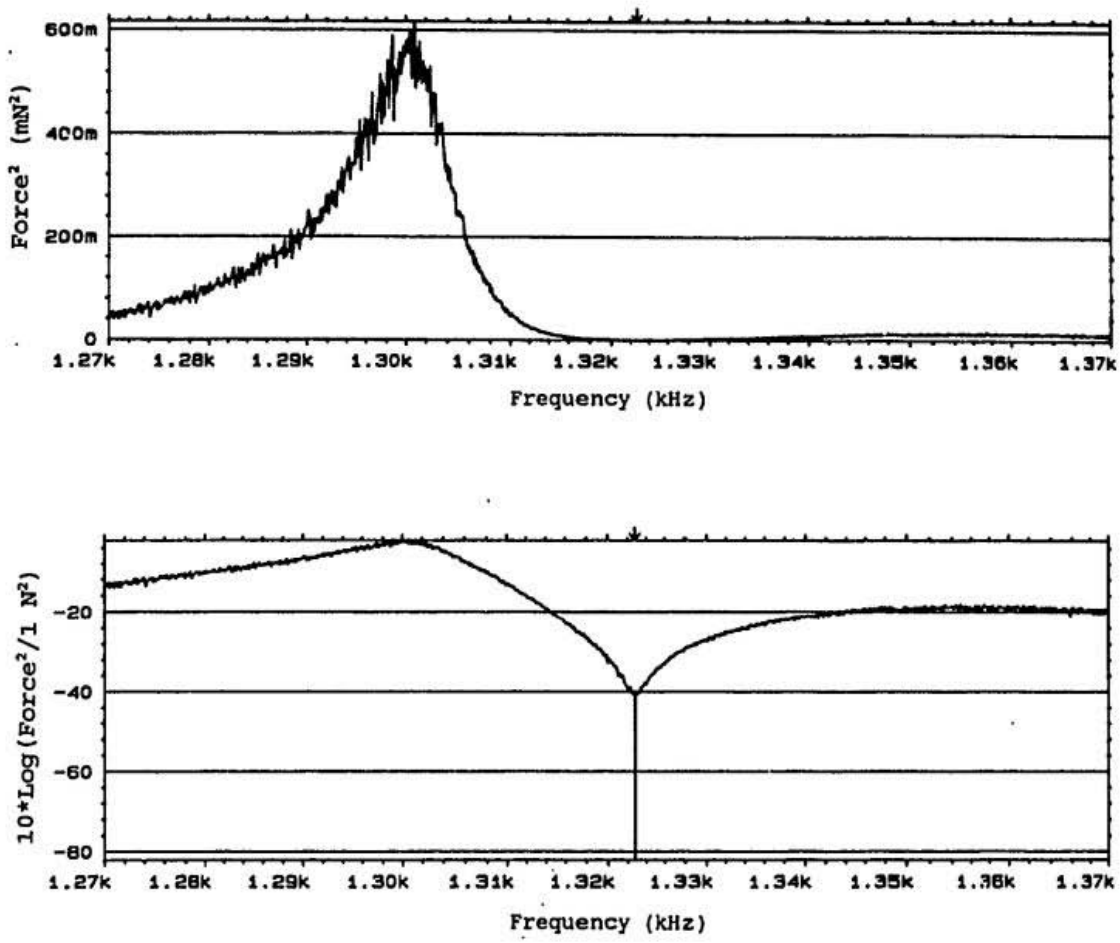

Figure 4.11: Force power spectrum in the region of the fifth bending on a linear (upper graph) and logarithmic (lower graph) scale. In units of mN^2 and dB re 1 N^2.

The cantilever was a very lightly damped system. Approaching resonance frequency the beam's apparent stiffness decreased rapidly reaching a minima at resonance. Beyond resonance the stiffness recovered with frequency. The exciter amplifier and

mechanical exciter were supposed to generate an approximately flat force spectrum, but apparently could not adjust to the varied stiffness around the resonance region. Physically, near resonance, the beam would yield without substantial resistance. The exciter could not generate much force by pushing something that yielded almost completely without pushing back. Consequently the region of maximum intensity occurred where the product of the force and PTF spectra peaked, at a frequency below the beam's natural frequency.

4.6 Summary

Overall, the construction of acoustic intensity from PTF's was successful. The PTF's had to be measured with a frequency resolution fine enough to provide a good estimate of the true spectral shape in the natural frequency regions. Equally important, the phase of the PTF's had to be accurate. At the natural frequencies, although the pressure signal levels might be adequate, the force signal could be small. This resulted in poor estimates of the phase difference between pressure and force. The cure was simply to raise the force level.

Acoustic intensity constructed from PTF's was normalized with respect to applied force. This normalization emphasized the natural frequency regions where a little force generated substantial power. Without this normalization, measured acoustic intensity became the product of both the mechanical response of the system and the shape of the force spectrum. In the case of the cantilever beam, mechanical limitations produced uneven force spectra causing the peaks in the acoustic intensity spectra to lie below the true natural frequencies.

CHAPTER FIVE

MODELLING THE CANTILEVER BEAM

The same cantilever beam had been used to generate the acoustic field for testing the closed surface intensity mapping method (chapter 3) and then for testing the construction of acoustic intensity from pressure transfer functions (chapter 4). None of the analytical work, however, had described the actual generation of the acoustic field. It seemed that a worthwhile next step would be the characterization of the acoustic field from the beam. This required a description of the vibration response of the beam.

In this chapter, a model is developed to describe the observed vibration of a fixed-free beam. Section 5.1 begins with a review of Euler-Bernoulli beam theory. Structural damping is introduced into the differential equation of motion by letting Young's modulus become complex. Additional damping is introduced with an equivalent viscous damping term. It is shown that the damped vibration response can be expressed in terms of real eigenvalues and complex eigenfrequencies. The limitations of Euler-Bernoulli theory are then reviewed in section 5.2. Experimental measurements of the beam's vibration response had to be analyzed to obtain values for the eigenfrequencies. The method of analysis is described in section 5.3. Examples of the beam's experimental vibration response are presented, the Euler-Bernoulli modes identified and the modal damping ratios obtained in section 5.4. Young's modulus for the beam is established from the observed eigenfrequencies in section 5.5, completing the model of the beam for the lower modes. Modelled behaviour is then compared with observed vibration response in section 5.6.

5.1 Damped Response Based On Euler-Bernoulli Beam Theory

We are interested in the vibration response of a flat homogeneous beam with rectangular cross-section. At equilibrium, one can imagine a surface that bisects the beam into equal upper and lower halves, referred to as the neutral plane. The motion of the beam is described by small displacements normal to this neutral plane. At a distance x along the beam, the beam displacement W(x,t) obeys the following differential equation (Morse and Ingard, 1968, p. 175 ff),

$$\frac{\partial^4 W(x,t)}{\partial x^4} + \frac{\rho}{QK^2}\frac{\partial^2 W(x,t)}{\partial t^2} = 0 \qquad (5.1)$$

where ρ is the density of the beam, Q is Young's modulus and K is the radius of gyration of the cross section of the beam.

This equation of motion for a beam (flexible bar) is derived by treating the beam as a series of infinitesimal parallel filaments. The derivation considers rotational moments due to bending on either end of an element of the beam, shear forces in the beam element and the inertial forces acting on the element due to displacement. Inertial forces due to rotation of the element and the effects of shear deformation of the element are ignored.

For harmonic motion,

$$W(x,t) = Y(x)\, e^{-2\pi i/rt} \qquad (5.2)$$

the equation of motion reduces to,

$$\frac{\partial^4 Y(x)}{\partial x^4} - 16\pi^4\mu^4 Y(x) = 0 \qquad (5.3)$$

where $\mu=(\rho v^2/(4\pi^2 QK^2))^{1/4}$. Y(x) has solutions of the form,

$$\xi(x) = A\cosh(2\pi\mu x) + B\sinh(2\pi\mu x) + C\cos(2\pi\mu x) + D\sin(2\pi\mu x) \qquad (5.4)$$

The boundary conditions for a beam fixed at x=0 and free at x=l correspond to zero displacement and rotation at x=0 and zero bending and shearing moments at x=l. Formally these conditions are,

$$\begin{aligned} \xi(x)\big|_{x=0} &= 0 \\ \frac{\partial \xi(x)}{\partial x}\Big|_{x=0} &= 0 \\ \frac{\partial^2 \xi(x)}{\partial x^2}\Big|_{x=l} &= 0 \\ \frac{\partial^3 \xi(x)}{\partial x^3}\Big|_{x=l} &= 0 \end{aligned} \qquad (5.5)$$

Satisfaction of the boundary conditions requires,

$$\begin{aligned} C &= -A \\ D &= -B \\ B &= -A\left[\frac{\cosh(2\pi\mu l) + \cos(2\pi\mu l)}{\sinh(2\pi\mu l) + \sin(2\pi\mu l)}\right] \\ \cosh(2\pi\mu l)\cos(2\pi\mu l) &= -1 \end{aligned} \qquad (5.6)$$

The last equation is the eigenvalue equation which determines the characteristic values of μ. The eigenfunctions, $\xi(x)$, have the form,

$$\xi(x) = (\cosh(2\pi\mu x) - \cos(2\pi\mu x)) - \left[\frac{\cosh(2\pi\mu l) + \cos(2\pi\mu l)}{\sinh(2\pi\mu l) + \sin(2\pi\mu l)}\right](\sinh(2\pi\mu x) - \sin(2\pi\mu x)) \qquad (5.7)$$

It can be shown using Sturme-Liouville procedure that the eigenfunctions satisfy the

orthogonality relation,

$$(\mu_m^4 - \mu_n^4) \int_0^1 \xi_m(x)\, \xi_n(x)\, dx = 0 \qquad (5.8)$$

where $\xi_n(x)$ corresponds to the form given by Eq.(5.7) with $\mu=\mu_n$, the nth eigenvalue for μ. It follows that the eigenfunctions form a complete set.

The driven response of the beam due to a point force at $x=x_o$ with frequency ν,

$$\frac{\partial^4 Y(x)}{\partial x^4} - 16\pi^4\mu^4 Y(x) = \frac{\delta(x-x_o)}{Q K^2 S} \qquad (5.9)$$

where S is the cross sectional area of the beam, can then be expressed in terms of the eigenfunctions $\xi_n(x)$,

$$Y(x) = \frac{1}{4\pi^2\rho l S} \sum_{n=1}^{\infty} \frac{\xi_n(x_o)}{(\nu_n^2 - \nu^2)} \xi_n(x) \qquad (5.10)$$

where $\nu_n=2\pi K\mu^2(Q/\rho)^{1/2}$. The eigenfrequencies ν_n are pure real. In this case, Eq.(5.10) assumes undamped response. The response approaches infinity as ν approaches any of the eigenfrequencies.

Finite response at a natural frequency requires damping. We can argue that the beam is not perfectly elastic and some of the vibrational energy will be dissipated within the beam as it deforms. In a single degree of freedom system, structural damping can be introduced by assuming hysteretic damping and taking the spring constant to be complex (Myklestad, 1952). In our case we let Young's Modulus, Q, become complex,

$$Q = Q_1 + iQ_2, \quad |Q_2| \ll Q_1, \quad Q_2 < 0 \tag{5.11}$$

Assume the beam to be lightly damped (damping effects small except at resonance) so that non viscous damping effects can be modelled in terms of equivalent viscous dampers (Norton, 1994). An equivalent viscous damping term (coefficient R(ν)) is introduced into the differential equation to account in some fashion for the energy lost to the surrounding fluid.

$$\frac{\partial^4 W(x,t)}{\partial x^4} + \frac{R(\nu)}{QK^2S}\frac{\partial W(x,t)}{\partial t} + \frac{\rho}{QK^2}\frac{\partial^2 W(x,t)}{\partial t^2} = 0 \tag{5.12}$$

For harmonic motion we obtain,

$$\frac{\partial^4 Y(x)}{\partial x^4} - \frac{1}{QK^2}\left[4\pi^2\rho\nu^2 + i\frac{2\pi R(\nu)}{S}\nu\right]Y(x) = 0 \tag{5.13}$$

If we choose our eigenvalues to be real, in particular,

$$\frac{1}{QK^2}\left[4\pi^2\rho\nu^2 + i\frac{2\pi R(\nu)}{S}\nu\right] = 16\pi^4\mu_n^4 \tag{5.14}$$

we recover the same differential equation as before. Now the eigenfrequencies become complex. The nth mode eigenfrequency $\nu_n=\nu_{1n}+i\nu_{2n}$, is given by,

$$\begin{aligned} \nu_{1n} &= \sqrt{\frac{\nu_{on}^2}{2} - \frac{\alpha^2}{8} + \frac{1}{2}\sqrt{(\nu_{on}^2 - \frac{\alpha^2}{4})^2 + \eta^2\nu_{on}^4}} \\ \nu_{2n} &= \frac{-(\eta\nu_{on}^2 + \alpha\nu_{1n})}{2\nu_{1n}} \end{aligned} \tag{5.15}$$

where ν_{on} (the nth mode undamped natural frequency (Q_2=0, R(ν)=0)), and α and η are given by,

$$\nu_{on} = 2\pi K\mu_n^2\sqrt{\frac{Q_1}{\rho}}$$

$$\alpha = \frac{R(\nu)}{2\pi\rho S} \qquad (5.16)$$

$$\eta = \frac{-Q_2}{Q_1}$$

The result is that the damped response is given by equation (5.10), using the complex eigenfrequencies ν_n defined in equation (5.15).

The advantage of this formulation is that it is only necessary to know the real and imaginary parts of the natural frequencies to characterize response. The disadvantage of this formulation is that the contributions to damping from different processes are not distinguishable.

5.2 Limitations of Euler-Bernoulli Beam Theory

The Euler-Bernoulli formulation assumes two dimensional bending along the length of the beam without flexure across the width of the beam. The relative shape of the $\xi_n(x)$ for n=1 to 5, (i.e. the first five mode shapes) is shown in Fig. 5.1. Effects associated with Poisson's ratio (the curling up of the beam edges in the width direction as the beam bends in the length direction) are ignored. Modes that involve bending in the directions of both length and width are also excluded from consideration (eg. torsional modes involve a twisting rotation about the centreline of the beam).

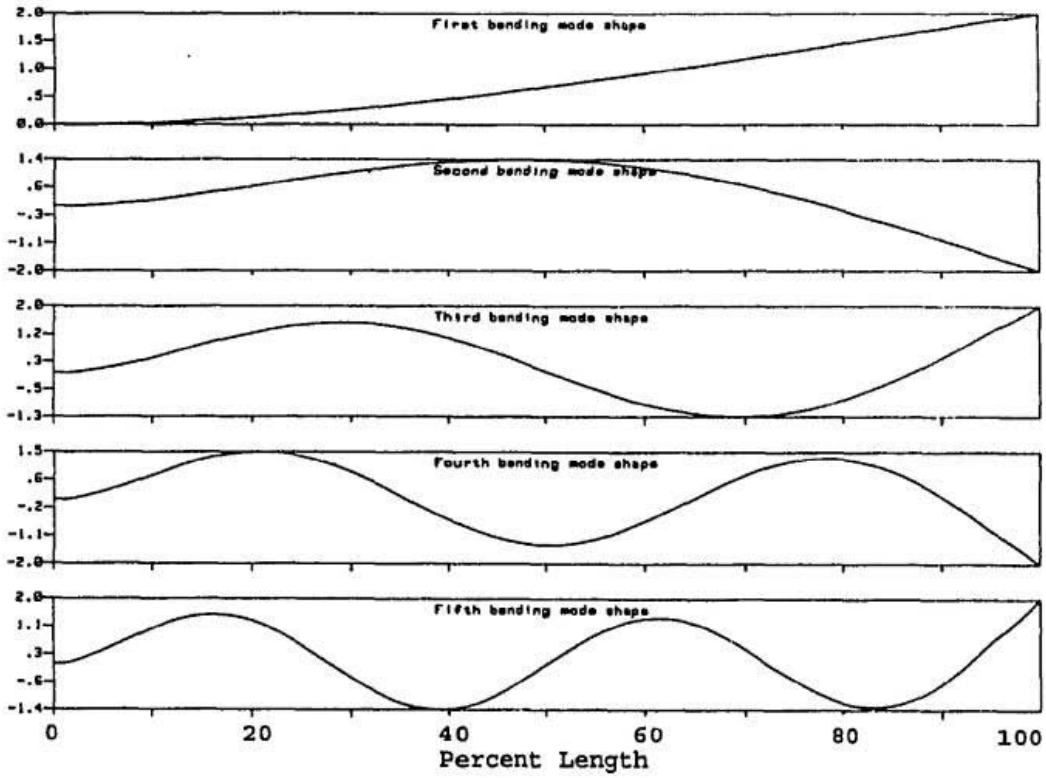

Figure 5.1: Eigenfunction shapes of the first five beam bending modes.

Inclusion of these effects requires the more general theory of plate vibration which accomodates bending in both directions. The main difference between beam and plate theory is that the $\partial^4/\partial x^4$ operator in the differential equation is replaced with the ∇^4 operator (see Morse and Ingard, 1968, p.214).

For an infinite plate, travelling wave solutions to the Euler-Bernoulli differential equation have a group velocity that is inversely proportional to the flexural wavelength (Junger and Feit, 1986). The group velocity tends to infinity as the wavelength approaches zero. This physically unrealistic result is because Euler-Bernoulli theory ignores both the rotational inertia in the beam and deformation caused by shear within the beam. Inclusion of these effects (Timoshenko, 1921) adds two more differential operators, $\partial^4/\partial x^2\partial t^2$ and $\partial^4/\partial t^4$ into the differential equation. Travelling wave solutions to the Timoshenko Beam Equation have the proper limiting phase velocity (Junger and Feit, 1986).

The Euler-Bernoulli description assumes a beam thickness that is small relative to both beam length, and to the characteristic wavelength that would propagate at the frequency of interest (Junger and Feit, 1986). Bending in the direction of beam width is ignored altogether.

5.3 Experimental Analysis Using the Single Degree of Freedom Assumption

Experimental data analysis assumed the vibration response near a natural frequency approximated that of a single degree of freedom system (see Ewins, 1986). Consider the case where the driving frequency ν is close to one of the natural frequencies ν_m. We write the response (Eq.(5.10)) as,

$$Y(x) = \frac{1}{4\pi^2\rho lS}\left[\frac{\xi_m(x_o)}{(\nu_m^2 - \nu^2)}\xi_m(x) + \sum_{n=1,n\neq m}^{\infty}\frac{\xi_n(x_o)}{(\nu_n^2-\nu^2)}\xi_n(x)\right] \qquad (5.17)$$

Provided the natural frequencies are well separated the second term will vary slowly with ν compared to the first term. For ν close to ν_m, the second term is treated as constant,

$$Y(x)_{\nu=\nu_m} \doteq \frac{1}{4\pi^2 \rho l S} \frac{\xi_m(x_o)}{(\nu_m^2 - \nu^2)} \xi_m(x) + G \qquad (5.18)$$

Single degree of freedom analysis provided a means of establishing natural frequency and mode shape while limiting the number of unknowns. Curve fitting the region of peak response to Eq.(5.18) was used to solve for $Re(\nu_m)$, $Im(\nu_m)$, $\xi_m(x_o)\xi_m(x)$ and G. Since x_o was fixed $\xi_m(x_o)$ was a constant. Plotting $\xi_m(x_o)\xi_m(x)$ versus position identified the shape of $\xi_m(x)$.

5.4 The Experimental Cantilever Beam

The same beam described in chapter 3 was used. The beam measured 649 mm long, 204 mm wide and approximately 9.5 mm thick (see Fig. 3.3). The experimental setup is shown in Fig. 5.2. Force was applied on the centreline of the beam at the free end for all measurements. This location favoured exciting beam bending modes over torsional modes because the centreline was a nodal line for torsional modes. The FRF's (frequency response functions) were measured as the ratio of acceleration to applied force in the frequency domain.

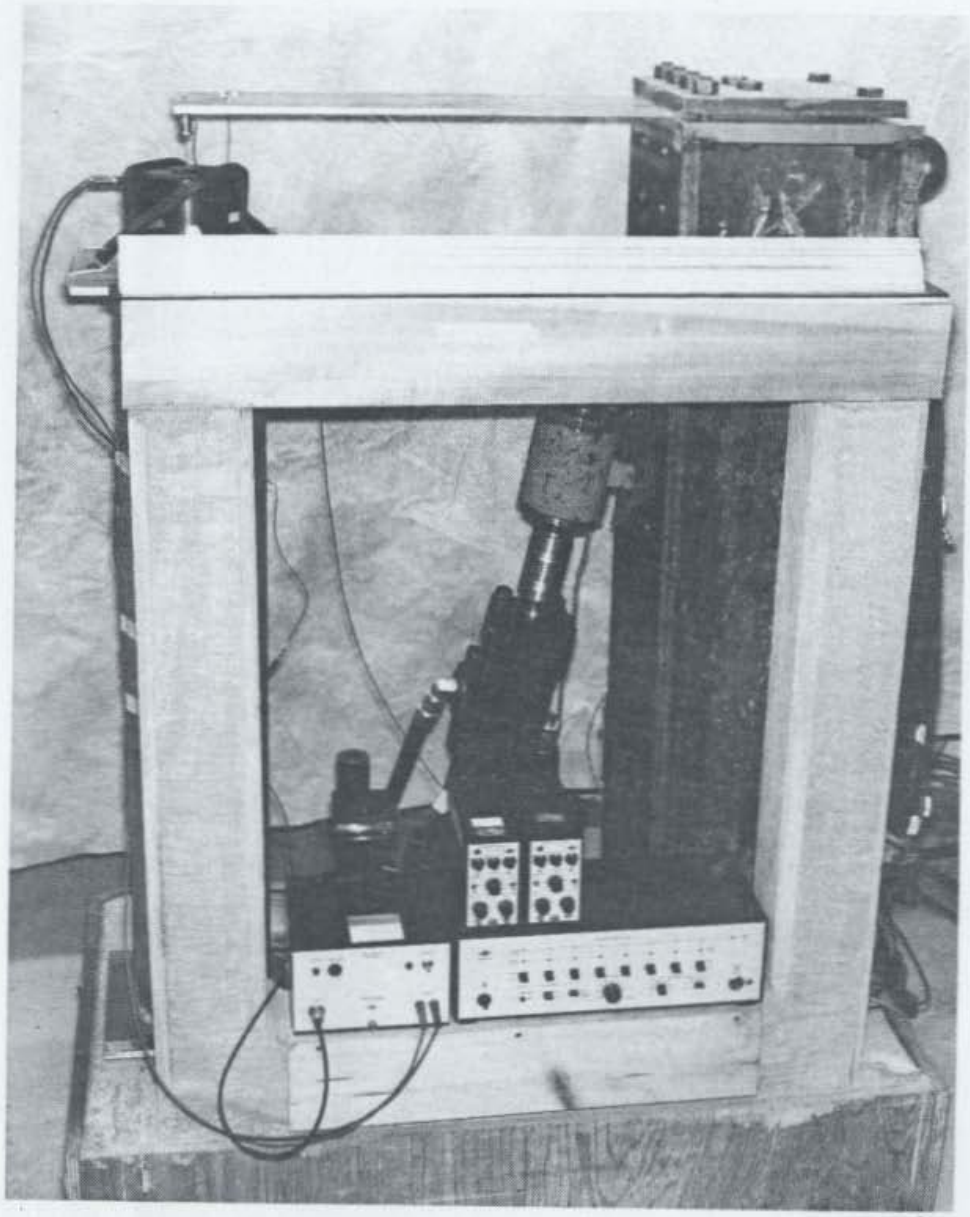

Figure 5.2: Photograph of the cantilever beam held in the fixed-free condition

Fig. 5.3 shows an FRF in the 0 to 800 Hz range measured at the free end of the beam on the centreline. The four peaks in Fig. 5.3 correspond to the first four beam bending modes (18, 112, 313 and 613 Hz). By comparison an FRF measured with the accelerometer in the corner of the free end of the beam Fig. 5.4 shows the same four peaks associated with beam bending modes with three new peaks associated with torsional modes. Fig. 5.5 shows the acceleration FRF in the 800 to 1600 Hz region at the free end on the centreline. Of the five peaks, two are beam bending modes. The first two peaks at 1015 and 1030 Hz belong to the same fifth beam bending mode. The split may have been due to imperfect boundary conditions. The sixth beam bending mode occurred at 1534 Hz. The three other peaks corresponded to other mode types. Table 5.1 lists the observed natural frequencies and damping ratios for the first eight Euler-Bernoulli beam bending modes.

Table 5.1: Observed natural frequencies and damping ratios

Euler-Bernoulli Beam Bending Mode	Frequency Hz	Damping Ratio ν_{2n}/ν_{1n}
1	17.99	8.06×10^{-4}
2	111.5	7.20×10^{-4}
3	313.0	5.37×10^{-4}
4	612.7	1.62×10^{-3}
5*	1014.5	6.33×10^{-4}
6	1533.5	8.32×10^{-4}
7	2123.	9.69×10^{-4}
8	2836.	9.51×10^{-4}

* Split peak.

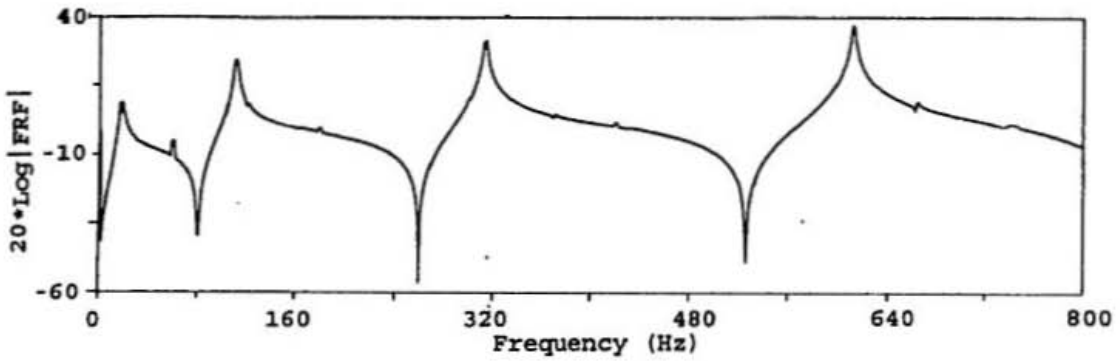

Figure 5.3: Cantilever beam FRF at the free end on the centreline of the beam, 0 to 800 Hz.

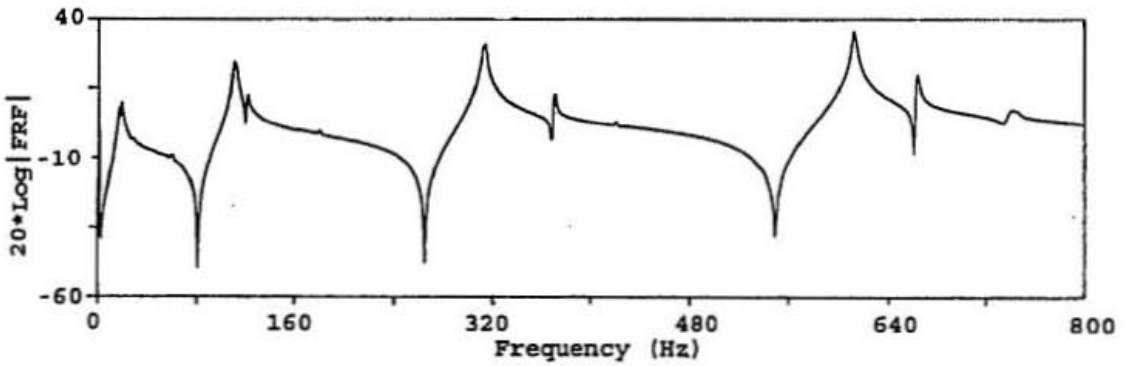

Figure 5.4: Cantilever beam FRF at the free end on the corner of the beam, 0 to 800 Hz.

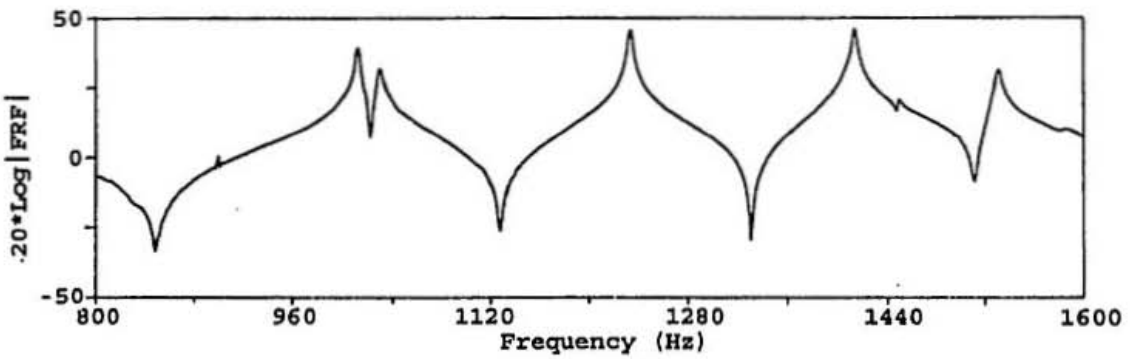

Figure 5.5: Cantilever beam FRF at the free end on the corner of the beam, 800 to 1600 Hz.

The damping ratios were of the order of 10^{-3} indicating the cantilever was indeed lightly damped. In general the natural frequencies were well separated as required for the single degree of freedom assumption.

5.5 Parameter Values and Approximations

While the observed damping ratios were used to establish the ratio of ν_{2n} to ν_{1n}, the model was used to calculate the values of ν_{1n}. Assuming a lightly damped system the model used the approximation that $\nu_{1n} \doteq \nu_{on}$ (i.e. $\alpha << \nu_{on}$ and $\eta << 1$ in Eq.(5.15)). In practice this meant calculating ν_{on}.

$$\nu_{1n} \doteq \nu_{on} = 2\pi K \mu_n^2 \sqrt{\frac{Q_1}{\rho}} \qquad (5.19)$$

Calculation of ν_{on} required values for K, Q_1, ρ, and μ_n. For a beam with rectangular cross section and thickness h, K = 0.289·h. The density of mild steel was taken to be 7,860 Kg/m^3 [Science Data Book, 1971]. Values for μ_n were obtained by numerically solving the eigenvalue equation (Eq.(5.6)). Only the value of Q_1 remained to be specified.

A value for Q_1 first required an estimate of η. Following the travelling wave method [Physical Acoustics, 1964] an approximate value of 8×10^{-4} for η_{steel} was calculated using tabulated values for longitudinal waves in tool steel (velocity in thin bars=5116 m/s, bulk wave velocity=5874 m/s, attenuation=4.94 nepers/m [Kaye and Laby, 1973]). With $|\eta| << 1$, the value of Q_1 was approximated with the tabulated value of Young's modulus for mild steel, 2.119×10^{11} Pa [Kaye and Laby, 1973].

Table 5.2 shows the values that were then calculated for ν_{on}. The natural frequencies were uniformly overestimated by 5 to 6 %.

Table 5.2: Natural frequencies calculated with Q_1=2.119 x 10^{11} Pa.

Mode n	$2\pi\mu_n l$	Calculated Frequency	Measured Frequency	Calculated/Measured
1	1.875	18.9	18.0	1.05
2	4.694	118.4	111.5	1.06
3	7.855	331.6	313.0	1.06
4	10.996	649.7	612.7	1.06
5	14.137	1073.9	1014.5	1.06
6	17.279	1604.4	1533.5	1.05
7	20.420	2240.7	2123.	1.06
8	23.562	2983.3	2836.	1.05

Subsequent measurements with a micrometer (9.5 mm was obtained using calipers) showed the beam thickness was 9.33 ± 0.17 mm. Measurements of beam mass and volume showed the beam density to be within 1 % of the assumed value. The errors in thickness and density were insufficient to account for the observed bias. If the Euler-Bernoulli theory was biased towards overestimating natural frequency one would have expected the percentage error to increase with frequency. The percentage error appeared to be independent of frequency. It was possible that the value used for Young's modulus was incorrect. Eq.(5.19) was rearranged to provide an independent estimate of Young's modulus at each observed natural frequency.

$$Q_1 = \frac{\rho v_{in}^2}{4\pi^2 K^2 \mu_n^4} \qquad (5.20)$$

Table 5.3 lists the values of Young's modulus calculated with Eq.(5.20).

Table 5.3: Values of Young's modulus calculated from natural frequencies

Euler-Bernoulli Beam Mode No.	Frequency (Hz)	Calculated Young's Modulus (Pa)
1	17.99	1.987×10^{11}
2	111.5	1.943×10^{11}
3	313.0	1.953×10^{11}
4	612.7	1.949×10^{11}
5	1014.5	1.955×10^{11}
6	1533.5	2.002×10^{11}
7	2123.	1.967×10^{11}
8	2836.	1.980×10^{11}

The average of the calculated values was $1.967 \pm 0.021 \times 10^{11}$ Pa, about 7 % below the tabulated value originally used for Q_l. The method employed here to estimate Young's modulus was quite similar to that described by Spinner and Tefft [1961], where laboratory specimens in the freely suspended condition, were excited into resonance. The leading term in the formula given by Spinner and Tefft to determine Young's Modulus from the fundamental flexural frequency for prismatic bars is exactly that obtained from Euler-Bernoulli theory for a free-free beam.

It could be argued that the the difference in the values for Young's modulus was related to the specific measurement method employed. However, Wolfenden et al [1989] conducted an interlaboratory testing program which compared measurements of Young's modulus for metals by different methods including the resonance method described by

Spinner and Tefft. All the methods obtained the same value of Young's modulus to within 1.6 % of each other. The different methods spanned a frequency range from 780 Hz to 15 Mhz. The measurement at the lowest frequency came from the suspended free-free beam resonance method.

Under the circumstances, it was deemed reasonable to use the calculated value of Young's modulus, 1.967×10^{11} Pa, for Q_1. The 0 to 800 Hz region containing the lowest four beam modes was modelled. The beam's vibration response was calculated in terms of acceleration, $-\omega^2 Y(x)$, using Eq.'s (5.10) and (5.19), with the damping ratios in Table 5.1. Calculated response summed the contributions from the first 8 beam modes, 4 modes above the highest mode of interest.

5.6 Comparison With Experimental Measurement

The calculated vibration response was compared with the beam's measured FRF's. Overall agreement was examined using measured FRF's with a frequency resolution of 1 Hz that spanned the entire region of interest, 0 to 800 Hz. These FRF's were appropriate to examine the extended regions between natural frequencies, but not the sharp response near resonance where their coarse resolution caused distortion. Agreement close to the natural frequencies was examined separately using measured FRF's with higher frequency resolution.

We begin by examining several cases of overall agreement. Fig. 5.6 compares measured response (solid line) with calculated response (dotted line) near the free end of the beam. Calculated response magnitude had the same basic shape and features as

measured response with the exception that the local minima of the calculated response were sometimes shifted in frequency from the observed local minima. When the calculated and observed minima were offset in frequency, so were the large phase transitions that accompanied those features.

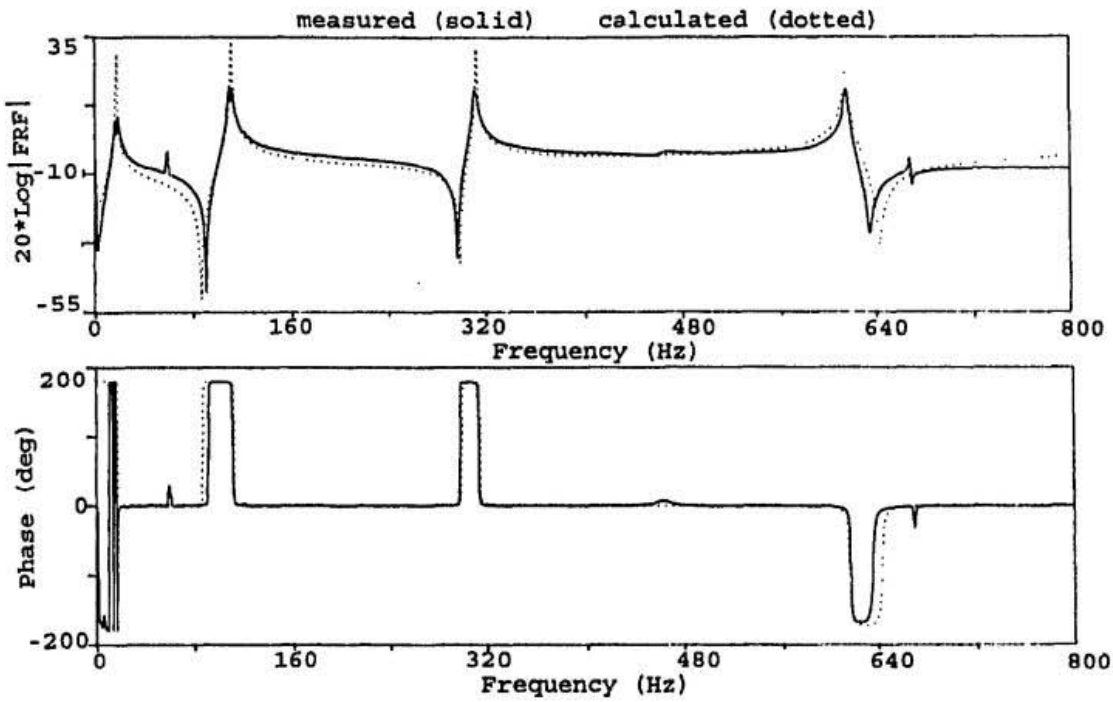

Figure 5.6: Comparison of calculated and measured response in the region between natural frequencies at 90 % span of the beam (x=576 mm). The frequency span of 800 Hz required coarse frequency resolution causing the observed response at the natural frequencies to be underestimated. Electrical interference caused the spike at 60 Hz.

Fig. 5.7 compares measured response with calculated response in between midspan and the free end of the beam (x=384 mm). Again overall shape is good but clearly affected by the difference between the frequencies of calculated and measured minima.

Plotted phase had a discontinuity at ± 180° although the two angles were equivalent. Small changes in measured phase at those angles were responsible for transitions in the plot as the phase jumped from 180° to -180° and vice versa.

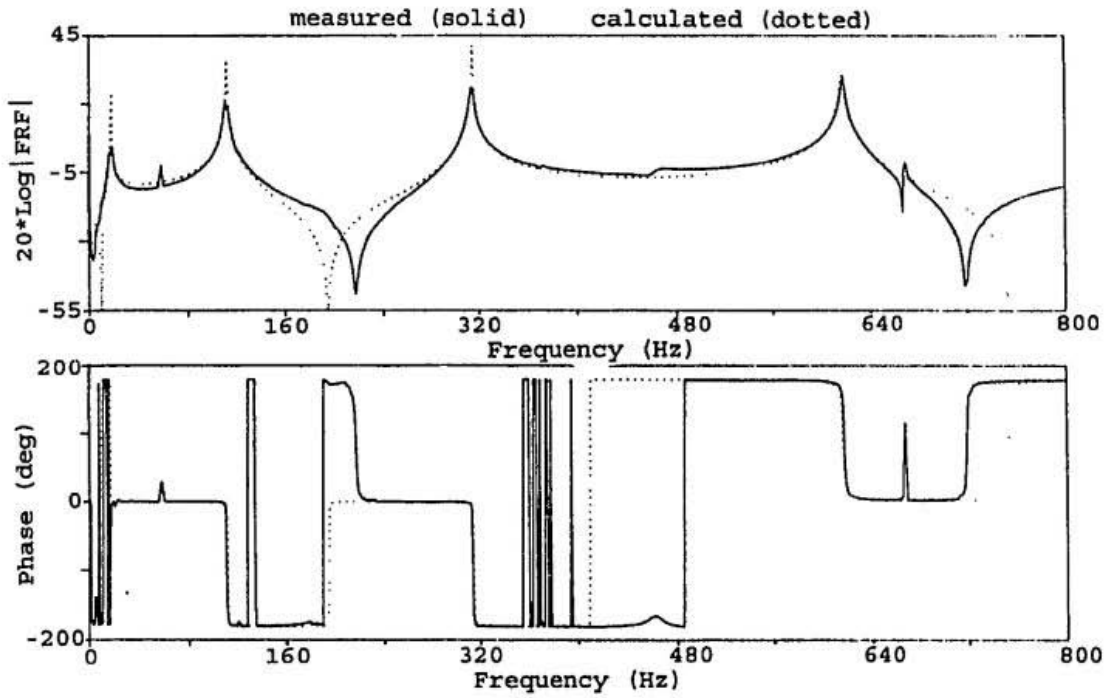

Figure 5.7: Comparison of calculated and measured response in the region between natural frequencies at 60 % span of the beam (x=384 mm).

Fig. 5.8 compares measured response with calculated response in between the midspan and fixed end of the beam (x=256 mm). Fig. 5.9 compares measured response with calculated response close to the fixed end of the beam (x=128 mm). Similar comments apply to both figures. Overall the agreement was favourable.

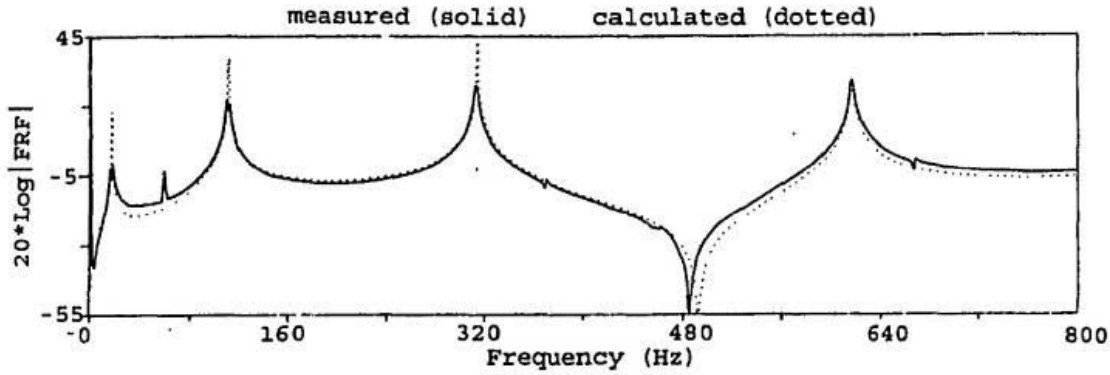

Figure 5.8: Comparison of calculated and measured response in the region between natural frequencies at 40 % span of the beam (x=256 mm).

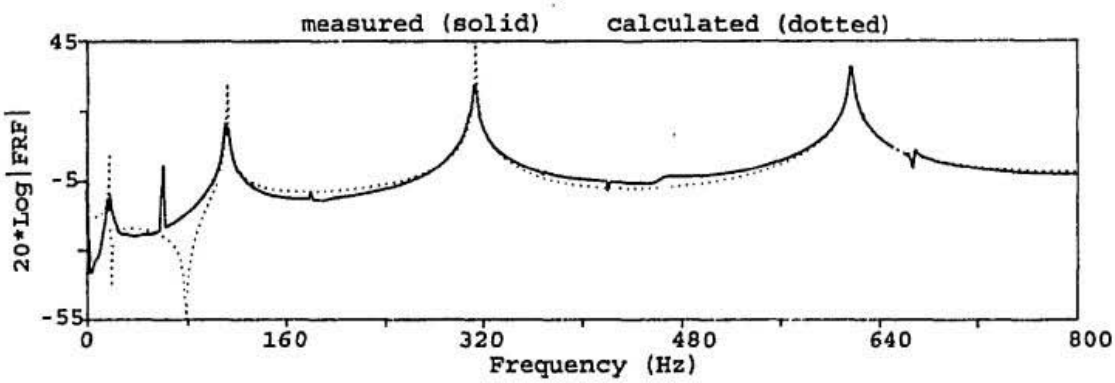

Figure 5.9: Comparison of calculated and measured response in the region between natural frequencies at 20 % span of the beam (x=128 mm).

Now we turn our attention to the response close to the natural frequencies. Fig. 5.10 shows the typical agreement between calculated and measured response in the region of the first beam mode. The measured FRF had a frequency resolution of 0.00391 Hz in order to properly replicate the shape of peak response. The measured response contains variations at 18.0 Hz that differentiate it from the assumed smooth response. The fine frequency scale shows the small offset (0.09 Hz) between the observed and calculated natural frequencies. With this resolution we can see that the magnitude of peak response was slightly underestimated by 1 dB. Overall the agreement was reasonable.

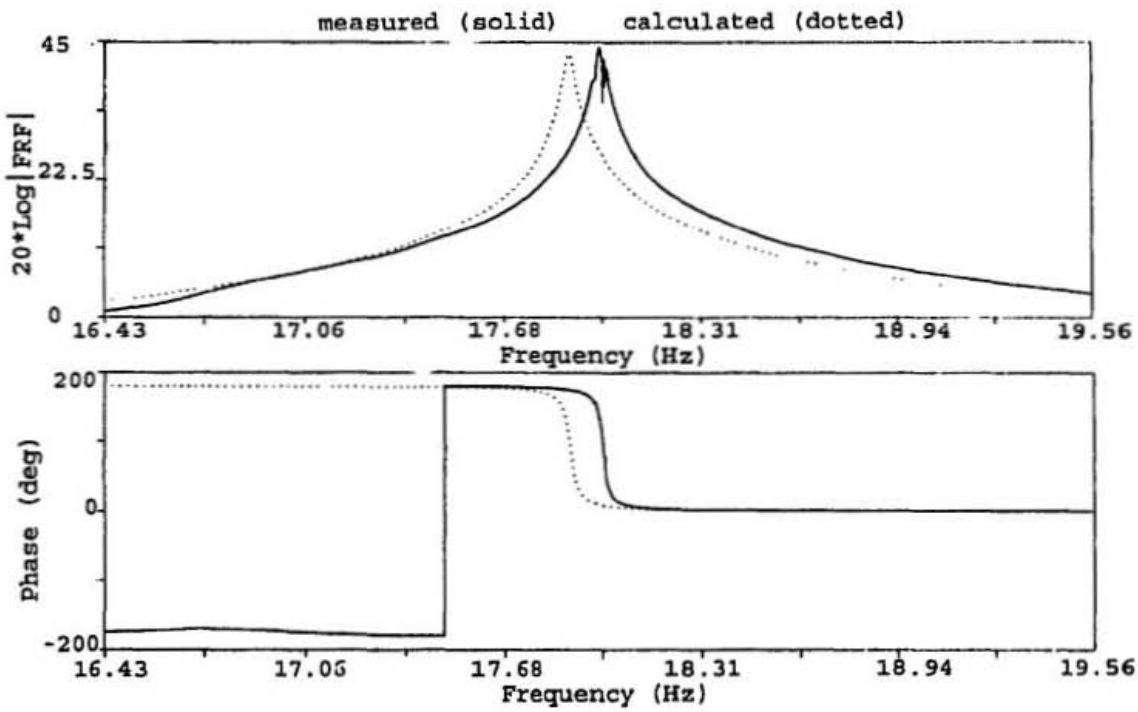

Figure 5.10: Comparison of calculated and measured response at the first beam mode at 70 % span of the beam (x=448 mm).

Similar agreement was observed in the region of the second beam mode at three positions on the beam corresponding to 40, 70 and 100 % span from the fixed end. Fig. 5.11 shows this typical agreement at 70 % span (x=448 mm). The fine frequency resolution highlights the small offset (0.7 Hz) between observed and calculated natural frequency. Calculated and measured peak response were within 1 dB in magnitude. The least agreement (Fig. 5.12) occurred close to the fixed end (10 % of span). Peak response at that position was underestimated by 2.5 dB and the curve shapes differed.

There was reasonably good agreement in the region of the third beam mode at five of six positions (corresponding to 20, 40, 70, 80 and 100 % of span). Fig. 5.13 shows this typical agreement close to the fixed end (x=128 mm). Calculated and measured peak response were within 1 dB in magnitude. The least agreement occurred at mid span (x=320 mm) (Fig. 5.14) which was a node for the third beam mode. Measured and calculated response differed by almost 10 dB at this position, but remained small compared to the other positions.

Lastly reasonable agreement was observed in the region of the fourth beam mode at ten positions spaced every 64 mm along the beam. Fig. 5.15 shows the typical agreement between measured and calculated response towards the fixed end at 30 % span (x=192 mm). Here the calculated peak value overestimated the response by 1 dB. One position closer to the fixed end (x=128 mm) showed almost perfect agreement apart from the frequency shift (Fig. 5.16). Over the ten positions the cases of under and over estimation were roughly equal. There did not appear to be a net bias.

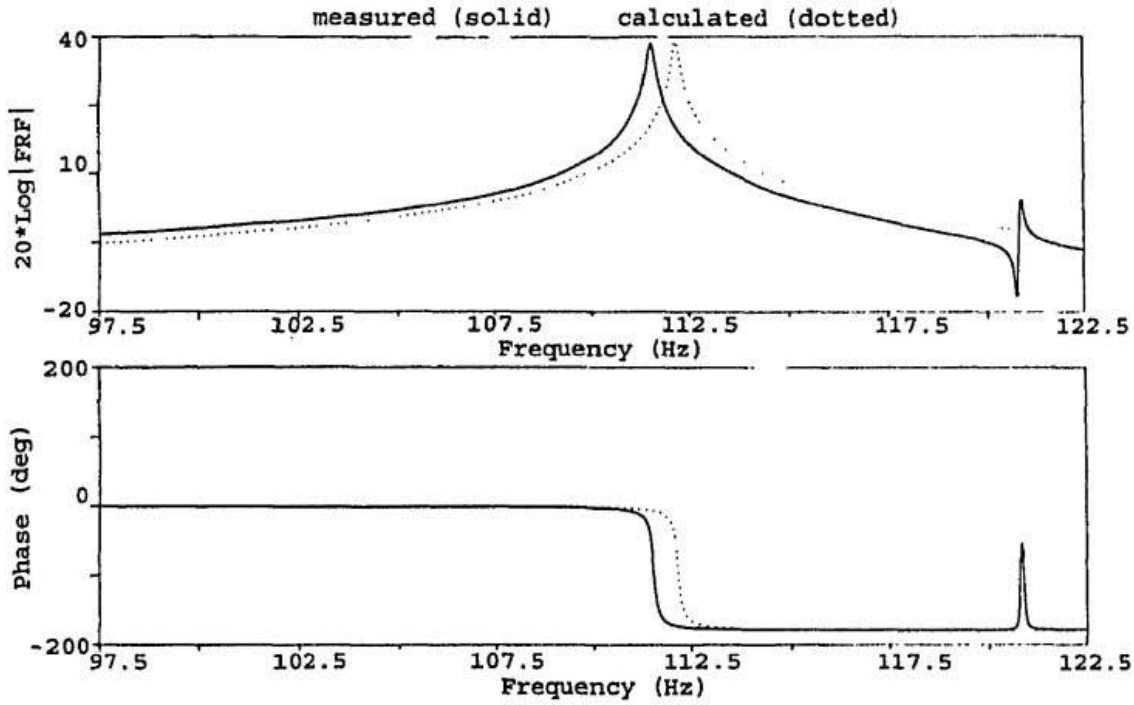

Figure 5.11: Comparison of calculated and measured response at the second beam mode at 70 % span of the beam (x=448 mm).

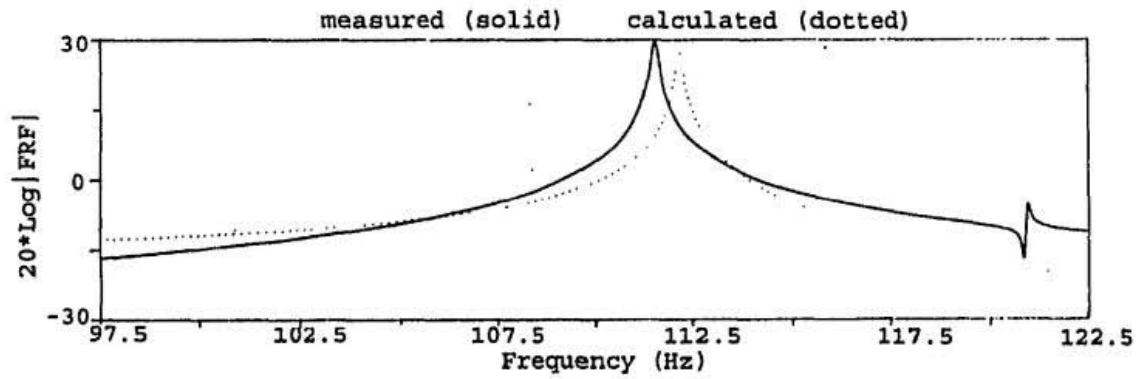

Figure 5.12: Comparison of calculated and measured response at the second beam mode close to the fixed end at 10 % span of the beam (x=64 mm).

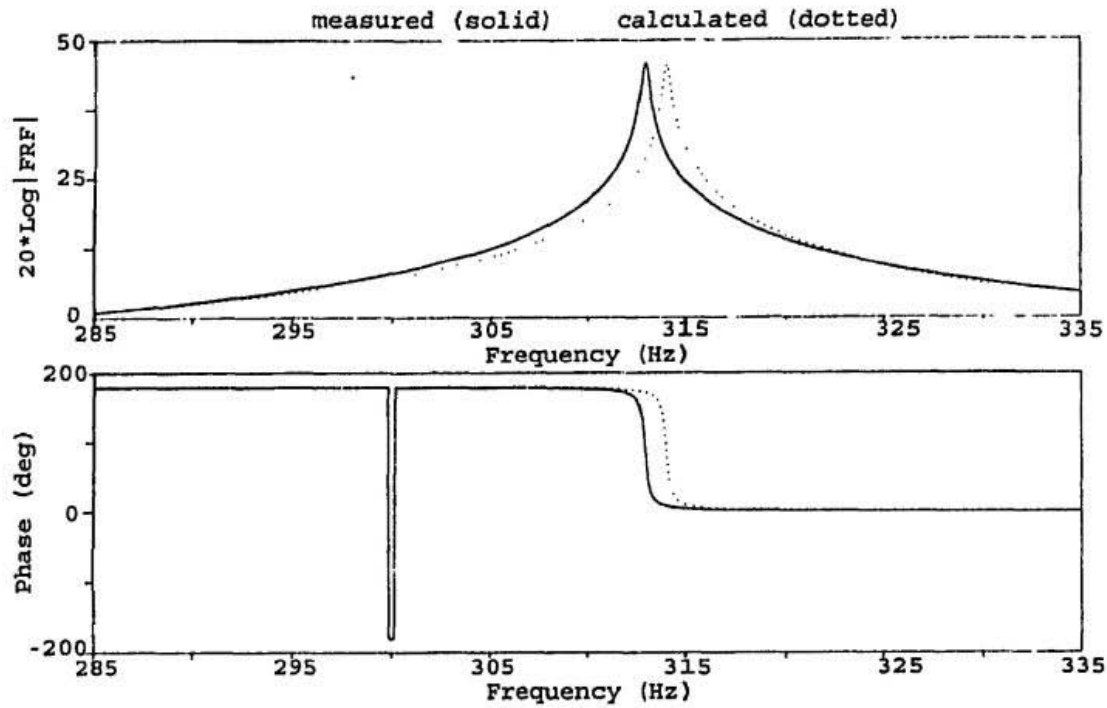

Figure 5.13: Comparison of calculated and measured response at the third beam mode close to the fixed end at 20 % span of the beam (x=128 mm).

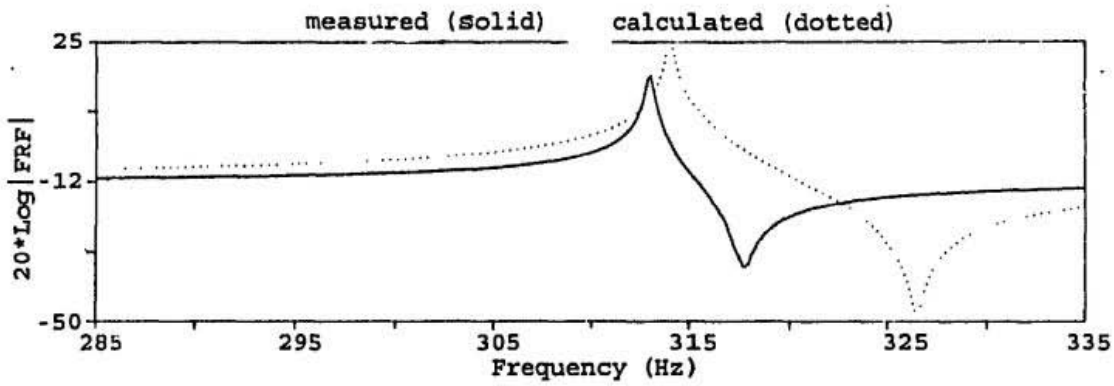

Figure 5.14: Comparison of calculated and measured response at the third beam mode, close to a node (x=320 mm).

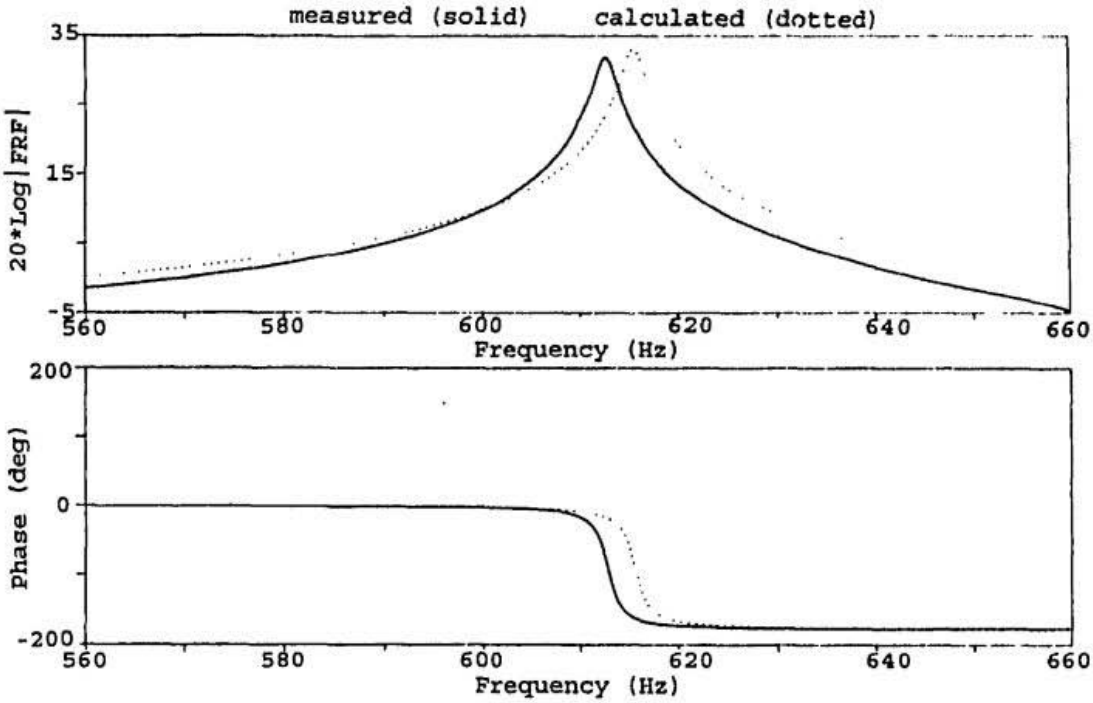

Figure 5.15: Comparison of calculated and measured response at the fourth beam mode, near the fixed end (x=192 mm).

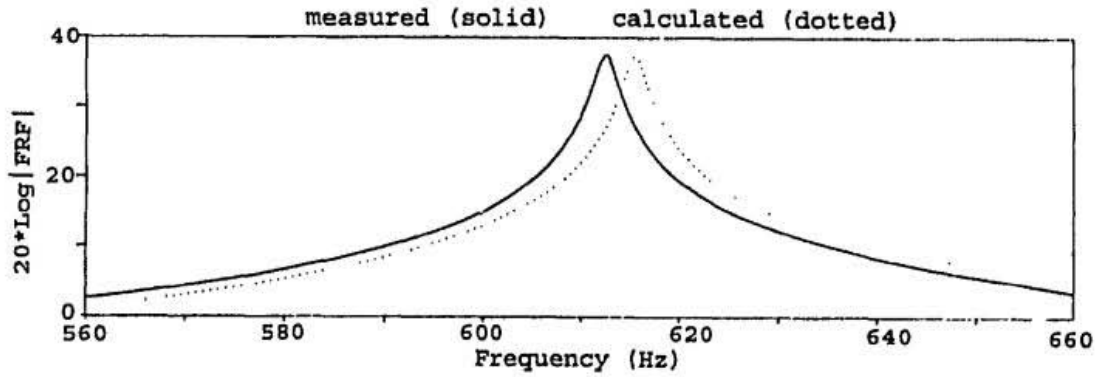

Figure 5.16: Comparison of calculated and measured response at the fourth beam mode, near the fixed end (x=128 mm).

5.7 Summary

The modelled response was typically within 2 to 3 dB of the observed response everywhere except in the regions of local minima. There, the frequencies where the calculated minima occurred were sometimes offset from the frequencies of the observed minima. This may have been due to the truncated series (8 modes) used to calculate response, or the limitations of Euler-Bernoulli beam theory.

In the natural frequency regions, which were the main areas of interest, the model replicated the observed response quite well, usually within ±1 dB in magnitude. On a fine frequency scale, the calculated and observed response typically differed by less than 0.7 % in frequency. This typical close alignment in frequency of calculated and observed peak response was attributed to having obtained a good estimate of Young's modulus for the beam. The next step was to incorporate the model of vibration response into a model for the radiated acoustic field.

CHAPTER SIX

MODELLING THE NEAR FIELD OF THE CANTILEVER BEAM

An integral expression for the acoustic field from a planar source in free space was used to model the near field of the beam. The motion of the planar source was described by the model developed in chapter 5. The modelled field was compared with the observed field of the beam in its reverberant environment. Both the modelled and measured fields were then used to examine the spatial variation of phase in the near field of the beam, and the consequent impact on the measurement of acoustic intensity.

Section 6.1 reviews the development of integral expressions for pressure. Section 6.2 discusses the conditions under which an integral expression was assumed to provide a reasonable approximation of the near acoustic field above the beam. Section 6.3 compares examples of the acoustic field calculated from the integral expression with measurement. Section 6.4 examines the spatial variation of phase in the near field above the beam and the consequences to near field acoustic intensity measurements.

6.1 Integral Expression for an Acoustic Field

The acoustic near field above the cantilever beam was approximated using an integral expression for pressure. The development of such an integral expression for an acoustic field is briefly reviewed below and can be found in several texts (e.g. Morse and Ingard, 1968, p. 320 ff).

Consider an acoustic source $S(\bar{x})$ contained in a volume V bounded by a surface A. The acoustic differential equation is,

$$\nabla^2 p(\vec{x};t) - \frac{1}{c^2}\frac{\partial^2 p(\vec{x};t)}{\partial t^2} = S(\vec{x};t) \qquad (6.1)$$

With harmonic ($e^{-i\omega t}$) time dependence, the differential equation reduces to,

$$\nabla^2 p(\vec{x}) + \frac{\omega^2}{c^2} p(\vec{x}) = S(\vec{x}) \qquad (6.2)$$

We will make use of a Green's function $G(\vec{x},\vec{x}')$ that satisfies,

$$\nabla^2 G(\vec{x},\vec{x}') + \frac{\omega^2}{c^2} G(\vec{x},\vec{x}') = \delta(\vec{x}-\vec{x}') \qquad (6.3)$$

For the moment, the form of $G(\vec{x},\vec{x}')$ remains unspecified. $G(\vec{x},\vec{x}')$ and $p(\vec{x})$ are then subsituted into Green's second identity,

$$\int_V G(\vec{x},\vec{x}')\nabla^2 p(\vec{x}) - p(\vec{x})\nabla^2 G(\vec{x},\vec{x}')\, dV = \iint_A [G(\vec{x},\vec{x}')\nabla p(\vec{x}) - p(\vec{x})\nabla G(\vec{x},\vec{x}')] \bullet dA \qquad (6.4)$$

Further subsitution of Eq.'s (6.2) and (6.3) into (6.4) leads to,

$$p(\vec{x}') = \int_V S(\vec{x}) G(\vec{x},\vec{x}')\, dV + \int_A [p(\vec{x})\nabla G(\vec{x},\vec{x}') - G(\vec{x},\vec{x}')\nabla p(\vec{x})] \bullet dA \qquad (6.5)$$

This is the integral equation of interest. To make use of this equation, we need the form of $G(\vec{x},\vec{x}')$ which depends on the boundary conditions of the problem.

First, consider the case of a localised source in free space with no boundaries. The boundary condition on $p(\vec{x}')$ is that it vanish as $\vec{x}'$ tends to infinity. The Green's function which satisfies this condition is,

$$G(\vec{x},\vec{x}') = \frac{e^{ik|\vec{x}-\vec{x}'|}}{4\pi|\vec{x}-\vec{x}'|}, \quad (free\ space) \tag{6.6}$$

The volume V enclosing the source can be extended to infinity and surface integral in Eq.(6.4) can be shown to vanish leaving,

$$p(\vec{x}') = \int_V S(\vec{x}) \frac{e^{ik|\vec{x}-\vec{x}'|}}{4\pi|\vec{x}-\vec{x}'|} dV, \quad (free\ space) \tag{6.7}$$

Secondly, consider the case of an infinite rigid baffle below the source. For convenience the baffle is chosen to lie in the x-y plane. The boundary condition at the baffle surface is that the normal component of fluid particle velocity must vanish. Therefore the normal derivative of pressure must vanish. The Green's function which satisfies this condition (see Morse and Ingard, 1968, p. 369) is,

$$G(\vec{x},\vec{x}') = \frac{e^{ik|\vec{x}-\vec{x}'|}}{4\pi|\vec{x}-\vec{x}'|} + \frac{e^{ik|\vec{x}^*-\vec{x}'|}}{4\pi|\vec{x}^*-\vec{x}'|}, \quad (baffle\ in\ x\text{-}y\ plane) \tag{6.8}$$

where $\vec{x}$=(x,y,z) and $\vec{x}^*$=(x,y,-z). Again the surface integral in Eq.(6.4) vanishes, leaving,

$$p(\vec{x}') = \int_V S(\vec{x}) \left[\frac{e^{ik|\vec{x}-\vec{x}'|}}{4\pi|\vec{x}-\vec{x}'|} + \frac{e^{ik|\vec{x}^*-\vec{x}'|}}{4\pi|\vec{x}^*-\vec{x}'|}\right] dV, \quad (baffle) \tag{6.9}$$

When the source is planar and lies in the plane of the baffle (z=0), the Green's function in Eq.(6.8) reduces to the free space Green's function in Eq.(6.6) multiplied by a factor of two (Pierce, 1991 p. 214.).

6.2 Obtaining an Estimate of the Near Field

The beam was treated as a planar source lying in the x-y plane. The volume integral in Eq.(6.7) reduced to the following integral over the surface of the beam,

$$p(\bar{x}') = \int_{\text{beam surface}} \rho_o \omega^2 Y(\bar{x}) \frac{e^{ik|\bar{x}-\bar{x}'|}}{4\pi|\bar{x}-\bar{x}'|} dA, \quad (\textit{free space}) \qquad (6.10)$$

The use of this expression was restricted to the centreline of the beam, close to the beam's surface, where the radiated sound could be attributed mainly to the vibration of the upper beam surface.

In reality, the acoustic field surrounding the beam consisted of the field radiated by the beam plus that which had been scattered by the walls and other objects in the room. The use of this equation assumed that as the measurement point approached the surface of the beam, the radiated component would eventually dominate over the scattered component (i.e. provided the measurement point remained close to the surface of the beam, the scattered field could be ignored). Comparison of experimental and calculated pressure would show how appropriate this assumption was in practice.

If the beam had been suspended in free space, the acoustic field in the upper half plane above the beam would have been symmetric in magnitude but 180° out of phase with that in the lower half plane. A consequence of this antisymmetry was that the pressure would vanish in the surrounding x-y plane. Clearly the contributions to the acoustic field from both the beam's upper and lower surfaces are required to obtain the correct model of the acoustic field. However, close to the beam's surface and away from the edges of the beam, the near side of the beam was expected to be the main contributor to the radiated acoustic field.

From the setup shown in Fig. 5.2, looking down from above the beam, the

clamped end was effectively baffled by the I-beam support, while the free end was suspended in relatively free space. The beam itself also acted as a baffle. Therefore it was anticipated that the radiated field close to the beam's surface would lie between the values associated with the baffled and free space conditions (i.e. between the value calculated from Eq.(6.10) and twice that value.).

Eq.(6.10) used the expression for Y(x) developed in chapter 5. The double integral over the surface of the beam was numerically evaluated in both x and y directions with an extended Simpson's Rule algorithm (Press et al, 1990).

6.3 Comparison With Experimental Measurement

PTF (pressure transfer function) measurements used the same setup as previously described in chapter 4 (see Fig. 4.1). The excitation point was still the centre of the free end of the beam. Comparison between the measured and calculated (Eq.(6.10)) PTF's took place in the same manner as for FRF's in chapter 5. Coarse resolution PTF's were used to examine the agreement in the regions between natural frequencies, and fine resolution PTF's were used to examine the agreement in the vicinity of the natural frequencies.

Coarse resolution PTF's were collected at x = 128, 256, 384 and 512 mm from the fixed edge of the beam at altitudes of 35 and 85 mm. Fig. 6.1 compares calculated and measured PTF's close to the free end of the beam at 80 % span (x=512 mm) at an altitude of 35 mm.

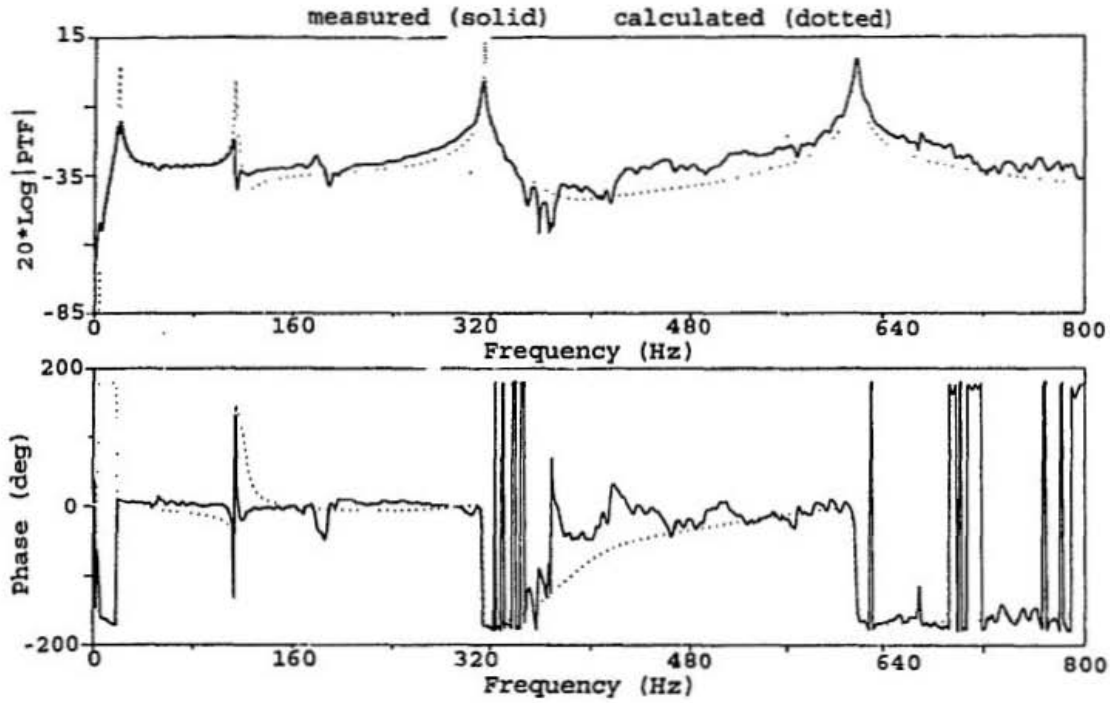

Figure 6.1: Comparison of calculated and measured PTF's for the regions between the natural frequencies at 80 % span of the beam (x=512 mm) with an altitude of 35 mm. Underestimation by the measured response at the natural frequencies was due to the coarse frequency resolution required to span the 0 to 800 Hz region.

Overall, the calculated and measured PTF's magnitudes and phases were quite similar. In places, the calculated PTF tended to underestimate the measured PTF magnitude by up to 6 dB (factor of 2) (e.g. between 400 and 560 Hz). The roughness of the measured PTF was attributed to a combination of signal noise in regions of small acoustic response and interference from the scattered field.

Fig. 6.2 makes the same comparison as Fig. 6.1 but with an altitude of 85 mm. Again, the calculated and measured magnitudes and phases were in reasonably good agreement. The calculated PTF still tended to underestimate the measured PTF magnitude, by up to 6 dB in places. It was observed that at each of the four positions the agreement was quite similar at both altitudes. Hence we will continue with just the comparisons at 35 mm.

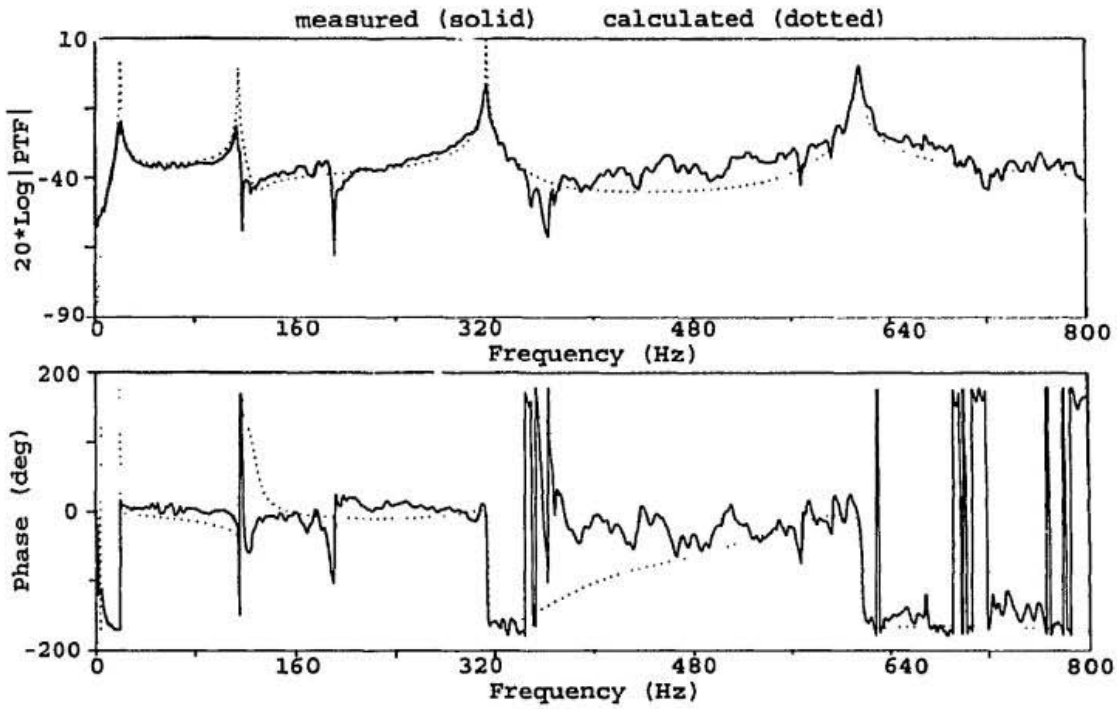

Figure 6.2: Comparison of calculated and measured PTF's for the regions between the natural frequencies at 80 % span of the beam (x=512 mm) with an altitude of 85 mm.

Fig. 6.3 compares calculated and measured PTF's at 60 % beam span (x=384 mm). The agreement was similar to the two previous examples. Again the calculated PTF had a tendency to underestimate the measured PTF magnitude. Fig.'s 6.4 and 6.5 continue the comparisons at 40% (x=256 mm) and 20 % (x=128 mm) of beam span respectively. The underestimation of the measured PTF magnitudes by the calculated PTF's was apparent in both cases. In these last two cases the underestimation appeared to increase somewhat with frequency. These results suggested that the underestimation was linked to the effects of baffling. The calculated pressure, based on a free space calculation, was generally within -6 db of the observed pressure, (i.e. the factor of 2 increase in magnitude that would be introduced by a baffle in the plane of the source). The baffling effects would have increased with decreasing wavelength (i.e. increasing frequency).

Fine resolution PTF's were also collected at altitudes of 35 and 85 mm above the beam. Six spectra were collected for each of the second, third and fourth modes. Unfortunately, a fine resolution spectrum for the first mode was not obtained. With the excitation point at the free end, the limit of the exciter's mechanical travel was reached before the acoustic signal strength was adequate for a reliable PTF measurement.

For the second mode, PTF's were measured at a height of 35 mm for x=256 and 576 mm and at heights of 35 and 85 mm for x=128 and 384 mm. In all 6 cases the calculated pressure overestimated the peak response by approximately 3 1/2 dB (~33 %). Fig. 6.6 compares the measured and calculated PTF's for the second mode at 60 % beam span (x=384 mm) and 35 mm altitude.

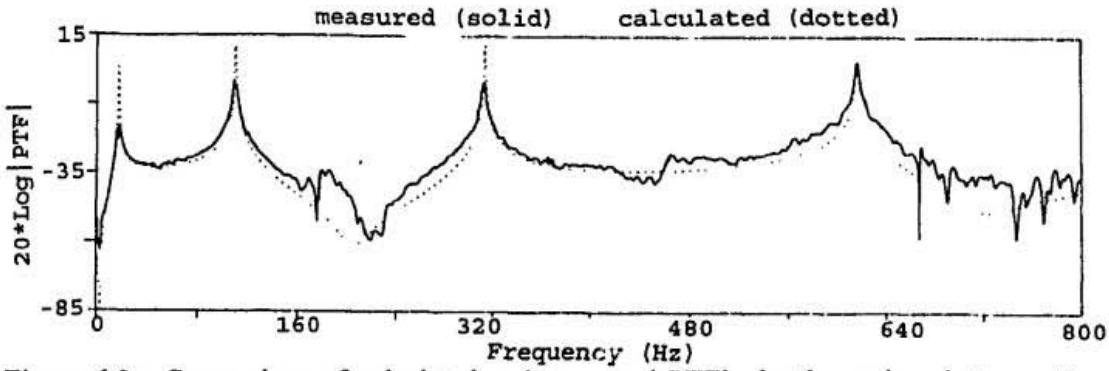

Figure 6.3: Comparison of calculated and measured PTF's for the regions between the natural frequencies at 60 % span of the beam (x=384 mm) with an altitude of 35 mm.

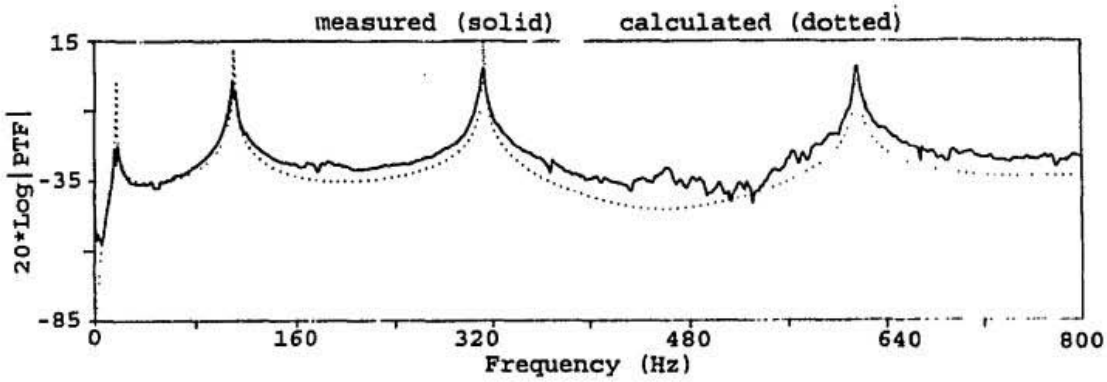

Figure 6.4: Comparison of calculated and measured PTF's for the regions between the natural frequencies at 40 % span of the beam (x=256 mm) with an altitude of 35 mm.

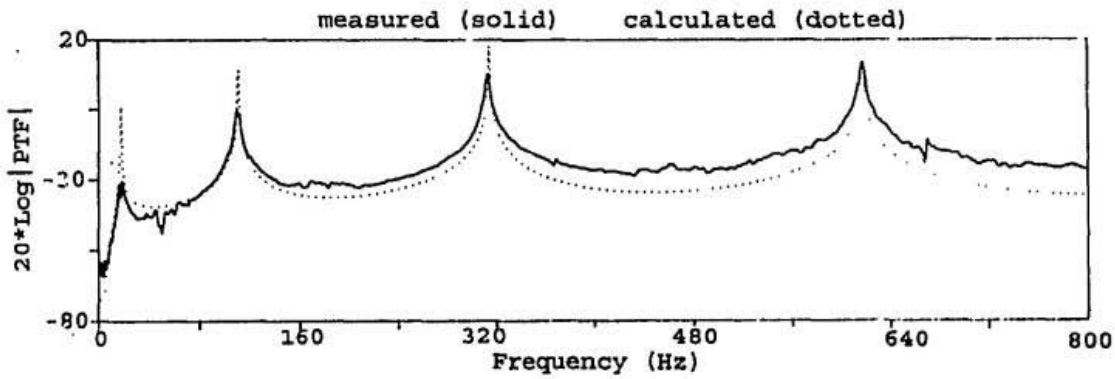

Figure 6.5: Comparison of calculated and measured PTF's for the regions between the natural frequencies at 20 % span of the beam (x=128 mm) with an altitude of 35 mm.

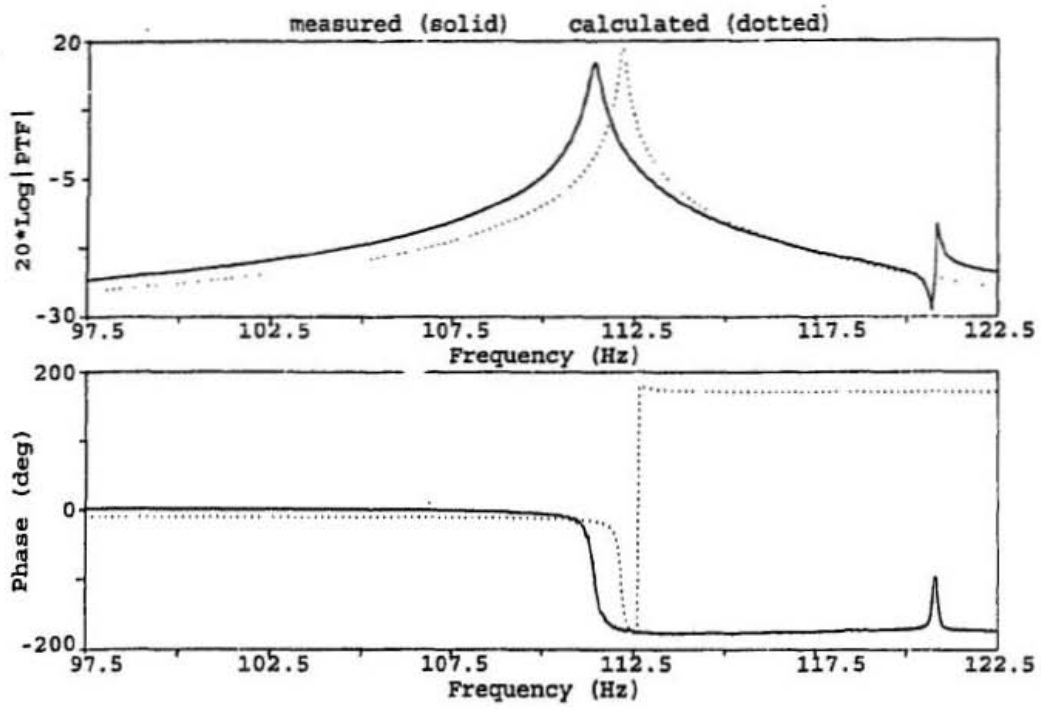

Figure 6.6: Comparison of calculated and measured PTF's for the second mode at 60 % beam span (x=384 mm) at a height of 35 mm.

For the third and fourth modes, PTF's were measured at a height of 35 mm for x=256 and 512 mm and at heights of 35 and 85 mm for x=128 and 384 mm. For the third mode four of the calculated PTF's underestimated peak response (-3 1/2 dB at x=128, 256 and 384 mm (lower altitude only)). Fig. 6.7 illustrates the typical difference between measured and calculated PTF's for the third mode at 20 % beam span (x=128 mm) and 85 mm altitude.

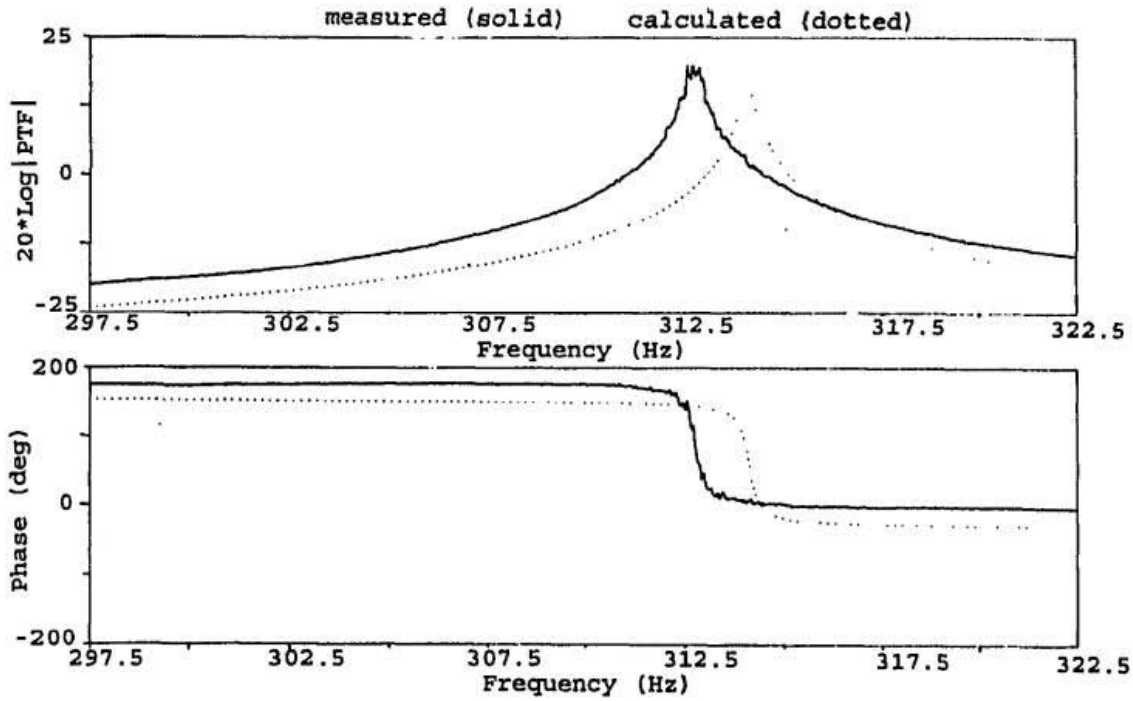

Figure 6.7: Comparison of calculated and measured PTF's for the third mode at 20 % beam span (x=128 mm) at a height of 85 mm.

There were only two cases where the calculated PTF overestimated the measured PTF. In one case, at x= 512 mm, (Fig. 6.8) the calculated PTF overestimated peak response by 1 1/2 dB (15 %). In the other case, at x=384 mm at a height of 85 mm, the least response for all 3rd mode PTF's was observed. There the calculated PTF overestimated peak response by about 5 dB (45 %). This may have been a minimum in the field.

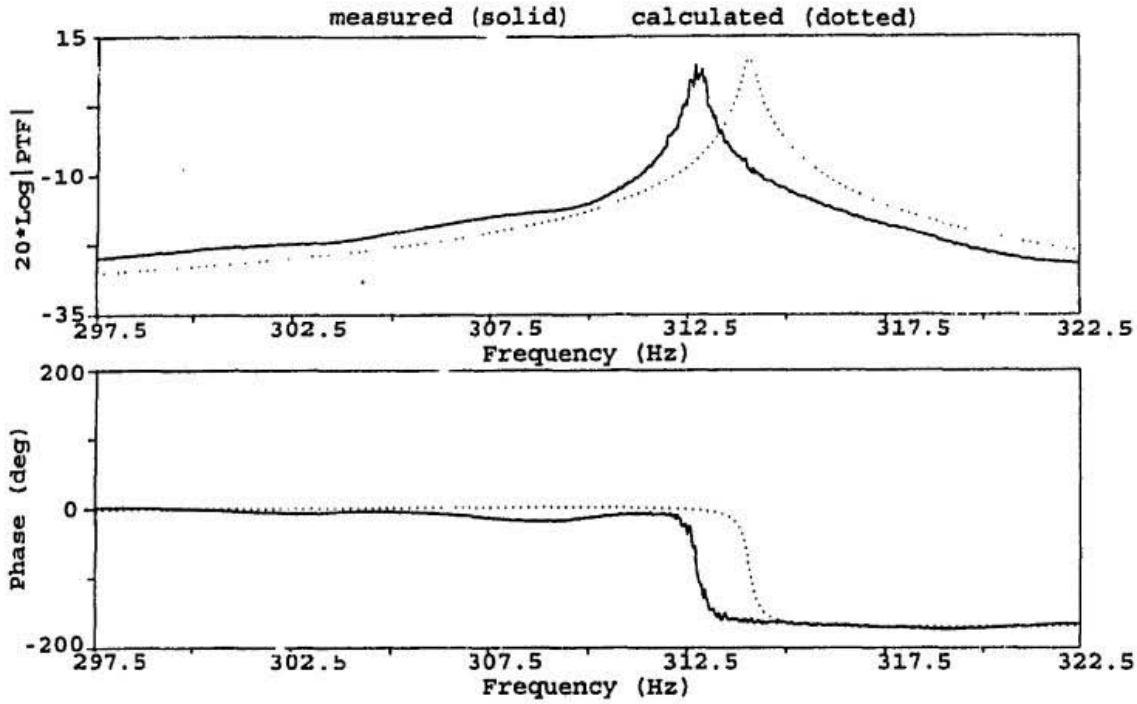

Figure 6.8: Comparison of calculated and measured PTF's for the third mode at 80 % beam span (x=512 mm) at a height of 85 mm.

The PTF's calculated for the fourth mode typically underestimated peak response by 7 dB (55 %). This is illustrated in Fig.'s 6.9 and 6.10 which compare measured and calculated PTF's at x=128 and 384 mm respectively for an altitude of 85 mm. In an isolated case, at the free end of the beam (x=512mm), peak response was underestimated by just 3 1/2 dB.

From these results, it was concluded that the model could be used with some caution to indicate the general trend with position of amplitude and phase.

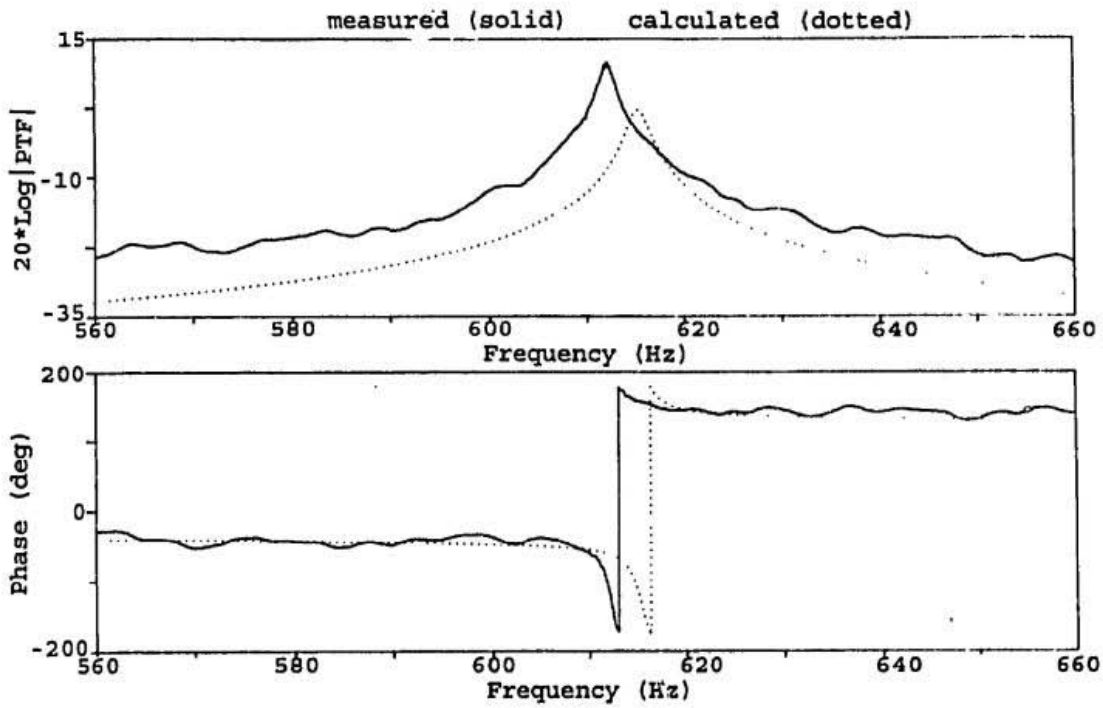

Figure 6.9: Comparison of calculated and measured PTF's for the fourth mode at 20 % beam span (x=128 mm) at a height of 85 mm.

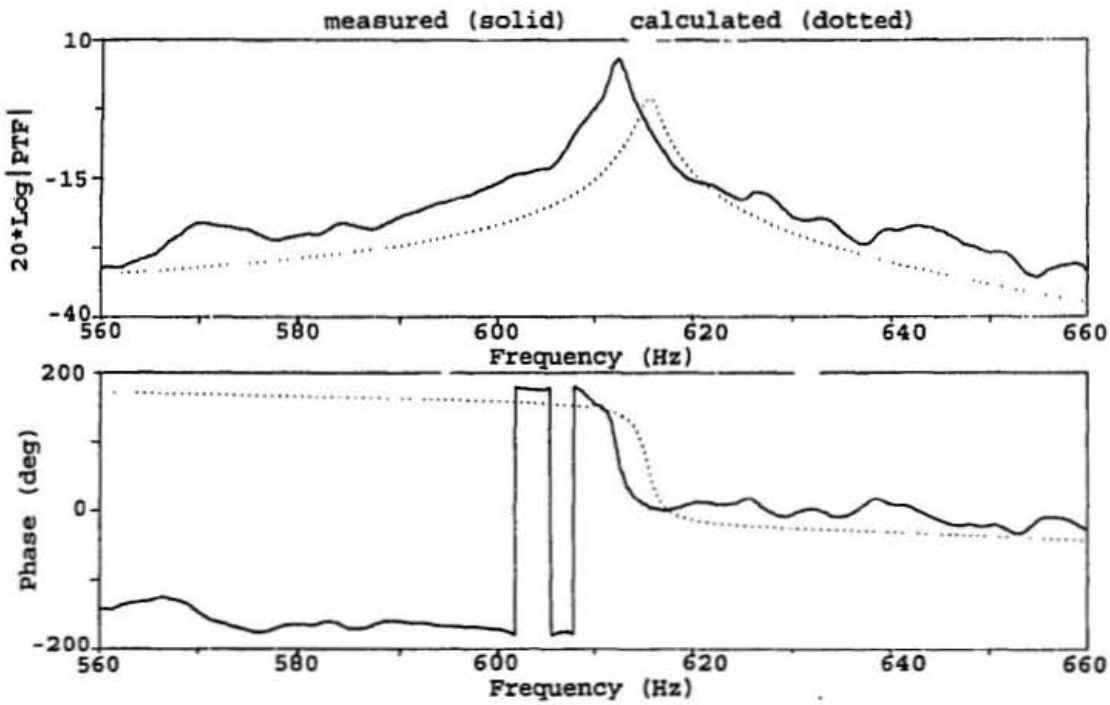

Figure 6.10: Comparison of calculated and measured PTF's for the fourth mode at 60 % beam span (x=384 mm) at a height of 85 mm.

6.4 Calculated and Measured Phase Difference

A measurement of time averaged acoustic intensity (see chapter 2) is very much a measurement of the phase difference between two pressures. With this in mind a comparison of the spatial variation of phase was made between the modelled field above the beam, the field measured above the beam and a field consisting of plane waves.

A microphone spacing of 50 mm was used, corresponding to altitudes of 35 and 85 mm above the centreline of the beam. This orientation would be used for measuring the z component of acoustic intensity. The comparison concentrated in the natural frequency regions where the PTF phase underwent a change of 180°. Two comparisons were made for the second mode at 40 (x=256 mm) and 60 % (x=384 mm) of beam span. Fig. 6.11 plots the measured and observed phases in the region of the second mode for 60 % of beam span. The modelled PTFs showed a uniform phase difference of -4.3°. The observed phase difference was only -1.3° on average and was not uniform. Similar results were observed at 40% span.

Four phase difference comparisons were made for the third mode at spans of 20, 40, 60 and 80 % beam span. At 20 % span (Fig. 6.12) the modelled PTF showed a constant phase difference of -9.3° while the observed PTF had a negligible average phase difference of -0.2°. As the observation point moved towards the free end, however, the observed phase difference increased relative to the modelled phase difference. At 80 % span (Fig. 6.13) the situation had reversed. Modelled pressure showed a constant phase difference of only 3° while the measured pressure had an average phase difference of 5.7°.

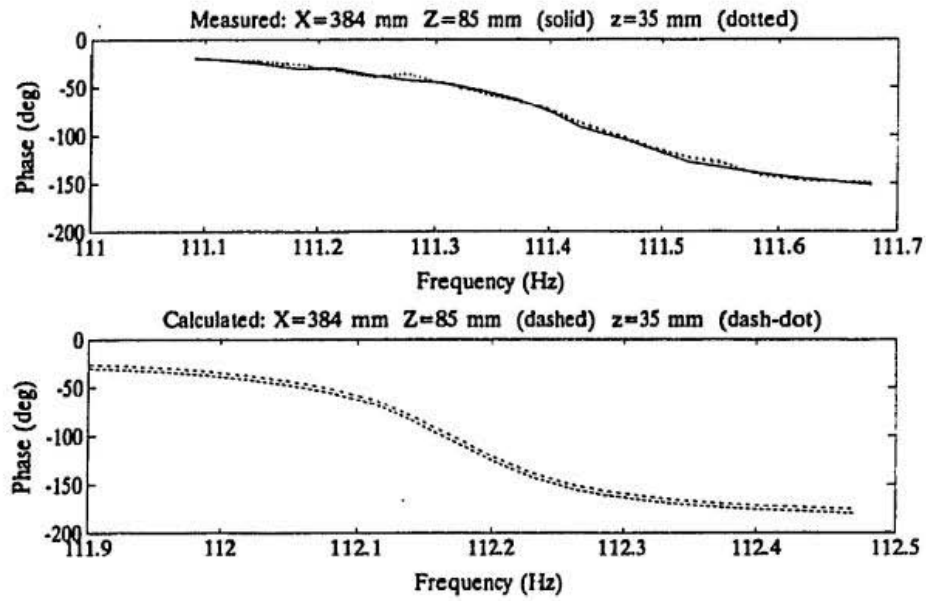

Figure 6.11: Comparison of calculated and measured phase difference between z=85 and z=35 mm at 60 % beam span (x=384 mm) in the region of the second mode.

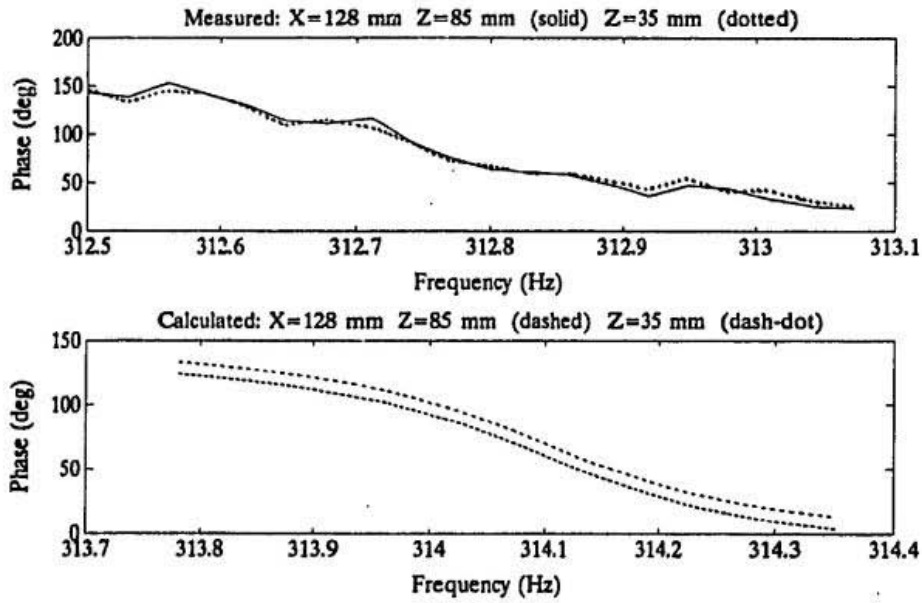

Figure 6.12: Comparison of calculated and measured phase difference between z=85 and z=35 mm at 20 % beam span (x=128 mm) in the region of the third mode.

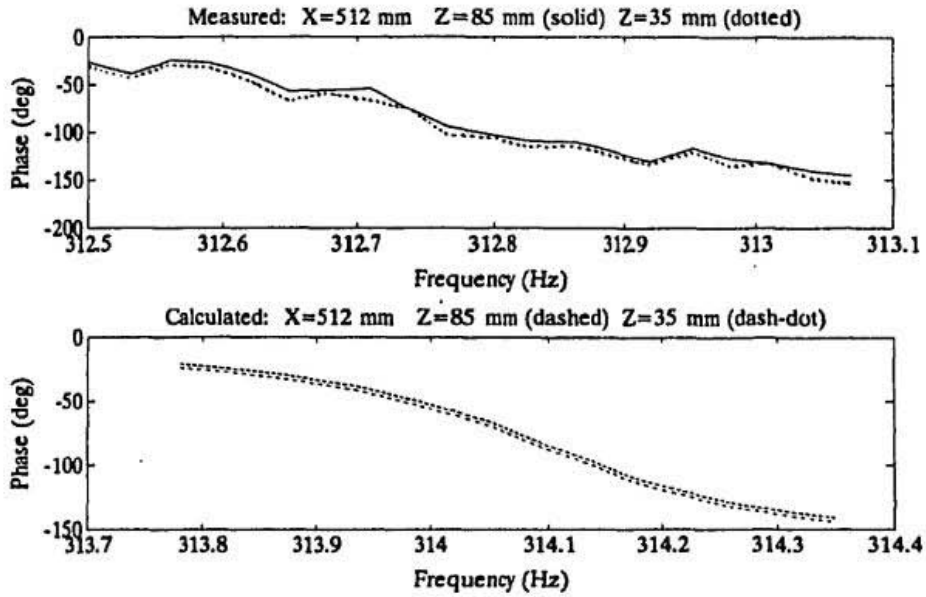

Figure 6.13: Comparison of calculated and measured phase difference between z=85 and z=35 mm at 80 % beam span (x=512 mm) in the region of the third mode.

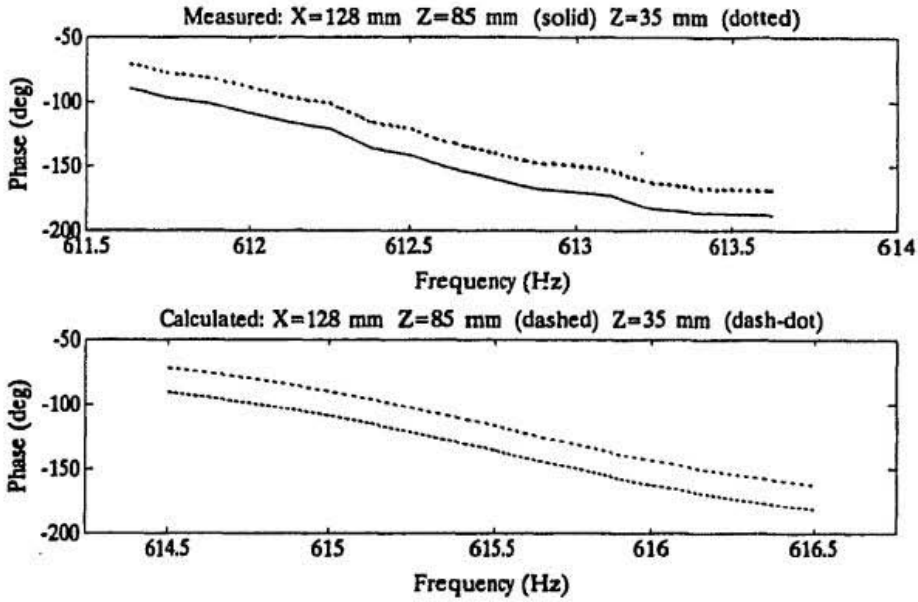

Figure 6.14: Comparison of calculated and measured phase difference between z=85 and z=35 mm at 20 % beam span (x=128 mm) in the region of the fourth mode.

Two phase difference comparisons were made for the fourth mode at 20 and 60% of beam span. At 20 % span (Fig. 6.14) modelled and measured phase differences were both uniform and almost equal, -18.9 and -19.6° respectively. The modelled and measured phase differences at 60 % span were also uniform. However the modelled phase difference was -9.3° while the measured difference was only -2.1°.

The phase difference assuming plane waves and the average values of the calculated and measured phase differences are summarized in table 6.1. For plane waves, a 50 mm spacing corresponded to phase differences of 5.9, 16.4 and 32.2° for modes 2, 3 and 4 respectively.

Table 6.1 Comparison of phase difference between z=85 and z=35 mm

Mode No	Freq (Hz)	Position X (mm)	Average Phase Difference Plane Wave (Deg)	Modelled (Deg)	Measured (Deg)
2	112	256	-5.9	-3.2	-1.3
		384	-5.9	-4.3	-1.2
3	313	128	-16.4	-9.3	-0.2
		256	-16.4	-12.0	-3.3
		384	16.4	10.9	6.1
		512	16.4	3.0	5.7
4	613	128	-32.2	-18.9	-19.6
		384	-32.2	-9.3	-2.1

The results indicate that in the near field of a distributed source, expectations for a phase difference based on a plane wave calculation (using microphone spacing and

wavelength) would be overly optimistic. If the modelled phase difference accurately portrays free space conditions then no more than about half the plane wave phase difference might be observed in the near field. Even expectations for half the plane wave phase difference in the near field could be optimistic depending on the measurement position. Finally phase differences smaller than half the plane wave phase difference would be expected in a reverberant environment.

6.5 Summary

Signal noise in regions of small acoustic response, the scattered field, and the effects of baffling were assumed to be responsible for most of the differences between the modelled and measured phase distributions. However, it is also possible that the calculation of the free space phase distribution close to the beam needed the rigour of a boundary value series solution. An answer to this question required either the boundary value solution itself or measurements in an anechoic chamber, both beyond the scope of this work.

Nonetheless, for this case (beam in a semi-reverberant enclosure), phase differences were observed in the near field, that were typically one half to one quarter of that modelled for free space, and that were an even smaller fraction of the phase difference that would be expected from plane waves. The implication is that larger microphone spacings are required for near field acoustic intensity measurements than those spacings that would be anticipated from simple calculations using just microphone spacing and wavelength.

FINAL SUMMARY

The research for this thesis occurred within a program to develop acoustic methods for monitoring mechanical behaviour of structures for indications of fatigue, and focussed on the acoustic field close to a vibrating surface. This work examined acoustic intensity and its measurement in the near field. Both the time domain and frequency domain methods of measurement were reviewed. The cross spectral formulation was shown to be equivalent to a windowed process that relies on the discrete Fourier transforms of two pressures closely replicating their corresponding continuous Fourier spectra counterparts. The measurement clearly depends on the ability to resolve the phase difference between two pressures. The ability to resolve phase difference is perhaps the most demanding aspect of the measurement. An example was given to show that the statistical distribution of intensity can broaden in moving from the far field to the near field. Moving to the near field has the adverse effect of lengthening the measurement interval to retain measurement accuracy.

From the single measurement, the focus shifted to obtaining an estimate of the spatial distribution of acoustic intensity in the near field. A method for mapping the spatial distribution was described that combined the physics of a closed surface with approximations from a Taylor's series analysis. The method was successfully tested on the near field of a cantilever beam. Several examples were used to show that this method provided a quantitative assessment of whether the calculated spatial distribution of intensity was a reasonable representation of the acoustic field.

The focus then returned to the single measurement of intensity, for the case where an applied force caused a mechanical system to radiate sound. It was shown that a form of normalized acoustic intensity could be constructed from transfer functions of pressure and force. Acoustic intensity constructed from pressure transfer functions was successfully tested in the near field of a cantilever beam. The testing process again emphasized the need for the discrete Fourier spectra to closely replicate their continuous Fourier spectra counterparts, with particular attention to obtaining good estimates of the phase difference between pressure and force. It was noted that the normalized acoustic intensity emphasized the natural frequency regions where the ratio of radiated power to applied force was large.

After using a cantilever on two occasions as a sound source, attention was directed to modelling the acoustic field of the beam. First, the damped vibration response of the beam was modelled using Euler-Bernoulli beam theory. Modal analysis was applied to the the beam's measured response to obtain the beam's complex eigenfrequencies. The main area of interest was the natural frequency regions. There, the modelled response replicated observed response quite well, both in frequency and amplitude. The agreement was due in part to an accurate estimate of Young's modulus from the data. Overall the agreement was good everywhere except in regions of local minima. The frequencies of calculated and observed local minima were sometimes separated (attributed to either limitations of theory or a truncated series solution).

The vibration model of the beam was then used in an integral expression that

treated the beam as a planar source. This formulation for the acoustic field was an approximation that ignored the sound radiated by the far side of the beam. Its use was restricted to interior points close to the beam's surface. While the modelled field agreed in general terms with the observed field there were noticeable differences. The model had a tendency to underestimate the observed acoustic field by up to 6 dB (attributed to the baffling effect of the beam and its support). The observed field also exhibited a certain amount of spectral roughness (attributed to a combination of small signal response and the presence of a scattered field).

With the assumption that the model would indicate the general trend with position of the acoustic field, the model was used to examine the spatial distribution of phase in the near field of the beam. It was found that over a typical microphone spacing of 50 mm, that the observed phase differences in the natural frequency regions were typically one half to a quarter of that predicted by the model (free space). The model in turn predicted typically half the phase difference that would be expected from plane waves. This suggested that larger microphone spacings are required for near field acoustic intensity measurements than those spacings that would be obtained from simple calculations using just microphone spacing and wavelength.

REFERENCES

Bissenger, G. and Chowdhury, M.R. "Comparison of Modal Analysis Measurements With Microphone and Accelerometer on Hammer-Impacted Structures", Proceedings of the 8th International Modal Analysis Conference, Vol. 1, 667-672, (1990).

Chung, J.Y. "Cross-Spectral Method of Measuring Acoustic Intensity Without Error Caused By Instrument Phase Mismatch," Journal of the Acoustical Society of America, 64(6), 1613-1616, (1978)

Chung, J.Y. "Fundamental Aspects of the Cross-Spectral Method of Measuring Acoustic Intensity", International Congress On Recent Developments In Acoustic Intensity, Senlis Oct 2, (1981).

Chung, J.Y. and Pope, J. "Practical Measurement Of Acoustic Intensity -- The Two-Microphone Cross-Spectral Method" Proceedings Inter Noise 78, San Francisco, 893-900, May 8, (1978).

Dyrlund,O. "A Note On Statistical Errors In Acoustic Intensity Measurements", Letters To The Editor, Journal of Sound and Vibration, 90(4), 585-589, (1983).

Ewins, D.J. "Modal Testing: Theory and Practice", Research Studies Press Ltd., Letchworth, Hertfordshire, England, (1986).

Fahy, F. "Measurement Of Acoustic Intensity Using The Cross-Spectral Density Of Two Microphone Signals", Journal of the Acoustical Society of America, 62(4), (1977).

Fahy, F. "Sound Intensity", Elsevier Science Publishers Ltd.
New York, New York (1989).

Guigne, J.Y., Klein, K., Swamidas, A.S.J. and Guzzwell, J. "Modal Information From Acoustic Measurements For Fatigue Crack Detection Applications", Proceedings of the 11th International Conference on Offshore Mechanics and Arctic Engineering, Calgary, Alberta, (1992).

Jacobsen, F. and Nielsen, T.G. "Spatial Correlation and Coherence in a Reverberant Sound Field", Journal of Sound and Vibration, 118(1), 175-180, (1987).

Junger, M.C., and Feit, D. "Sound, Structures, and Their Interaction", The MIT Press, Cambridge, Massachusetts, 2nd ed., p. 201ff, (1986).

Kaye, G.W.C. and Laby, T.H. "Tables of Physical and Chemical Constants", Longman 14th ed., New York, (1973).

Klein, K., Guigné, J.Y. and Swamidas, A.S.J. "Contact and Acoustic Measurements on a Fatiguing Cantilever Beam", Proceedings of the 13th International Modal Analysis Conference, Nashville, Tennessee, (1995).

Klein, K. and Guigné, J.Y. "Near Field Acoustic Intensity Mapping Using A Closed Surface". Journal of the Acoustical Society of America, 98(2), 973-980 (1995).

Krishnappa, G. "Cross-Spectral Method of Measuring Acoustic Intensity by Correcting Phase and Gain Mismatch Errors by Microphone Calibration", Journal of the Acoustical Society of America, 69(1), (1981).

Mann III, J.A., Tichy, J. and Romano, J. "Instantaneous and Time Averaged Energy Transfer in Acoustic Fields", Journal of tbe Acoustical Society of America, 82(1), (1987).

Mendenhall, W. "Introduction to Probability and Statistics", Duxbury Press, Wadsworth Publishing Co., Belmont, California, 3rd Ed., (1971).

Morse, P.M. and Ingard, K.U. "Theoretical Acoustics", Princeton University Press, Princeton, New Jersey, (1968).

Myklestad, N.O. "The Concept of Complex Damping", Journal of Applied Mechanics, 19, 284-286, (1952).

Norton, M.P. "Fundamentals of Noise and Vibration Analysis for Engineers", Cambridge University Press, New York, New York, p.31, (1994).

Okubo, N. and Masuda, K. "Acoustic Sensitivity Analysis Based on the Results of Acoustic Modal Testing", Proceedings of the VIIIth International Modal Analysis Conference, Vol. I, 270-274, (1990).

Pascal, J.C. and Carles, C. "Systematic Measurement Errors With Two Microphone Sound Intensity Meters", Journal of Sound and Vibration, 83 (1), 53-65, (1982).

Pierce, A.D. "Acoustics", Acoustical Society of America, Woodbury, New York, (1991).

Press, W.H., Flannery, B.P., Teukolsky, S.A., and Vetterling, W.T. "Numerical Recipes; The Art of Scientific Programming (Fortran Version)", Cambridge University Press, Cambridge, (1990).

"Physical Acoustics: Principles and Methods", Ed. Warren P. Mason, New York Academic Press, New York, New York, 1(A), Chap.4, p.272ff, (1964).

Pascal,J.C. "Analytical Expressions For Random Errors of Acoustic Intensity", Proceedings of the International Conference on Noise Control Engineering, Poughkeepsie, New York, (1986).

Pavic, G. "Measurement of Sound Intensity", Journal of Sound and Vibration, 51(4), 533-545, (1977).

Pepin, H. "Statistical Errors in Sound Power Determination by Intensity Measurements", Proceedings of the International Conference on Noise Control Engineering, Poughkeepsie, New York, (1984).

Petterson, O.K. "A Procedure For Determining The Sound Intensity Distribution Close To a Vibrating Surface", Journal of Sound and Vibration, 66(4), 626-629, (1979).

Ross, D. "Mechanics of Underwater Noise",Pergamon Press, New York, 375 pp, (1976).

Schultz, T.J., Smith, P.W. and Malme, I.C. "Measurement of Acoustic Intensity in Reactive Sound Field", Journal of the Acoustical Society of America, 57(6) Part 1, (1975).

"Science Data Book", Ed. R.M. Tennant, Oliver & Boyd, Edinburgh, p. 60, (1971).

Seybert, A.F. "Statistical Errors In Acoustic Intensity Measurements", Journal of Sound and Vibration, 75(4), 519-526, (1981).

Spinner, S., and Tefft, W.E. "A Method For Determining Mechanical Resonance Frequencies and For Calculating Elastic Moduli From These Frequencies", Proc. American Society for Testing and Materials, 61, 1221-1238, (1961).

Tichy, J. "Some Effects of Microphone Environment on Intensity Measurements", International Congress On Recent Developments In Acoustic Intensity, Senlis, Oct 2, (1981).

Timoshenko, S.P. "On the Correction for Shear of the Differential Equation for Transverse Vibrations of Prismatic Bars", London, Edinburgh and Dublin Philosophical Magazine and Journal of Science, 6(41), 744-746, (1921).

Thompson, J.K. and Tree, D.R. "Finite Difference Approximation Errors In Acoustic

Intensity Measurements", Journal of Sound and Vibration, 75(2), 229-238, (1981).

Watkinson, P.S. "The Practical Assessment of Errors in Sound Intensity Measurement", Journal of Sound and Vibration, 105(2), (1986).

Williams, E.G. and Maynard, J.D. "Intensity Vector Field Mapping With Nearfield Holography", International Congress On Recent Developments In Acoustic Intensity, Senlis, Oct 2, (1981).

Wolfenden, A., Harmouche, M.R., Blessing, G.V., Chen, Y.T., Terranova, P., Dayal, V., Kinra, V.K., Lemmens, J.W., Phillips, R.R., Smith, J.S., Mahmoodi, P., and Wann, R.J. "Dynamic Young's Modulus Measurements in Metallic Materials: Results of an Interlaboratory Testing Program", Journal of Testing and Evaluation, 17(1), 2-13, (1989).

Appendix A
Statistics of Intensity For Waves at Two Frequencies

Averaging over an infinite time frame would remove all interaction between adjacent frequency components, but real measurement time frames are finite. Consequently, interaction can occur between adjacent frequency components that affects the reproducibility of the measurement of time averaged acoustic intensity.

Consider a pressure with two frequency components,

$$p(x;t) = f_1(x)\cos(k_1 x-\omega t) + f_2(x)\cos(k_2 x-(\omega+\Delta\omega)t) \qquad (A.1)$$

where $f_{1,2}(\vec{x})$ are real functions of position coordinate x. Using Euler's relation the particle velocity is,

$$\begin{aligned}\vec{u}(x;t) = \frac{1}{\rho_o}\Big[&\frac{\vec{\nabla}f_1(x)}{\omega}\sin(k_1 x-\omega t) + \frac{k_1 f_1(x)}{\omega}\cos(k_1 x-\omega t)\\ &+ \frac{\vec{\nabla}f_2(x)}{(\omega+\Delta\omega)}\sin(k_2 x-(\omega+\Delta\omega)t)\\ &+ \frac{k_2 f_2(x)}{(\omega+\Delta\omega)}\cos(k_2 x-(\omega+\Delta\omega)t)\Big]\end{aligned} \qquad (A.2)$$

Then $\Psi(t)$ is given by,

$$\begin{aligned}\bar{\Psi}(t) = \frac{1}{\rho_o \omega}\,[\, & f_1 \nabla f_1 \sin(k_1 x-\omega t)\cos(k_1 x-\omega t) + k_1 f_1^2 \cos^2(k_1 x-\omega t) \\ & + f_2 \nabla f_1 \sin(k_1 x-\omega t)\cos(k_2 x-(\omega+\Delta\omega)\,t) \\ & + k_1 f_1 f_2 \cos(k_1 x-\omega t)\cos(k_2 x-(\omega+\Delta\omega)\,t)\,] \\ + \frac{1}{\rho_o\,(\omega+\Delta\omega)}\,[\, & f_1 \nabla f_2 \cos(k_1 x-\omega t)\sin(k_2 x-(\omega+\Delta\omega)\,t) \\ & + k_2 f_1 f_2 \cos(k_1 x-\omega t)\cos(k_2 x-(\omega+\Delta\omega)\,t) \\ & + f_2 \nabla f_2 \sin(k_2 x-(\omega+\Delta\omega)\,t)\cos(k_2 x-(\omega+\Delta\omega)\,t) \\ & + k_2 f_2^2 \cos^2(k_2 x-(\omega+\Delta\omega)\,t)\,]\end{aligned} \tag{A.3}$$

which reduces to,

$$\begin{aligned}\bar{\Psi}(t) = \frac{1}{\rho_o}\,[\, & \frac{f_1 \nabla f_1}{2\omega}\sin 2(k_1 x-\omega t) + \frac{k_1 f_1^2}{\omega}\cos^2(k_1 x-\omega t) \\ & + \left[\frac{f_2 \nabla f_1}{2\omega} - \frac{f_1 \nabla f_2}{2(\omega+\Delta\omega)}\right]\sin((k_1-k_2)\,x+\Delta\omega\, t) \\ + \frac{f_1 f_2}{2}\left[\frac{k_1}{\omega}+\frac{k_2}{\omega+\Delta\omega}\right]\big(\cos((k_1-k_2)\,x+\Delta\omega\, t) & + \cos((k_1+k_2)\,x-(2\omega+\Delta\omega)\,t)\big) \\ & + \left[\frac{f_2 \nabla f_1}{2\omega} + \frac{f_1 \nabla f_2}{2(\omega+\Delta\omega)}\right]\sin((k_1+k_2)\,x-(2\omega+\Delta\omega)\,t) \\ + \frac{f_2 \nabla f_2}{2(\omega+\Delta\omega)}\sin 2(k_2 x-(\omega+\Delta\omega)\,t) & + \frac{k_2 f_2^2}{\omega+\Delta\omega}\cos^2(k_2-(\omega+\Delta\omega)\,t)\,]\end{aligned} \tag{A.4}$$

The time average of $\Psi(t)$ is now taken over the interval $[t_o, t_o+T]$.

$$\overline{\Psi(t)} = \frac{1}{T}\int_{t_o}^{t_o+T} \Psi(t)\, dt \tag{A.5}$$

Performing the integration and substituting for $k_1=\omega/c$, $k_2=(\omega+\Delta\omega)/c$ yields,

$$\overline{\nabla(t)} = \frac{1}{\rho_o}\left[\frac{f_1 \nabla f_1}{2\omega^2 T}\sin(\omega T)\sin 2(\phi_1 - \omega(t+\frac{T}{2}))\right.$$
$$+ \frac{f_2 \nabla f_2}{2(\omega+\Delta\omega)^2 T}\sin((\omega+\Delta\omega)T)\sin 2(\phi_2 - (\omega+\Delta\omega)(t+\frac{T}{2}))$$
$$+ \frac{f_1^2}{2c} + \frac{f_2^2}{2c}$$
$$+ \left[\frac{f_2 \nabla f_1}{\omega\Delta\omega T} - \frac{f_1 \nabla f_2}{\Delta\omega(\omega+\Delta\omega)T}\right]\sin(\frac{\Delta\omega T}{2})\sin(\phi_1 - \phi_2 + \Delta\omega(t+\frac{T}{2}))$$
$$+ \frac{2 f_1 f_2}{\Delta\omega c T}\sin(\frac{\Delta\omega T}{2})\cos(\phi_1 - \phi_2 + \Delta\omega(t+\frac{T}{2})) +$$
$$+ \left[\frac{f_2 \nabla f_1}{\omega(2\omega+\Delta\omega)T} + \frac{f_1 \nabla f_2}{(\omega+\Delta\omega)(2\omega+\Delta\omega)T}\right]\sin((\omega+\frac{\Delta\omega}{2})T)\sin(\phi_1 + \phi_2 - (2\omega+\Delta\omega)(t+\frac{T}{2}))$$
$$+ \frac{2 f_1 f_2}{(2\omega+\Delta\omega)cT}\sin((\omega+\frac{\Delta\omega}{2})T)\cos(\phi_1 + \phi_2 - (2\omega+\Delta\omega)(t+\frac{T}{2}))$$
$$+ \frac{f_1^2}{2\omega T c}\sin(\omega T)\cos 2(\phi_1 - \omega(t+\frac{T}{2}))$$
$$+ \left.\frac{f_2^2}{2(\omega+\Delta\omega)Tc}\sin((\omega+\Delta\omega)T)\cos 2(\phi_2 - (\omega+\Delta\omega)(t+\frac{T}{2}))\right] \qquad (A.6)$$

where,

$$\phi_1 = k_1 x$$
$$\phi_2 = k_2 x \qquad (A.7)$$

Six of the ten terms contain either a $(\omega T)^{-1}$ or $(\omega^2 T)^{-1}$ dependence. The contribution of these terms will decrease as T increases. It will be assumed that T is sufficiently large to ignore these terms. The remaining terms are,

$$\frac{f_1^2}{2\rho_o c} + \frac{f_2^2}{2\rho_o c}$$
$$+ \frac{1}{\rho_o}\left[\frac{f_2 \nabla f_1}{\omega\Delta\omega T} - \frac{f_1 \nabla f_2}{\Delta\omega(\omega+\Delta\omega)T}\right]\sin(\frac{\Delta\omega T}{2})\sin(\phi_1 - \phi_2 + \Delta\omega(t+\frac{T}{2})) \qquad (A.8)$$
$$+ \frac{2 f_1 f_2}{\rho_o c\Delta\omega T}\sin(\frac{\Delta\omega T}{2})\cos(\phi_1 - \phi_2 + \Delta\omega(t+\frac{T}{2}))$$

The first two terms are just the time averaged acoustic intensity associated with

frequencies ω and $\omega+\Delta\omega$ respectively as $T\to\infty$. The third and fourth terms are of interest for the case when $\Delta\omega T<<1$. In that case $\sin(\Delta\omega T)\to\Delta\omega T$ leaving,

$$\frac{f_1^2}{2\rho_o c} + \frac{f_2^2}{2\rho_o c} + \frac{1}{2\rho_o}\left[\frac{f_2 \nabla f_1}{\omega} - \frac{f_1 \nabla f_2}{(\omega+\Delta\omega)}\right] \sin\left(\phi_1-\phi_2+\Delta\omega\left(t+\frac{T}{2}\right)\right) + \frac{f_1 f_2}{\rho_o c} \cos\left(\phi_1-\phi_2+\Delta\omega\left(t+\frac{T}{2}\right)\right) \tag{A.9}$$

The last two terms are sinusoidal components with frequency $\Delta\omega$. Each time the measurement is repeated with interval T, there will be a different contribution from these terms. This would be an impediment to obtaining reproducible measurements of average intensity. Larger values of $\Delta\omega T$ would then be required to mitigate this effect.

Appendix B

The two data sets plotted in Fig. 3.4 are compared by common component in Tables B.1, B.2 and B.3. The value estimated by CSIM is compared with the value measured at cell centre.

Table B.1 Comparison of data sets: X component at cell centre

Coord (mm) X	Y	Calculated by CSIM $\mu W/m^2$	Measured at Cell Centre $\mu W/m^2$
108	51	-23.1 ± 0.7	-21.0 ± 0.8
108	102	-31.9 ± 1.2	-36.3 ± 1.0
108	153	-22.0 ± 0.8	-18.1 ± 1.0
162	51	-10.5 ± 0.4	-11.0 ± 0.2
162	102	-12.1 ± 1.2	-14.4 ± 1.1
162	153	- 9.4 ± 0.7	-12.0 ± 0.3
216	51	1.6 ± 0.5	- 1.1 ± 0.4
216	102	4.1 ± 1.2	- 1.0 ± 0.2
216	153	3.4 ± 0.7	- 1.9 ± 0.5
270	51	10.5 ± 2.6	8.7 ± 2.5
270	102	15.0 ± 1.6	11.1 ± 0.4
270	153	11.3 ± 0.8	9.2 ± 0.8
324	51	13.6 ± 3.0	14.1 ± 0.4
324	102	19.0 ± 1.6	18.1 ± 0.6
324	153	12.2 ± 0.9	12.0 ± 0.6
378	51	10.8 ± 1.0	9.6 ± 0.2
378	102	14.2 ± 1.6	11.2 ± 0.2
378	153	7.6 ± 1.0	5.1 ± 0.2
432	51	0.6 ± 0.4	- 1.2 ± 0.3
432	102	1.4 ± 0.6	0.9 ± 0.1
432	153	- 2.1 ± 0.6	- 2.2 ± 0.1
486	51	-14.2 ± 0.5	-13.0 ± 0.2
486	102	-15.7 ± 0.3	-15.6 ± 0.2
486	153	-13.3 ± 0.4	-11.7 ± 0.3
541	51	-21.6 ± 0.6	-19.7 ± 0.3
541	102	-25.8 ± 0.8	-24.5 ± 0.4
541	153	-20.8 ± 2.3	-19.5 ± 0.7

Table B.2 Comparison of data sets: Y Component at cell centre

Coord (mm) X	Y	Calculated by CSIM $\mu W/m^2$	Measured at Cell Centre $\mu W/m^2$
108	51	6.1 ± 0.7	11.0 ± 0.2
108	102	- 1.1 ± 0.6	- 0.7 ± 0.3
108	153	- 9.6 ± 0.8	-14.1 ± 1.1
162	51	16.3 ± 0.6	18.1 ± 0.4
162	102	- 2.5 ± 0.3	3.1 ± 0.5
162	153	-16.2 ± 0.8	-14.6 ± 0.6
216	51	12.2 ± 0.8	14.1 ± 0.5
216	102	- 0.7 ± 1.0	- 0.2 ± 0.4
216	153	-16.6 ± 3.2	-18.3 ± 0.3
270	51	6.7 ± 0.4	9.0 ± 0.2
270	102	0.1 ± 0.4	0.4 ± 0.2
270	153	- 6.1 ± 0.6	- 7.8 ± 0.1
324	51	1.1 ± 0.1	1.3 ± 0.4
324	102	- 0.2 ± 0.1	- 0.2 ± 0.4
324	153	- 2.0 ± 0.3	- 2.6 ± 0.1
378	51	0.6 ± 0.3	0.0 ± 0.4
378	102	0.9 ± 0.2	0.0 ± 0.2
378	153	0.9 ± 0.2	1.3 ± 0.2
432	51	4.2 ± 0.7	1.3 ± 0.6
432	102	2.0 ± 0.6	0.8 ± 0.2
432	153	1.3 ± 0.6	- 1.1 ± 0.1
486	51	5.4 ± 0.5	6.9 ± 0.1
486	102	1.2 ± 0.3	- 0.8 ± 0.4
486	153	- 2.8 ± 0.3	- 3.9 ± 0.6
541	51	3.8 ± 0.4	3.9 ± 0.1
541	102	0.1 ± 0.2	- 2.3 ± 0.2
541	153	- 3.7 ± 0.8	- 4.6 ± 0.4

Table B.3 Comparison of data sets: Z component at cell centre

Coord (mm) X	Y	Calculated by CSIM $\mu W/m^2$	Measured at Cell Centre $\mu W/m^2$
108	51	61.8 ± 2.5	63.6 ± 1.2
108	102	73.3 ± 1.5	71.8 ± 0.8
108	153	64.6 ± 1.9	64.9 ± 1.1
162	51	47.9 ± 1.7	53.9 ± 0.8
162	102	66.9 ± 2.7	70.8 ± 0.8
162	153	46.1 ± 1.1	54.2 ± 0.8
216	51	38.5 ± 2.6	42.0 ± 0.7
216	102	47.7 ± 3.3	51.1 ± 0.5
216	153	37.4 ± 1.4	40.3 ± 1.0
270	51	23.1 ± 0.6	25.2 ± 0.3
270	102	29.4 ± 1.5	30.8 ± 0.3
270	153	25.1 ± 1.4	24.9 ± 0.2
324	51	4.3 ± 0.2	4.7 ± 0.1
324	102	4.4 ± 0.1	4.8 ± 0.1
324	153	5.1 ± 0.2	5.4 ± 0.1
378	51	-15.8 ± 1.8	-15.9 ± 0.2
378	102	-19.0 ± 1.6	-18.3 ± 0.6
378	153	-14.1 ± 1.2	-14.9 ± 0.2
432	51	-26.2 ± 1.1	-24.6 ± 0.6
432	102	-31.6 ± 1.2	-29.5 ± 0.7
432	153	-21.8 ± 2.2	-21.0 ± 0.1
486	51	-30.6 ± 1.7	-29.2 ± 1.0
486	102	-34.0 ± 1.4	-34.5 ± 0.8
486	153	-29.3 ± 3.0	-28.0 ± 0.7
541	51	-12.0 ± 1.3	-11.9 ± 0.7
541	102	-16.3 ± 1.1	-15.5 ± 0.7
541	153	-12.5 ± 2.3	-11.8 ± 0.4

The paired-difference test (see Mendenhall, [1971]) was applied to the data set for each intensity component (i.e. the set of differences $d_i = (\Psi_{measured})_i - (\Psi_{calculated\ by\ CSIM})_i$). The Student's t distribution was used to place 95 % confidence limits on the differences. The results are tabulated in Table B.4.

Table B.4 Paired Difference analysis by component in μWatts/m^2

Comp	Average	Variance	Confidence Interval (95 %)
x	-1.00	2.33	-1.00 ± 0.92
y	-0.05	2.22	-0.05 ± 0.88
z	1.52	2.09	1.52 ± 0.83

The variances of the distribution of differences were very similar for all three components. This suggests that apart from any non zero bias, the distribution of errors was independent of which component was measured. Bias's did exist for both x and z components but were relatively small compared to the range of intensity values observed for those components.